ISBN 978-82-326-2708-0 (printed ver.)
ISBN 978-82-326-2709-7 (electronic ver.)
ISSN 1503-8181

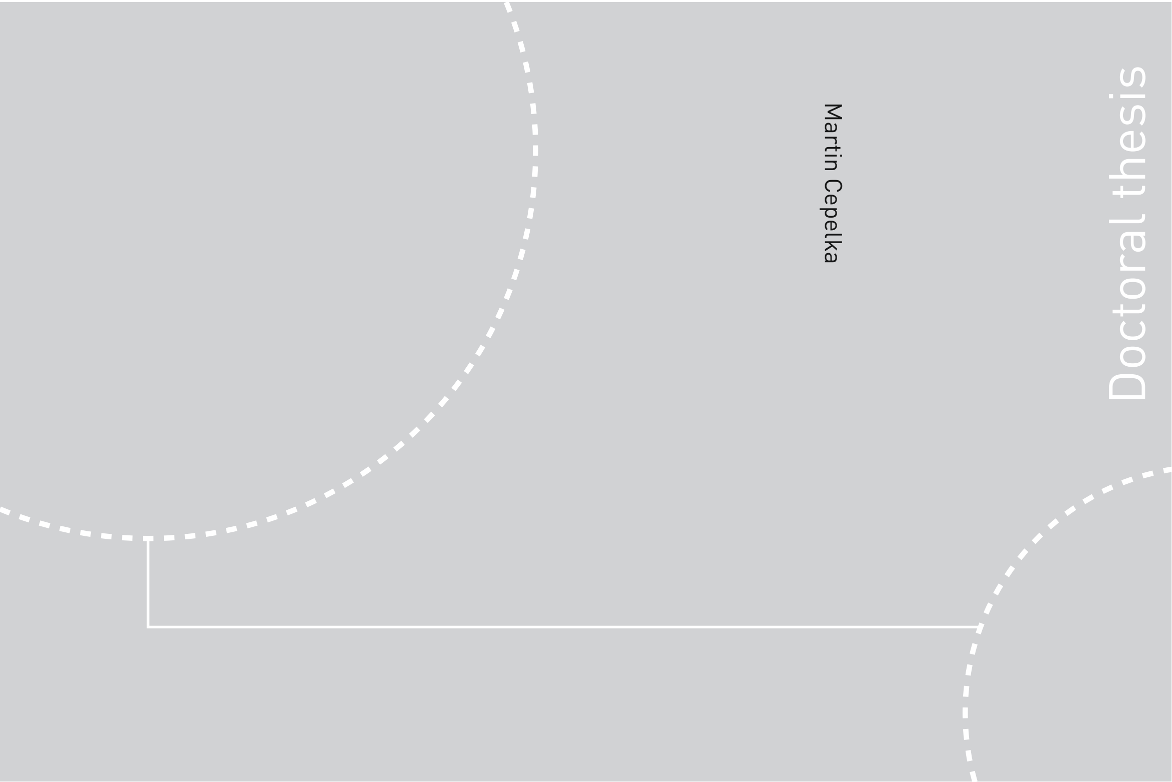

Doctoral thesis

Martin Cepelka

Doctoral theses at NTNU, 2017:320

NTNU
Norwegian University of Science and Technology
Thesis for the Degree of
Philosophiae Doctor
Faculty of Engineering
Department of Structural Engineering

NTNU
Norwegian University of
Science and Technology

NTNU

Doctoral theses at NTNU, 2017:320

Martin Cepelka

Splicing of Large Glued Laminated Timber Elements by Use of Long Threaded Rods

NTNU
Norwegian University of
Science and Technology

Martin Cepelka

Splicing of Large Glued Laminated Timber Elements by Use of Long Threaded Rods

Thesis for the Degree of Philosophiae Doctor

Trondheim, November 2017

Norwegian University of Science and Technology
Faculty of Engineering
Department of Structural Engineering

NTNU
Norwegian University of
Science and Technology

NTNU
Norwegian University of Science and Technology

Thesis for the Degree of Philosophiae Doctor

Faculty of Engineering
Department of Structural Engineering

ISBN 978-82-326-2708-0 (printed ver.)
ISBN 978-82-326-2709-7 (electronic ver.)
ISSN 1503-8181

Doctoral theses at NTNU, 2017:320

Printed by NTNU Grafisk senter

Preface

The present doctoral thesis has been submitted to the Norwegian University of Science and Technology (NTNU) in partial fulfilment of the requirements for the degree of Philosophiae Doctor (Ph.D.). This work has been carried out at the Department of Structural Engineering, NTNU, Trondheim and supervised by Professor Kjell Arne Malo. The work was funded by the WoodWisdom-Net+ project DuraTB ("Durable Timber Bridges").

This thesis is paper based and contains three parts. Part I is an introductory section, Part II includes five appended papers, and Part III consists of 2 appendices.

Acknowledgements

This work was funded by the WoodWisdom-Net+ project DuraTB (“Durable Timber Bridges”), and the support from the funding bodies and partners is gratefully acknowledged.

I would like to acknowledge my supervisor Professor Kjell Arne Malo for all his suggestions and guidance through the Ph.D. study period. Your critical proofreading of my manuscripts increased the quality of my work considerably. I also deeply appreciate the provided opportunity of working on the international project of Durable Timber Bridges.

Many thanks go to my colleagues, the fellow Ph.D. students at the department of Structural Engineering at NTNU. The way towards a doctorate is specific in many aspects, and I am very thankful for being a part of such a helpful and friendly environment. Special thanks go to Mirko Massaro for all our discussions and spell checking of my manuscripts. Truly, coming back to study duties (exams!) was much easier thanks to sharing the office with you!

I would like to thank Michele Baravalle and Professor Kolbein Bell for critical feedbacks on my manuscripts. Thanks to Haris Stamatopoulos for sharing his technical experience and Anna Ostrycharczyk for sharing her numerical model.

I appreciate all the assistance I have received from the laboratory staff. Thank you Odd Nerdahl, Pål Rike, Ragnar Moen, Steinar Seehuus, Terje Petersen and Christian Frugone for always being ready to help. My thanks also go to Hallvard Oltedal Veium, Mathias Strøm, Christoffer Aune Moe, Halvor Grytting and Eirik Dimmen Sæle who assisted with the experimental investigations as a part of their master projects.

This work would never be possible without receiving so much patience and support from my wife Betka and so much energy from my son Marek. We have taken the journey together, and this thesis is as much your, as my achievement.

Abstract

The use of glued laminated timber (glulam) enables timber elements having nearly unlimited cross-sectional dimensions. Owing to the favourable strength-to-weight ratio compared to steel and concrete, glulam is well suited for structures with large spans. Feasibility studies of glulam arches with network hanger configuration have shown that road timber bridges with spans reaching 100-120 m feature excellent structural properties and can be designed for full traffic loading. Massive glulam arches of such lengths must be spliced on the bridge site. The splice joints must feature high flexural rigidity in order to maintain the stability of the arches. Nevertheless, the available state-of-the-art timber splicing techniques do not provide the required joint features. Therefore, an innovative splicing technique is investigated and proposed in this work.

The novel splicing technique utilises the large withdrawal stiffness and strength of long threaded rods. Two alternatives are proposed. In the first alternative, commonly available threaded rods are embedded in timber parallel to the grain. The mutual splicing of the rods is carried out by grout-filled steel couplers, which are fully embedded in timber. In the second alternative, purpose-made threaded rods with metric threads at one end are used with a small inclination to the grain. The metric threads enable a fast on-site joint assembly by a simple mechanical coupling, whereas the inclination to the grain prevents potential shrinkage cracks in timber along the rods.

The flexural performance of the joint was experimentally investigated on prototype splice joints. The joints featured a large rotational stiffness without initial slip. A ductile steel failure was achieved by providing a sufficient embedment length of the rods. Numerical simulations by finite element models enabled a deeper insight into the mechanical behaviour of the tested connections as well as the execution of parametric studies. The finite element models simulated the flexural behaviour of the joint effectively. As a basis for practical joint design, analytical models validated by the experiments are proposed for determining the rotational stiffness, the moment capacity and the capacity under combined action of bending and normal force.

Two additional investigations were carried out in order to obtain input parameters to the analytical models. In the first investigation, the effect of rod-to-grain and load-to-rod angles on capacity and stiffness of threaded rods were studied. In the second investigation, stiffness and capacity were examined for the interface zone of two mutually compressed timber end faces in a direct timber-to-timber contact in comparison to a timber-steel-timber arrangement.

Finally, the effect of splice joints on the stability of timber network arch bridges was assessed using numerical models. The results indicate that the proposed splicing technique provides a sufficient rotational stiffness to ensure the stability of the timber arches.

In conclusion, the introduction of an effective splicing technique enables the construction of timber bridges with massive glulam arches, which represents a more durable and cheaper alternative to the currently used truss arches. The present research work gives a theoretical basis for the further industrial development of the proposed prototype joints and potential implementation on the market.

Keywords: glulam, long threaded rod, splice joint, network arch bridge, rotational stiffness, moment resistance, experimental testing, analytical model, 3D finite element model

Table of contents

Part I: Introduction, background and overview of the present work

1 Introduction 1

1.1 Motivation and problem statement 1

1.2 Objectives.. 3

2 State-of-the-art connection techniques 7

2.1 Slotted-in steel plates and dowels 7

2.2 Glued-in steel rods 10

2.3 Glued-in steel plates 14

2.4 Glued connection 15

2.5 BVD anchor bolt connection 16

2.6 Self-tapping screws 17

2.7 Lagscrewbolts... 20

2.8 Concluding remarks 22

3 Background for long threaded rods as connectors in timber joints 24

3.1 Dimensions and materials.. 24

3.2 Withdrawal (axial) capacity and stiffness 26

3.3 Combined axial and lateral loading... 31

3.4 Prototype joints with LTRs 31

4 Overview of the present work..33

4.1 The proposed splicing technique 33

4.2 Scope of the research work – Publication list.. 37

4.3 Research methods 38

4.4 Limitations.. 41

4.5 Main results and conclusions... 41

4.6 Proposals for future work 47

5 Declaration of authorship 50

6 References..51

Part II: Appended Papers

i. **Moment resisting splice of timber beams using long threaded rods and grout-filled couplers – Experimental results and predictive models**
Martin Cepelka, Kjell Arne Malo
In: Construction and Building Materials (2017),
https://doi.org/10.1016/j.conbuildmat.2017.08.089

ii. **Effect of rod-to-grain angle on capacity and stiffness of axially and laterally loaded long threaded rods in timber joints**
Martin Cepelka, Kjell Arne Malo, Haris Stamatopoulos
Under review in an international scientific journal (2017)

iii. **Moment resisting on-site splice of large glulam elements by use of mechanically coupled long threaded rods**
Martin Cepelka, Kjell Arne Malo
Under review in an international scientific journal (2017)

iv. **Experimental study of end grain effects in timber joints under uniaxial compression load**
Martin Cepelka, Kjell Arne Malo
In: Proceedings of the World Conference on Timber Engineering (WCTE 2016), Vienna (2016)

v. **Effect of on-site splice joints for timber network arch bridges**
Martin Cepelka, Kjell Arne Malo
In: Proceedings of the International Conference on Timber Bridges (ICTB 2017) Skellefteå (2017)

Part III: Appendices

A. Analytical description of splice efficiency

B. Derivation of the resultant stiffness of axially and laterally loaded LTRs

Abbreviations

Glulam	Glued-laminated timber
EC5	Eurocode 5: EN 1995-1-1
ULS	Ultimate limit state
SLS	Serviceability limit state
STS	Self-tapping screw
CLT	Cross-laminated timber
LSB	Lagscrewbolt
LTR	Long threaded rod
MC	Moisture content
LVDT	Linear variable differential transformer (displacement transducer)
DIC	Digital image correlation
CNC	Computer-Numerical-Control (cutting machine)

Part I:
Introduction, background and overview of the present work

1 Introduction

1.1 Motivation and problem statement

The development of glued laminated timber (glulam) and block gluing, where elements are in parallel, enables the production of timber elements with nearly unlimited cross-sectional dimensions. The fact that glulam has an excellent strength-to-weight ratio, compared to steel and concrete, promotes glulam to be used in structures with large spans.

The Tynset Bridge in Norway, illustrated in Figure 1.1a, represents an example of a modern large road timber bridge with a total length of 125 m. The bridge consists of 3 glulam single-span arches. The main truss arch has a span of 70 m, and it supports the bridge deck through vertical hangers. A feasibility study presented in [1] shows an alternative design of the main arch with inclined, mutually crossing hangers. For such a configuration, commonly denoted as network arch bridge [2], both bending moments and shear forces in the arch decrease considerably, allowing the arch to be designed as a massive glulam cross section. It is estimated that for the Tynset Bridge, the solution with massive arches would require about 55 % less timber compared to the current solution with trusses [1]. Additional saving in costs would be obtained by the substantially lower number of connections.

Connections exposed to outdoor conditions suffer an increased probability for decay development due to moisture exposure and limited drying possibilities. Conferring Figure 1.1a, it is obvious that detailing of cladding at the lower chord of the Tynset Bridge is cumbersome and any completion inaccuracy may potentially lead to water leakage into the joints. The massive glulam arches provide a more durable design by featuring a simple geometry and lower number of connections, compared to the truss arches.

Figure 1.1 Large road timber arch bridges in Norway: (a) the Tynset Bridge (2001), (b) the Steien Bridge (2016) [3], (c) detail of the arch of the Steien Bridge [3]

Figure 1.1b shows the recently erected Steien Bridge in Norway [4]. With a span of 88 m, the bridge is currently the longest single-span road bridge with a timber load-bearing structure in the world. Similar to the Tynset Bridge, the arches of the Steien Bridge are formed as trusses consisting of a hybrid timber-steel structure, with the chords of timber and the diagonals of steel, as illustrated in Figure 1.1c. Clearly, the number of connections is large.

Despite the record spans of the Tynset Bridge and the Steien Bridge, feasibility studies of glulam arch bridges with network hanger configuration [5, 6] have even shown excellent structural properties for road bridges with massive glulam arches of spans up to 100-120 m. However, since the timber arches cannot be produced and transported in one piece, the timber elements must be connected on the bridge site by splice joints (in some literature also defined as end joints or butt joints). In order to maintain stability and reduce buckling problems of the arches, the splice joints must feature a sufficiently large rotational stiffness [7, 8].

Additional requirements on durability, cost-effectiveness and mounting efficiency on the site make the use of the currently available timber joining techniques precarious. Thus, it is believed that the main reason behind the currently used truss-like solution is the lack of a suitable on-site splicing technique for large timber elements rather than the structural performance of the arches themselves.

The development of a splicing technique suitable for large glulam elements of network arch bridges is the main scope of the present research work. The introduction of an effective splicing technique enables the construction of timber network arch bridges with massive glulam arches, which represents a more durable and cheaper alternative to the currently used truss arches. A possible layout of a timber network arch bridge with massive glulam arches is illustrated in Figure 1.2.

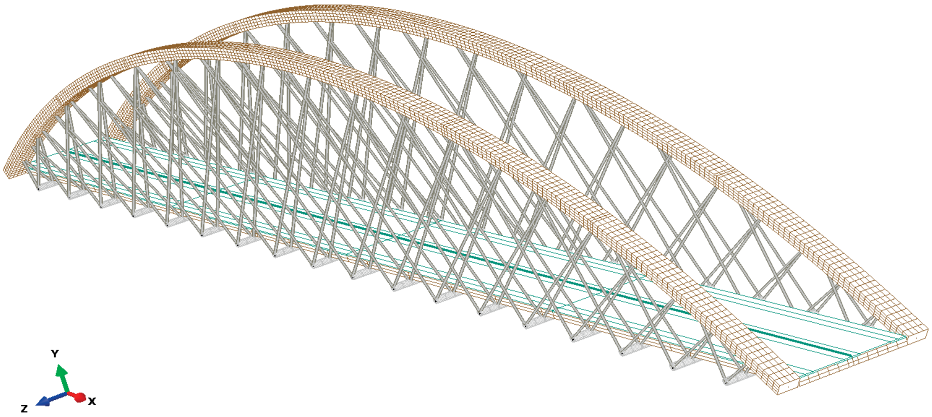

Figure 1.2 Illustration of a network arch bridge with massive glulam arches

1.2 Objectives

The main objective of the present work is the development of a suitable joining technique for on-site splicing of large glulam arches in timber bridges. The flexural behaviour of the splice joint is the main focus since a sufficient rotational stiffness and moment capacity represent the primary prerequisites for the possible practical application of the joint.

The splice joints in timber arches should feature the following primary qualities:

- Sufficient strength and stiffness
- Durability
- Fast, easy and reliable assembly (cost competitiveness, production tolerances and quality control)

Sufficient strength and stiffness

Strength - Design at Ultimate Limit State (ULS)

The joint should be designed to withstand the action of the acting internal forces and their interactions. Care must be taken to the shifting sign of internal forces (e.g. tension/compression or orientation of bending moments) caused by the position of the traffic load on the bridge, combined actions of wind and traffic load, and specific load cases in the erection phase.

Rotational stiffness and ductility

In order to maintain stability and reduce buckling problems of the spliced massive timber arches, the joints must feature a sufficiently large rotational stiffness without initial slip.

For statically indeterminate structures, the distribution of internal forces is affected by the stiffness of joints [9]. Therefore, the joint stiffness has to be considered in the global structural models for the calculation of internal forces (ULS), as well as serviceability verifications (SLS) and stability assessments. Eurocode 5 (EC5) [10] defines that the joint stiffness for ULS verifications should be assumed equal to 2/3 of the characteristic (initial) joint stiffness used for assessments in SLS.

The initial slip of joints can hardly be analytically quantified. Consequently, the additional deformation caused by the initial slip makes the global analysis unreliable. Therefore, the absence of the initial slip is an important prerequisite for moment resisting connections.

A ductile failure mode in joints is preferred due to the development of significant (plastic) deformations before the failure occurs. The brittle failure is, on the contrary, characterised by a sudden failure without “warning” before the collapse.

Detailing with respect to moisture induced stresses

The change of moisture content in wood causes shrinkage and swelling deformations. Due to the anisotropy of wood, these moisture induced deformations are typically 5-10 times larger in directions perpendicular to the grain than parallel to the grain [11]. The presence of steel fasteners may restrain the moisture induced deformations, and it may thus cause moisture induced stresses in the timber cross-section. Such stresses are often negligible in the direction parallel to the grain, where the strength is also high. However, in the direction perpendicular to the grain, the moisture induced stresses are significantly larger, and together with the low strength in this direction, this can initialize splitting in the joint area. Due to the strong moisture transport mechanism in the grain direction, the joints in timber bridges are susceptible to moisture variation, being located close to the end grain.

Detailing with respect to fatigue

For joints in road and railway bridges, fatigue assessment should be carried out. The fatigue issue of timber is a relatively new research area. A simplified verification method is provided by Annex A of EN 1995-2 [12]. An overview over the fatigue problem in timber and some preliminary results of a currently ongoing research at NTNU can be found in [13, 14]. The fatigue assessment of steel parts in joints is covered in detail by design codes, such as EN 1993-1-9 [15].

Durability

Connections in timber bridges suffer an increased probability for decay developments due to moisture exposure and limited drying possibilities. A splice joint in a large timber bridge is difficult to inspect, and the repair possibilities are very limited. The joint should, therefore, be designed to have a lifetime corresponding to the required lifetime of the members of the load-bearing structure [16]. The durability of timber bridges is discussed in detail in [13]. For joints, a proper detailing is essential and following recommendations should be respected:

- Preferably, the joint region should be kept dry, and it should be allowed for a fast drying through ventilation.
- Any form of free standing water and spaces where dirt can accumulate should be avoided in contact with timber surface.
- Steel parts in the connection should be anti-corrosion treated such that the maintenance is not necessary (use of galvanised or stainless steel).
- The upper faces of timber members should be covered (application of cladding at side faces of timber members is also favourable).
- The end faces of timber members should be well protected from leaking water because of the strong moisture transport mechanism in the grain direction.

2 State-of-the-art connection techniques

In the following, several state-of-the-art connection techniques with a possible application for splicing of large glued laminated elements of timber arch bridges are shortly introduced.

2.1 Slotted-in steel plates and dowels

In this commonly used connection technique, timber elements are connected via steel plates which are mounted to timber by dowel type fasteners. Steel plates can either be placed externally (forming steel brackets) or slotted into timber members. The use of the steel brackets is, due to durability issues, not recommended for bridges because of the limited moisture dry-out in the interface between the steel plates and the timber surface. Weathering exposure of the steel/timber interface is omitted by slotting steel plates into the timber elements. The connection technique using slotted-in steel plates and dowels has widely been used in modern timber bridge design. The joint is usually built up of several steel plates of thickness 8 or 10 mm and dowels of diameter 10, 12 or 16 mm [16].

The technique is commonly used to carry axial and shear forces, as for example in nodes in truss structures and hinges in arches. A typical example of a truss joint is shown in Figure 2.1. The gap between the end faces of elements is filled with acrylic mortar, which allows the transfer of compression force and protects the end faces from moisture.

In contrast to joints transferring axial and shear forces, there are not many examples of splice joints carrying bending moments. Figure 2.2 shows a moment resisting splice joint used in the Leonardo Footbridge, in Norway. Slotted-in steel plates and dowels at the top and the bottom edges together with a shear key placed in the middle of the section are used to carry bending moments and shear forces, respectively. The shear key is designed as a welded steel gusset connected to the timber by a combination of transversal dowels and rods glued from the end face.

The axial compression force is transmitted by the contact of the end faces since the gap between elements is filled with acrylic mortar. Weathering degradation and creep of acrylic mortar are common concerns because the additional contraction of the mortar overloads the dowels, which are not designed to carry the axial force. Regular inspection of the joint is, therefore, important. The upper sides of the arches of the Leonardo footbridge were eventually protected by metal cladding to prevent water from leaking into possible gaps or cracks.

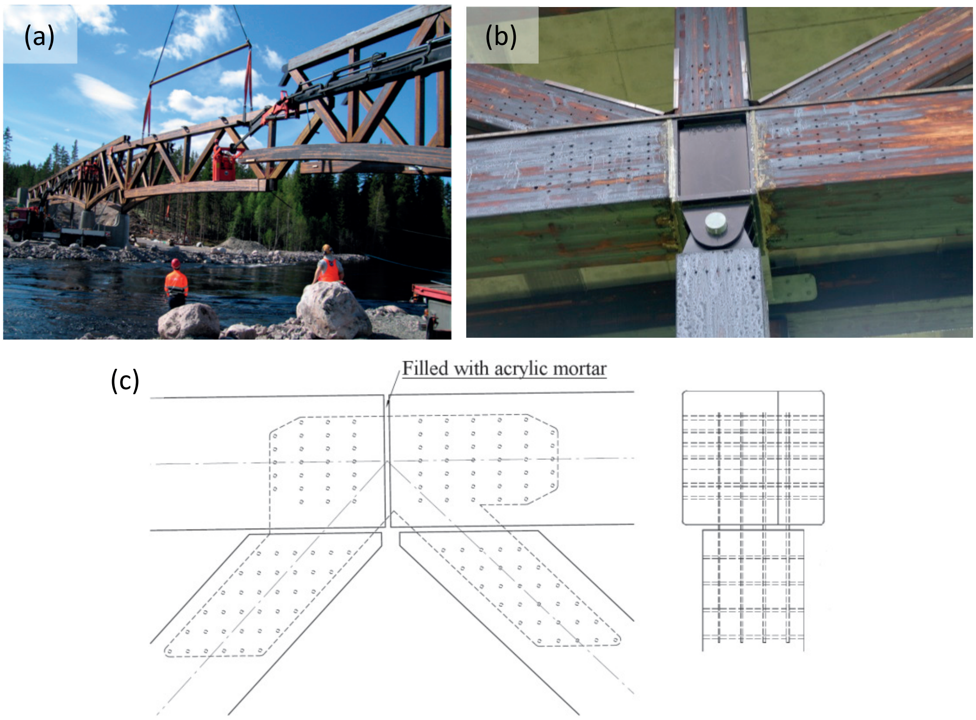

Figure 2.1 The Kjøllsæter Bridge (2005), Norway: (a) truss structure under assembly, (b) detail of joint at the lower chord, (c) drawing of a connection at the top chord; source: (a) and (c) Moelven Limtre AS and Sweco AS

When transmitting bending moments, dowel-type fasteners impose concentrated local forces in timber with an angle to the grain [17]. The bending resistance is then governed by a combination of tension perpendicular to the grain and longitudinal shear stresses – the two weakest strength properties of wood. The failure mechanism by tension perpendicular to the grain, the so-called “splitting”, is related to the fastener slenderness (ratio of the embedded length in timber to the diameter of the fastener) and to the number of fasteners in a row parallel to the grain. The probability of splitting is larger for less slender fasteners and a higher number of fasteners in a row.

The failure mode by splitting is brittle and very low ductility of connection may occur. In order to prevent the brittle splitting failures, adequate spacing and end distances of fasteners must be ensured. The fulfilment of the requirements for the spacing often leads to a large area of connections, which may result in increased timber dimensions. Generally, a higher number of thinner plates and a smaller diameter of dowels provide a smoother stress distribution and a more ductile behaviour.

Figure 2.2 The Leonardo Footbridge (2001), Norway: the central arch under assembly (left), visualisation of the splice joint (right)

The splitting tendency can also be initiated by shrinkage cracks. Experiments in [18] showed that load carrying capacity of joints with slotted-in steel plates and dowels is reduced due to moisture induced stresses perpendicular to the grain. An increased spacing between the dowels in a perpendicular-to-grain direction (and thus increase of the joint size) resulted in an amplified effect of the reduction of load-carrying capacity and increased the occurrence of moisture induced cracks.

For moment resisting connections, stiffness and ductility play major roles. The effective joint stiffness is decreased by an initial slip. Although the holes to accommodate dowels should be tight-fitting to minimise clearances, material tolerances and requirements to fast mounting make the tight-fitting unreliable.

Moreover, if a dowel fits too tight in a hole, splitting can be initiated. Consequently, the initial slip is often observed in joints with dowel-type fasteners.

A reinforcement perpendicular to the grain can reduce the splitting, thus ensure ductility and reduce the required spacing of dowels. The load-carrying capacity is also increased considerably, see e.g. [19, 20]. Recent research reports an excellent reinforcing effect of self-tapping screws (STSs) applied perpendicular to the grain. Lam et al. report in [21] an increasing capacity of column-joist connections by a factor of 2 and observe a ductile failure mode. Splitting did not occur in any specimen, even for a cycling loading. The failure mode was a plug-shear on the tension side of the beam. This indicates that the screws have the capacity to carry imposed stresses perpendicular to the grain, thereby changing the failure mode to parallel-to-grain failures. Later, the effects of increased bolt dimensions and decreased edge distances were studied in [22]. The results showed an amplifying effect of the reinforcement and thus an additional increase in capacity while maintaining the ductile behaviour. Brühl et al. report in [23, 24] a highly ductile behaviour and an increased rotation capacity of splice connections with slotted-in steel plates and dowels reinforced by STSs. Furthermore, tensile tests of STS-reinforced splice joints showed that the effective number of fasteners was equal to the installed number, and hence that it is not necessary to reduce the number of fasteners in rows parallel to the grain as currently required in EC5.

2.2 Glued-in steel rods

Another widely used timber connection technique is facilitated by using rods glued into predrilled holes in timber. Usually, steel rods and epoxy adhesives are used, but other materials such as rods from fiber-reinforced polymers and adhesives of polyurethane are becoming common as well [25-27]. The rods are fully embedded in timber members and, thus, protected. Since the adhesive fills the pre-drilled holes entirely, there is no clearance between the rods and the wood. As a result, the initial slip is avoided.

The most effective force transfer is obtained for axially loaded rods by shear stresses continuously distributed along the rods. Large stiffness and pull-out capacity can be achieved by using high strength adhesives. However, for large joints, multiple rods are necessary, and the brittleness of the adhesives can lead to a progressive failure in a group of rods [26]. Therefore, the ductile pull-out behaviour of the rods is important. In addition, the joint ductility is also required in seismic areas. The ductility is usually achieved by the plastic deformations of the rods, provided by: use of low-grade steel bars, glue-free zones, and zones with a reduced cross section of the rods [28-32].

Figure 2.3 Splice joint with glued-in rods: rods glued into one member of the joint (left), deformation of the joint (right), [28]

The main shortcoming associated with the application of glued-in rods is the production. In the example shown in Figure 2.3, the rods were put inside holes using a wire-guide to centre them. The epoxy was injected through grouting channels drilled to each embedment hole near to its end. The effectiveness of the grouting operation cannot be visually checked. Experience from reviewers of failed joints revealed inadequately mixed and incorrectly applied epoxy on site. Nowadays, the production is limited to a climate controlled environment with quality control and skilled personnel [26].

A joining technique combining glued-in rods and pinned steel connections is presented in [29]. The principle of this so-called GSA®-technology is shown in Figure 2.4. Rods are glued to timber sections in factory conditions with welded or screwed special steel pin-joint at the end. Thus, a pinned steel-to-steel connection is created with an effective on-site mounting. The ductile behaviour is achieved by a combination of low-grade steel and pre-defined glue-free deformation zone of the rods. The plastic deformation of the rods can thus absorb the eventual uneven distribution of forces in a group of rods.

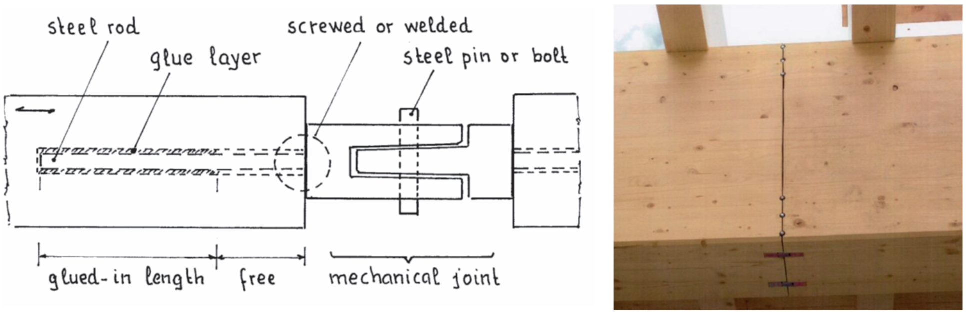

Figure 2.4 GSA®-technology: illustration of joint principle (left), moment resisting splice of a glulam beam (right), [29]

The rods can be positioned at skewed angles to grains in order to increase the lever arm of internal forces in moment resisting connections and to prevent a potential loss of capacity due to shrinkage cracks along the rods. An example of a splice joint by this so-called V-connection technique [33-35] is shown in Figure 2.5. The glued-in ribbed steel rods are grouped in couples that are welded to connecting steel rods or plates. By using the glued-in rods in couples, the transversal bending of the rods is minimised, since the load is mainly distributed to the rods as the axial tension and compression.

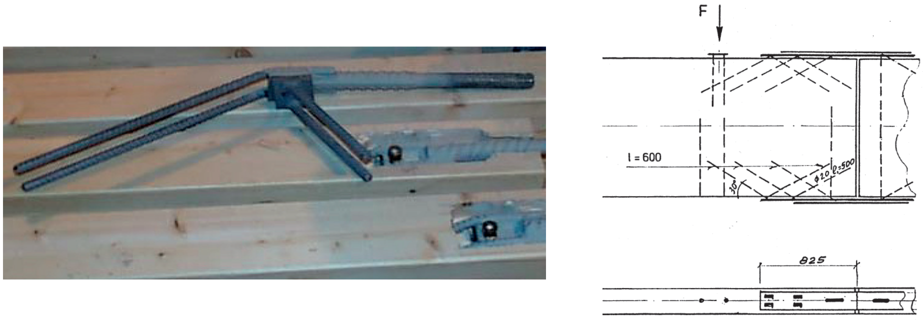

Figure 2.5 V-connection with glued-in rods: glued-in rod couples welded to a connecting steel rod (left), experimentally investigated beam splice (right), [33]

An example of a splice joint by glued-in rods placed in the apex of a 2-hinged arch road bridge is shown in Figure 2.6. The span of the bridge is 33.4 m, and no bracing (wind truss) is used between the two arches leading to bending moments in the splice joint both in the in- and the out-of-the plane direction of the arches. The glulam arches were finally protected by cladding applied both at the top and the sides.

Figure 2.6 Example of application of glued-in rods in the apex of an arch bridge, Kirchenbrücke, 2009, Switzerland, [36]

Connections with glued-in rods present complex systems with complicated stress distributions since three different materials with distinctly different properties are combined. Some design models for predicting rotational stiffness and moment capacity of splice- and end-joints with glued-in rods are proposed e.g. in [37-41]. The current state of design, research and industrial applications are reported in [42] and [43] on the basis of comparison of design rules and an online survey sent to scientists, timber industrialists and structural designers all over Europe. It is concluded that, despite many research projects (the European GIROD project was probably the largest [25]), there are still various issues that have not been clarified and where a common agreement has not been reached. As a result, there are still no universal design rules and technical guidelines. In 2003, it was decided to discard the Annex C in Eurocode 5-part 2 [12], which was dealing with the design of glued-in rods. There are, up to date, no design rules in the current (2017) version of Eurocode 5 [10].

2.3 Glued-in steel plates

An alternative solution to the connections with slotted-in steel plates and dowels and to the connections with glued-in rods is obtained by gluing steel plates into slots in timber. The solid steel plates have a larger cross-sectional area compared to rods, and the glued connection is stiffer than the traditional dowel-type connections. As a result, large capacity and stiffness can be achieved. Valée et al. [44] performed full-scale tests of timber trusses with connections by slotted-in steel plates and dowels and by glued-in solid steel plates. The trusses with glued-in steel plates featured about 40 % higher capacity and 300 % higher stiffness. However, similar to joints with glued-in rods, the bond efficiency and the failure brittleness (see Figure 2.7 left) are the major concerns for joints with glued-in solid steel plates. The glued-in rods are usually manufactured with threads or ribs. The force transfer is thus realised to some extent by a mechanical interlock between the rods and the adhesives. The glued-in solid steel plates rely, on the contrary, solely on force transfer by adhesion, which depends largely on the surface preparation by degreasing of the steel plates [45].

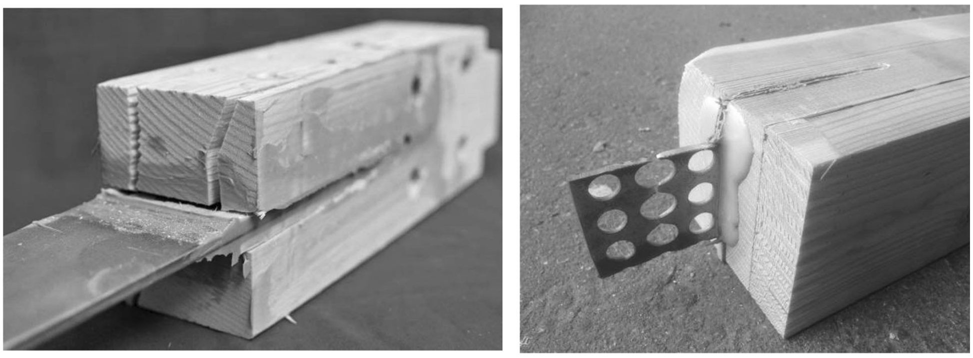

Figure 2.7 Glued-in steel plates: solid plate (left), perforated plate (right), [45]

The aforementioned shortcomings can be overcome by the use of glued-in perforated steel plates, also known as HSK^{TM} system (Holz-Stahl-Komposit-System) [45-48]. The perforations in the plates create cavities that are filled with an epoxy adhesive and form a kind of “adhesive dowels”. The force transfer is thus carried out by mechanical “dowel connectors”, which transfer the load between the steel plates and the connected timber members. A ductile steel failure can be obtained by a design enforcing the perforated steel plates being the weakest part of the connection, see Figure 2.7 right. The perforated plates were successfully used in splice joints of a timber wind tower in Hannover with a total height of 100 m. Bathon et al. [46, 47] reported a fatigue performance of the adhesive resisting up to 10 000 000 load cycles.

2.4 Glued connection

A splicing technique under trademark HESS LIMITLESS was presented by Aicher et al. in [49, 50] and it is covered by German and international patents. The joint is formed by a combination of large finger joint, wedge shaped fitting and high premium (P-) laminations. Currently, the maximum height of the cross section is 2 m. According to the manufacturer, the load bearing efficiency of the joint in in-plane bending and shear is as high as 100 %.

The splicing technique is illustrated in Figure 2.8. The wedge shaped fitting with height H/6 (where H is the height of the entire cross section) is placed at the tension edge of the section, and it is glued to the bottom parts of both the connected members. The remaining 5H/6 height of the cross section is joined by a large finger joint.

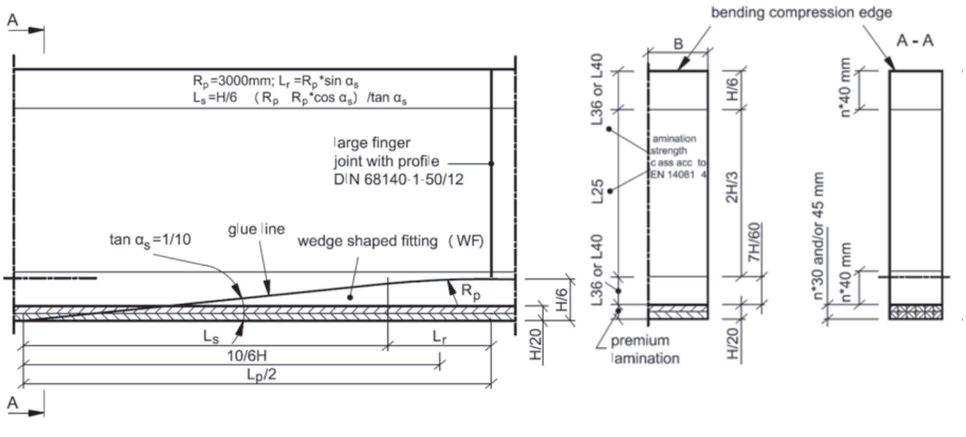

Figure 2.8 Illustration of the principle of large glued splice joint, [50]

In the case of loading by tension or compression parallel to the grain or out-of-plane bending, the wedge shaped fitting must be placed on both edges. The joint efficiency is consequently decreased to approximately 85 %.

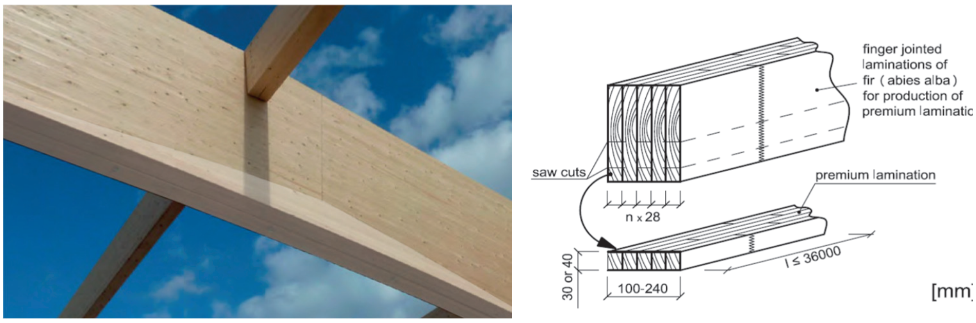

Figure 2.9 Details of a large glued connection: assembled spliced beam (the wedge shaped fitting is highlighted) (left) [51], premium laminations (right) [50]

The outermost tension edge of both the beam and the wedge shaped fitting is made of so-called Premium (P-) laminations. As shown in Figure 2.9 right, the P-laminations consist of parallel-arranged finger-jointed fir laminations. The required bending and tensile strength are $f_{m,k} \geq 45$ MPa and $f_{t,k} \geq 29$ MPa and mean MOE in tension is equal to $E_{0,mean} = 12500 \pm 500$ MPa.

Although the glued connection is very efficient in terms of capacity and stiffness, the main drawback is the production difficulty. High precision in manufacturing is required for cutting and gluing the large finger joint. The production on site must, therefore, take place in climate controlled and specially equipped tents.

2.5 BVD anchor bolt connection

The connection consists of cylindrical steel or gusset anchor bolt (on the market also known as BS-connector) and orthogonally placed dowels in 2 directions, see Figure 2.10. The dowels are placed in half-circular holes in the anchor bolt, and a rigid load transfer is achieved by injection of a high-strength, non-shrinking cement grout via an infill hole in the anchor bolt. Depending on the required capacity, the anchor bolts differ in length, diameter and amount of incorporated dowels (4-24 pieces). Several anchor bolts can be placed in parallel in large joints, which is, however, not covered explicitly by the technical approval at present [50]. The load is transferred from timber members via dowels to the anchor bolt, which is consequently loaded by an axial tension or compression force. The German building approval specifies that BVD anchor bolt connections shall not be loaded by a shear force, except from the self-weight of timber members.

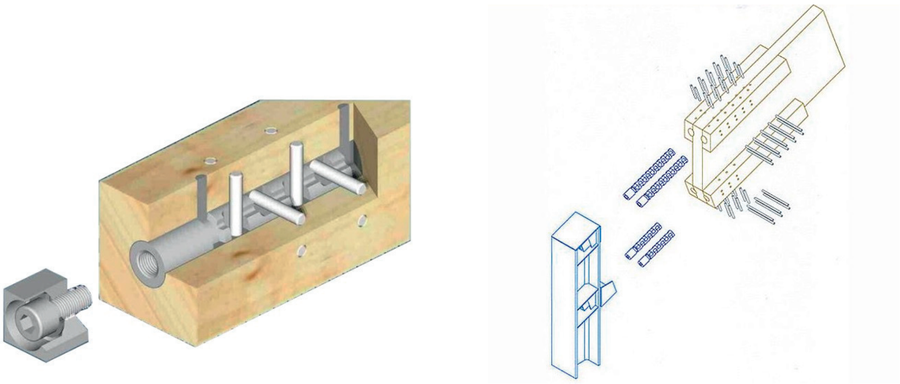

Figure 2.10 BVD anchor bolt connection – an example of use in a hybrid steel-timber joint [52]

Compared to connections with slotted-in plates and dowels, a higher capacity is achieved due to a more effective load transfer, achieved by the two-directional placement of dowels. The efficiency, in terms of net cross-sectional area, is also larger since the predrilled holes for the anchor bolts occupy a smaller area than the slots for steel plates. The anchor bolts are fully embedded in timber, and there are no slots in the upper and lower faces of timber, through which water could leak into timber as in the case of slotted-in plates. However, the common failure mode of the connection is, alike for all dowel-type fastener connections, governed by the premature splitting of timber caused by tensile stresses perpendicular to the grain [50].

2.6 Self-tapping screws

Self-tapping screws (STSs) are characterized by full threads and hardening after rolling the thread. Hardening increases tensile strength and thus bending and torsion capacity. STSs are usually manufactured up to a diameter of 14 mm and used without pre-drilling of holes (the pre-drilling is, however, recommended for larger diameters, especially when applied parallel to the grain [53]).

STSs feature large withdrawal and pushing-in resistance for axial loading. On the contrary, the transversal capacity of the screws is rather low due to their slenderness. Proper positioning of the screws, relative to the direction of the loads, is thus essential concerning the optimisation of both load-carrying capacity and stiffness of the connection. The effect of the screw inclination relative to the loading is demonstrated for a simple lap joint transferring a tensile force by Blaß in [54, 55]. It is concluded that connections with the screw-to-load angle of 45˚ show an increase of 50 % of the load-carrying capacity and an increase of the slip modulus by a factor up to 12, compared to the screws loaded perpendicular to their axes. The failure mechanism is shown in Figure 2.11. In the left, the force is mainly transferred by an axial withdrawal force in the screws and a compressive force component between the timber members based on a truss-like system equilibrium. In the right, the load-bearing capacity is governed by the bending capacity of the screws and the timber embedding strength.

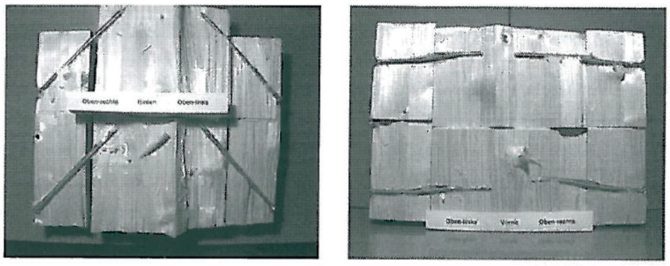

Figure 2.11 Deformation of a tensile lap joint with STSs: load-to-screw angle 45˚ (left), load-to-screw angle 90˚ (right),[55]

Great performances of STSs as a reinforcement to carry tensile stresses perpendicular to the grain and shear stress in glued laminated timber have recently been well documented by the current research, see e.g. [56]. Some possible design solutions of tensile splice joints of lap timber connections and steel-to-timber lap connections with STSs are given in [55, 57-60]. Recently, STSs have also been applied as fasteners in moment resisting connections. An example of a large moment resisting splice joint is illustrated in Figure 2.12. The joint is used to connect three assembly parts of timber girders with a total span of 69 m in Saint-Michel Environmental Complex Soccer Stadium in Montreal in Canada [61]. The girders consist of glulam flanges and cross-laminated timber (CLT) webs. The lower tensile flange is spliced by the use of 416 screws of 14 mm in diameter and 550 mm in length, placed parallel to the grain at each side of the connection.

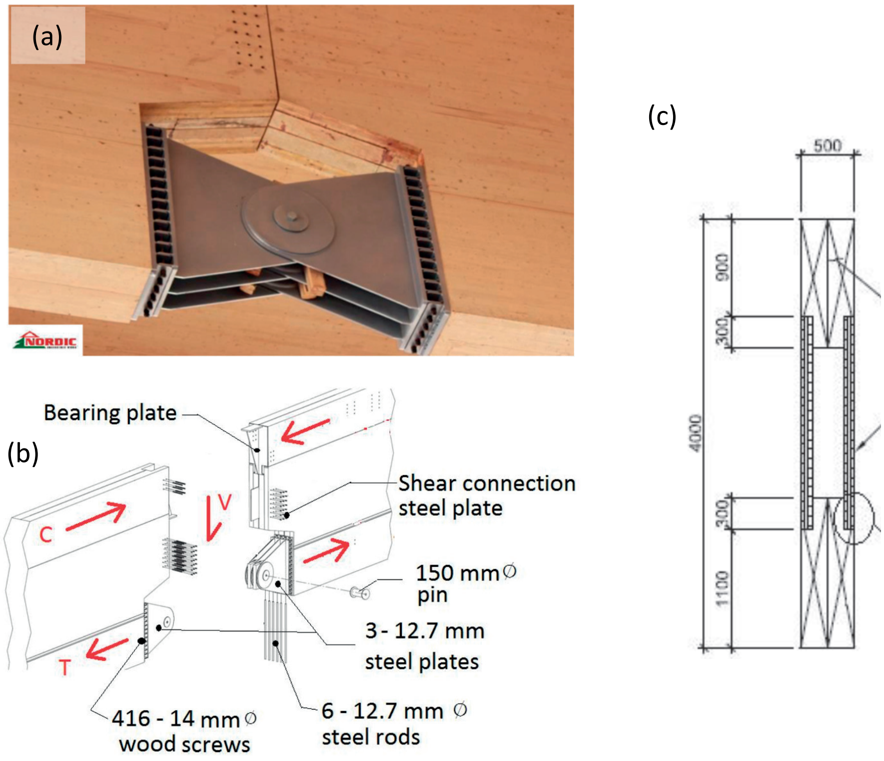

Figure 2.12 Splice joint of a large timber beam with STSs, CESM Soccer Center in Montreal, Canada [61, 62]: (a) detail at the lower flange after assembly, (b) schematic illustration of the joint, (c) girder cross section

Another example of a moment resisting connection with STSs favourably utilising the strong axial withdrawal resistance of the screws is achieved by using the so-called tension and compression plates (on the market also known as ZD-plates). The plates distribute the load to the screws in a force couple, such that each screw is loaded by either axial tension or compression. The principle of the connection is demonstrated in Figure 2.13 on the trademarked SWG system. Screws are driven into timber under an angle of 30˚ via a "base-part" of the ZD-plate. Thereafter, a "top-part" is applied, through which the ZD-plate is bolted to a steel bracket.

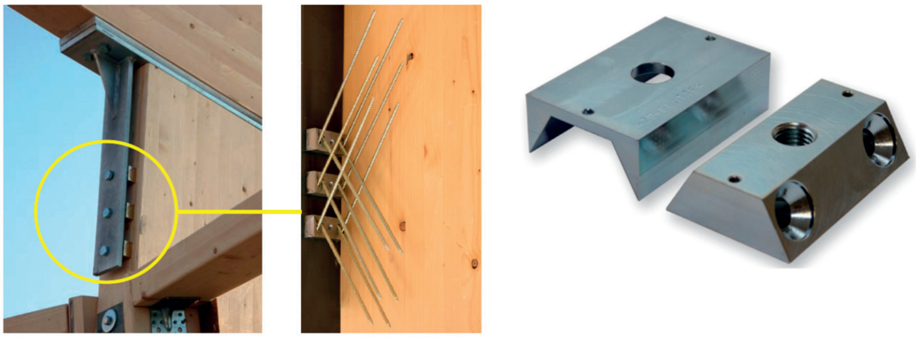

Figure 2.13 Joint with ZD-plates and STSs screws [63]: portal frame joint (left), detail of screw assembly (centre), ZD-plate (right)

An experimental study on moment resisting joist-column connection with STSs and ZD-plates [64] showed high moment capacity and very stiff behaviour. However, a relatively low ductility of the connection was observed. The connection ductility was later improved in [65] by the application of massive ductile steel links inserted between the columns and the joist.

2.7 Lagscrewbolts

Lagscrewbolts (LSBs) have been developed as connectors for moment resisting joints of glulam structures in Japan [31, 66-68]. LSBs have an external wood thread as lag screws and one end formed as a metric thread (internal or external) allowing easy on-site assembly, see examples in Figure 2.14. The outer diameter of the wood thread is in the range of 14-35 mm.

Figure 2.14 Examples of lagscrewbolts [66]

Examples of LSB applications for column-beam connections are illustrated in Figure 2.15. In typical beam-column joints, the LSBs are embedded perpendicular to the grain in columns and parallel to the grain in beams. The withdrawal of LSB parallel to the grain features large capacity and stiffness. However, both the shear failure of columns and the withdrawal failure of LSB from beams are very brittle [68]. In order to fulfil the requirements in seismic areas, the ductility of the joint is controlled by ensuring the yielding of the connecting bolts or other steel parts [31].

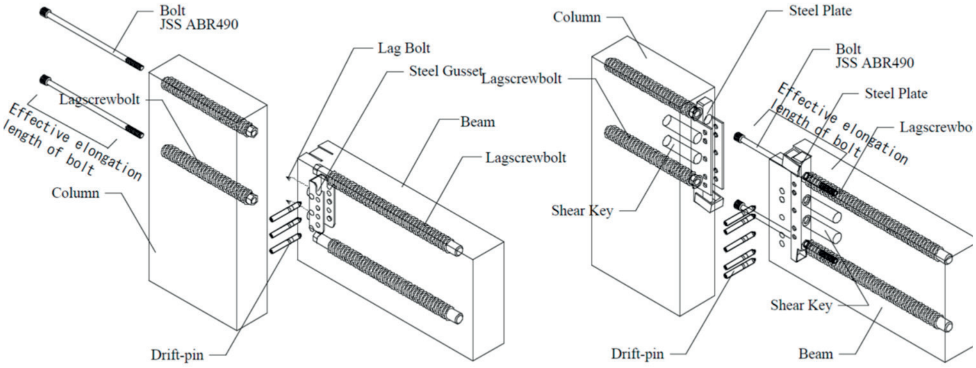

Figure 2.15 Beam-column joints with lagscrewbolts [31]

2.8 Concluding remarks

The reviewed state-of-the-art connection techniques are characterised by different pros and cons. In the following, a brief evaluation is given regarding the suitability for the splicing of timber arch bridges as defined in Section 1.2:

- The key prerequisite for the splicing of arch bridges is a large and reliably predictable rotational stiffness without initial slip. The rotational stiffness of timber joints is mainly governed by the load-slip behaviour of the individual fasteners. Due to a more uniform force transfer between timber and connectors, axially loaded fasteners (screws, glued-in rods and plates) feature higher stiffness and lower initial slip compared to the dowel-type fasteners (bolts, dowels) [17]. Moreover, the reliability of the prediction of the rotational stiffness of the joints with dowel-type fasteners is doubtful due to the presence of the initial slip caused by clearances in the holes for fasteners.
- Large capacity and stiffness can be achieved by glued-in rods and plates. However, the production must be carried out by skilled personnel. Despite many investigations performed in the past, there are, up to date, no available universal design guidelines. As a result, the connection technique is not very versatile, which maintains scepticism among many timber working professionals [42, 43].
- Probably, the most efficient joining technique in terms of capacity and stiffness can be achieved by the large glued connection. However, due to the complex and costly production on site, the technique is not suited to general use in timber bridges.
- The large withdrawal strength and stiffness, together with an easy application, make self-tapping screws efficient timber connectors. However, for large joints, a high number of screws is required. The joint detailing can thus be complicated, especially with regard to the transfer of compressive forces in the joint.

- The lagscrewbolts (LSBs) used in Japan present a more robust alternative to the self-tapping screws. The recent research has shown that the use of LSBs can facilitate relatively simple and cheap joints featuring large capacity and stiffness. In Europe, similar products known as long threaded rods (LTRs) are currently used for reinforcement of large glued laminated beams. Pilot studies in [69, 70] show that, similar to LSBs, LTRs can also be effectively employed as connectors in moment resisting joints.

  On the basis of the state-of-the art knowledge, LTRs are here selected as preferred connectors to provide splice joints with the required joint features.

3 Background for long threaded rods as connectors in timber joints

Long threaded rods (LTRs) have originally been developed as a reinforcement of large glued laminated timber beams to carry shear stresses and tensile stresses perpendicular to the grain. More details about the use of LTRs as a reinforcement can be found e.g. in [56, 71, 72]. However, in the present work, LTRs are utilised as connectors in moment resisting timber joints. The background for the use of LTRs in timber joints is summarised in the following.

3.1 Dimensions and materials

LTRs are manufactured by rolling high-strength wire rods, providing high tensile and torque capacity. There are two main industrial producers of LTRs: SFS Intec (WB System) [73] and SPAX [74], see Figure 3.1a and Figure 3.1b, respectively. The principal dimensions and mechanical properties of the SFS and SPAX rods are summarized in Table 3-1.

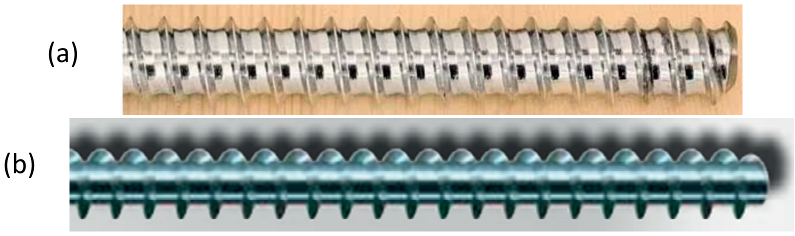

Figure 3.1 LTRs: (a) SFS Intec – WB System [75], (b) SPAX [76]

In addition to SFS and SPAX rods, a purpose-made LTR was developed in conjunction with the present work in order to facilitate a mechanical coupling of the rods. The geometry of the purpose-made LTR is shown in Figure 3.2. The average outer and inner diameters of the wood thread are 22.4 mm and 16.9 mm, respectively. The initial 90 mm long part of the rods was manufactured with an M20 metric threaded part. The transition from the wood thread to the metric thread is realised by a smooth evolution of the thread in order to minimise the stress peaks in the wood at the beginning of the wood thread. Moreover, the beginning of the wood thread is translated from the wood surface deeper in the wood which has a positive effect both on the capacity and the long-term behaviour. It was shown for STSs (with 8 mm diameter and 100 mm effective length) that by sinking the beginning of the wood thread from the wood surface (by 15 mm), an increase of the withdrawal capacity (by 15 %) can be achieved [53]. Furthermore, as shown in [77], sinking the beginning of the thread significantly improves the long-term behaviour of STSs placed parallel to the grain. For screws with the wood thread penetrating the timber edge surface, very poor long-term behaviour was observed. However, if the beginning of the wood thread was sunk 15 mm in the timber, the long-term behaviour improved drastically, reaching comparable resistance of screws inserted with 45° and 90° to the grain.

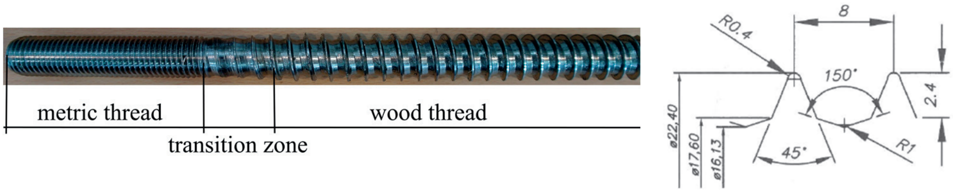

Figure 3.2 Purpose-made LTR with the geometry of the wood thread (dimensions in mm)

Table 3-1 Principal dimensions and tensile strength of LTRs

Type	Outer thread diameter [mm]	Inner thread diameter [mm]	Maximum length [mm]	Characteristic tensile capacity [kN]	Mean tensile capacity [kN]
SFS Intec	16	12	3000	91.5 [73]	N.A.
	20	15	3000	145 [73]	176 [78]
SPAX	16	12	3000	63 [74]	N.A.
Purpose-made [79]	22.4	16.9	1900	N.A.	207 [79]

The application of LTRs is very simple. After a drill, corresponding to the inner diameter of the rods, has been pre-drilled, the rod is simply driven into the hole using a high-torque drilling machine.

3.2 Withdrawal (axial) capacity and stiffness

3.2.1 *Technical approvals*

The withdrawal capacity of axially loaded LTRs embedded in timber with rod-to-grain angle $\gamma = 45° - 90°$ can be determined according to the manufacturers' technical approvals:

SFS Intec (WB system) [73]:

$$\begin{aligned} R_{ax,k} &= f_{ax,k} \cdot l_{ef} \cdot d \\ f_{ax,k} &= 0.52 \cdot d^{-0.5} \cdot l_{ef}^{-0.1} \cdot \rho_k^{0.8} \end{aligned} \tag{1}$$

(Note that the equation has changed from the previous version of the technical approval valid until November 2015.)

SPAX [74]:

$$\begin{aligned} R_{ax,k} &= f_{ax,k} \cdot l_{ef} \cdot d \cdot \left(\frac{\rho_k}{380} \right)^{0.8} \\ f_{ax,k} &= 10.2\ N/mm^2 \end{aligned} \tag{2}$$

where $R_{ax,k}$ is the characteristic withdrawal capacity of one rod in N, ρ_k is the characteristic value of the timber density in kg/m^3, d is the outer diameter of LTRs in mm and l_{ef} is the embedment (effective) length of rods screwed in timber in mm.

Note that both relations are independent of the rod-to-grain angle γ, but their validity is restricted to $\gamma = 45° - 90°$, and $4 \cdot d \le l_{ef} \le 1000\,\mathrm{mm}$.

None of the technical approvals provides means for the determination of the withdrawal stiffness.

3.2.2 *Eurocode 5*

The current version of Eurocode 5 (EC5) [10] provides the following relation for the determination of the withdrawal capacity of a single screw with $d > 12\ \mathrm{mm}$ and $\gamma \geq 30°$:

$$R_{ax,k} = \frac{f_{ax,k} \cdot d \cdot l_{ef}}{1.2 \cdot \cos^2 \gamma + \sin^2 \gamma} \cdot \left(\frac{\rho_k}{\rho_a} \right)^{0.8} \tag{3}$$

where $f_{ax,k}$ is the characteristic withdrawal parameter perpendicular to the grain determined in accordance with EN14592 for the associated density ρ_a. Since $f_{ax,k}$ is not provided by EC5, the relation is of little practical use.

EC5 does not cover the withdrawal stiffness.

3.2.3 *Recent research*

As stated earlier, neither the technical approvals, nor the EC5 provides design equations for the determination of the withdrawal capacity of LTRs for rod-to-grain angles of $\gamma < 45°$ and $\gamma < 30°$, respectively. Moreover, no relation is given for the determination of the withdrawal stiffness. Stamatopoulos et al. [78, 80] conducted series of experiments in order to determine the withdrawal capacity and the stiffness of LTRs as a function of the embedment length l_{ef} (l_{ef} $= 100$ - $600\ \mathrm{mm}$) and the rod-to-grain angle γ ($\gamma = 0° - 90°$) (tests carried out with SFS of type WB-T-20 [75]). Mean experimental results for specimens with the two largest tested embedment lengths of $l_{ef} = 450\ \mathrm{mm}$ and $l_{ef} = 600\ \mathrm{mm}$ are summarized in Figure 3.3.

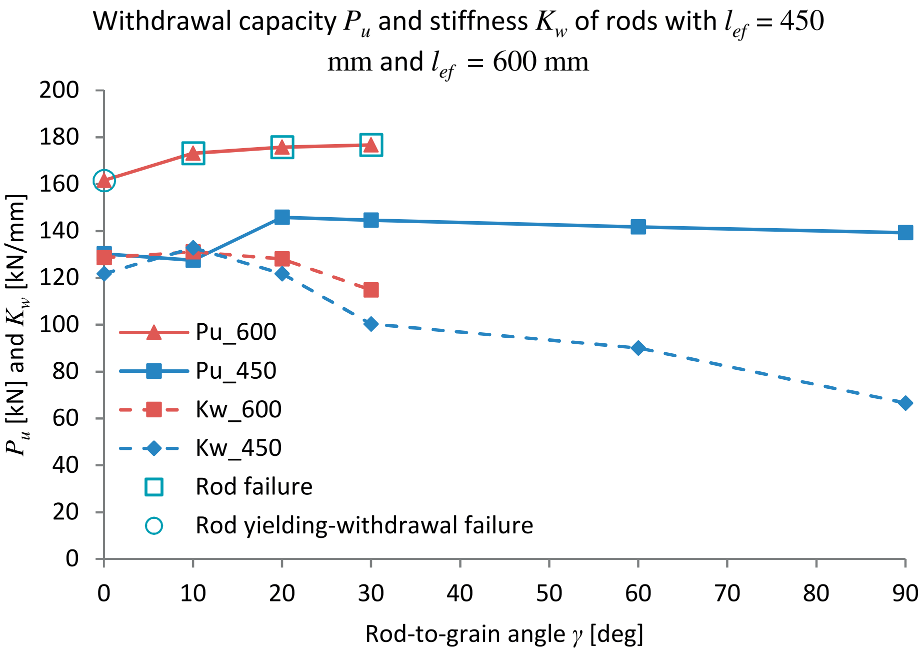

Figure 3.3 Mean experimental withdrawal properties of LTRs – SFS WB-T-20 [75] obtained from [78, 80]

The results presented in Figure 3.3 show the following trends:

- The capacity slightly increases for increasing rod-to-grain angle up to approximately 20˚, thereafter the capacity is approximately constant.
- The stiffness is decreasing for increasing rod-to-grain angle.
- For rods with 600 mm embedment lengths, the failure mode changes from a withdrawal failure to a tensile failure of the steel rods.

In addition, [78, 80] shows that:

- The capacity increases approximately linearly with the increasing embedment length.
- The relation between stiffness and embedment length is nonlinear – for embedment lengths larger than approximately 400 mm, the stiffness is approximately constant.
- The ductility of the failure increases with increasing rod-to-grain angle.

The analytical model proposed in [78, 80] is based on the classical Volkersen theory [81] and gives the following relations for predicting the withdrawal capacity P_u and the stiffness K_w:

$$\frac{P_{u,mean}}{\pi \cdot d \cdot l_{ef} \cdot f_w} = \left(\frac{\sin(m \cdot \omega \cdot \lambda_u)}{m \cdot \omega} + \frac{\tanh((1-\lambda_u) \cdot \omega) \cdot \cos(m \cdot \omega \cdot \lambda_u)}{\omega} \right) \tag{4}$$

$$K_w = \pi \cdot d \cdot l_{ef} \cdot \Gamma_e \cdot \frac{\tanh(\omega)}{\omega} \tag{5}$$

with input parameters defined as:

$$\begin{aligned} &\omega = \sqrt{\pi \cdot d \cdot \Gamma_e \cdot \beta \cdot l_{ef}^2}; \ \beta = \frac{1}{A_s \cdot E_s} + \frac{1}{A_w \cdot E_{w,\gamma}}; \\ &\Gamma_e = \frac{9.35}{1.5 \cdot \sin^{2.2}(\gamma) + \cos^{2.2}(\gamma)}; \\ &f_w = \frac{4.35}{0.91 \cdot \sin^2(\gamma) + \cos^2(\gamma)}; \ m = \frac{0.332}{1.73 \cdot \sin(\gamma) + \cos(\gamma)} \end{aligned} \tag{6}$$

where E_s is the elastic modulus of steel, A_s is the cross-sectional area of the threaded rod (with inner thread diameter), A_w is the area of wood subjected to axial stress, $E_{w,\gamma}$ is the elastic modulus of wood in an angle to the grain and the parameter λ_u is determined from a chart provided in [78], or conservatively taken equal to 1.0. The material parameters are optimized for glulam class GL30c of Norwegian spruce.

It should be noted that the investigations in [78, 80] were performed with a pull-push test arrangement. The area of wood, A_w, subjected to axial stress is dependent on the particular test set-up. However, for general use of rods in joints, the force transfer between the rod and the surrounding timber corresponds rather to a so-called pull-pull or pull-shear boundary condition. For the pull-pull boundary condition, Eqs. (4) and (5) take a different form. The resulting equations can be obtained e.g. from [82], but the solution is again a function of A_w, which is troublesome to define. A practical, but conservative, choice [83] is to assume the pull-shear boundary condition, for which the solution is obtained by Eq. (4) and (5) with $A_w = 0$ inserted to Eq. (6).

A group effect and effect of small edge distances and spacing of axially loaded LTRs was studied by Stamatopoulos et al. in [84]. The results of the investigation were compared with the design requirements given in EC5 for axially loaded screws. EC5 specifies that the capacity of a connection with multiple axially loaded screws should be determined using the effective number of screws $n_{ef} = n^{0.9}$, where n is the number of screws acting together in a connection. No guidance is given in EC5 considering the stiffness of a group of screws. In addition, requirements for minimum spacing and edge distances are given in EC5 in order to prevent the brittle splitting failures. The investigation in [84] was carried out with two LTRs in parallel in two configurations featuring: 1) reduced spacing ($a_2 = 2d$, whereas $a_2 = 5d$ in EC5), and 2) reduced edge distances ($a_{2.CG} = 1.5d$, whereas $a_{2.CG} = 4d$ in EC5). For both configurations, the effective number of LTRs regarding capacity was found to be in a range of 1.72 - 1.94, which corresponds essentially to $n_{ef} = n^{0.9}$ (1.87) given by EC5, but with EC5 assuming much larger spacing and edge distances. With regard to stiffness, no group effect was observed, which suggests that $n_{ef} = n$. It was concluded that the use of EC5 for a group effect of LTRs is conservative.

To the author's knowledge, the work of Stamatopoulos et al. provides the most comprehensive basis considering the withdrawal properties of LTRs. In addition, experimental investigation of Blaß et al. [71] can be mentioned: As a part of the investigation on the performance of LTRs as a shear reinforcement, withdrawal tests of LTRs were carried out with d = 16 and 20 mm, l_{ef} = 200 and 400 mm and γ = 45° and 90°. Furthermore, as discussed in Sections 2.7 and 2.8, lagscrewbolts (LSBs) feature similar geometry as LTRs. Some investigations on withdrawal properties of LSBs can be found e.g. in [67, 85, 86]. A comprehensive review of the different design models developed for LSBs and STSs can be found in [82].

3.3 Combined axial and lateral loading

No design models are currently available for the combined axial and lateral loading of the threaded rods. Several studies were conducted for timber-to-timber joints with inclined self-tapping screws, see e.g. [58, 59, 87]. In addition, few design guidelines are given by EC5. The suitability of the different models for LTRs used in joints is, however, unclear. Therefore, the effects of rod-to-grain and load-to-rod angles on capacity and stiffness were investigated within the scope of the present work, see Section 4.5.2.

3.4 Prototype joints with LTRs

A prototype steel-to-timber connection of a glulam cantilever beam with LTRs as connectors was investigated in [69, 70]. The cantilever beam is a scaled model of propeller blades in a water turbine, and it was experimentally investigated with the test set-up illustrated in Figure 3.4.

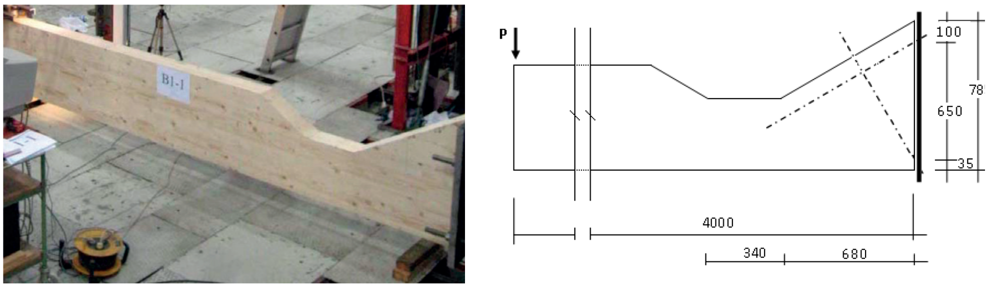

Figure 3.4 The test set-up for a cantilever beam connected by LTRs, [70]

SPAX threaded rods with 16 mm in diameter were installed into pre-drilled holes via a base steel plate. One or two rods were used at the tension side in different test configurations. The embedment length and rod-to-grain angle were 1000 mm and 30˚, respectively. Compression was transmitted by a contact pressure at the end face of the beam. In the first test, a crack occurred at the compression side caused by tensile stresses normal grain. Therefore, an additional rod with a rod-to-grain angle of 60˚ was used to reinforce the compression zone. This reinforcement prevented the cracking in further tests. Rupture failure in the steel rods was encountered in the tests with one tension rod. However, for the case with two rods, both the capacity and the rotational stiffness decreased disproportionally indicating a possible group effect of the rods. In addition, effects of moisture content (MC) on the stiffness and capacity were studied. The MC varied from 12 % to 24 %. The results showed that the increased MC had no effect on the capacity of the connection. The rotational stiffness slightly decreased with the increased MC, which can be explained by the lower elastic modulus of timber in green conditions. It was finally concluded that the use of LTRs as connectors can facilitate practical moment resisting connections, but more research is needed.

Several experimental investigations of prototype moment resisting joints with LTRs as connectors have recently been carried out in conjunction with master student projects at Norwegian University of Science and Technology and Norwegian University of Life Sciences [88-94]. Most of the work is reviewed and summarised in [91] (in English), and it will thus not be further discussed herein. As a representative example, a moment resisting column-beam connection investigated in [94] is shown in Figure 3.5.

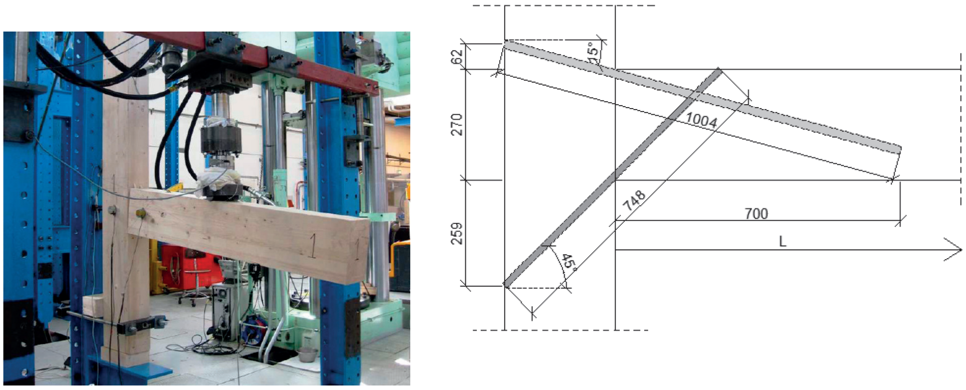

Figure 3.5 A prototype column-beam connection with LTRs, [94]

4 Overview of the present work

4.1 The proposed splicing technique

4.1.1 *The design concept*

The joint design is proposed in two alternatives, see the illustrations in Figure 4.1a and Figure 4.1b. In the first alternative, commonly available LTRs are embedded in timber parallel to the grain. The mutual splicing of the rods is carried out by grout-filled steel couplers. In the second alternative, purpose-made threaded rods with metric threads at one end are used with a small inclination to the grain. The rods are here joined by mechanical coupling.

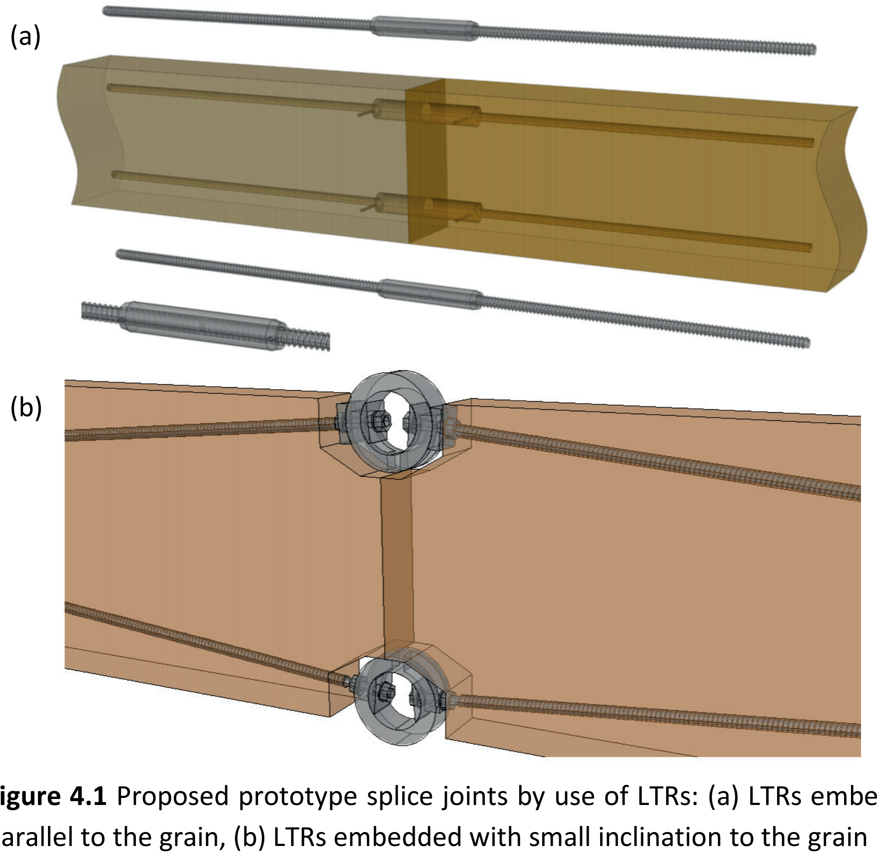

Figure 4.1 Proposed prototype splice joints by use of LTRs: (a) LTRs embedded parallel to the grain, (b) LTRs embedded with small inclination to the grain

The structural joint performance is based on the following principles:

- The moment resistance and the rotational stiffness are achieved by axial tension or compression in LTRs and by timber end faces in compression
- The compression force is transferred by the contact of timber end faces together with axial forces in LTRs
- The shear forces are carried by a shear key (the shear key is not shown in Figure 4.1 – a possible solution is illustrated in Figure 2.2)

The design philosophy of the joints is based on utilising the high withdrawal stiffness of the threaded rods to achieve a rotationally stiff joint without initial slip. By providing a sufficient effective length, the failure mode is driven by yielding of the steel rods. This enables a more reliable prediction of the structural properties and an increased ductility of the joint. The joint assembly is simple and fast since no special tools or skills of personnel are required. After the rod has simply been driven into the pre-drilled hole, it can immediately carry 100 % of the loads. The rods can be driven into timber elements prior to their transport, which enhances the efficiency of the joint assembly on site.

Conceptually, the joints with LTRs are similar to the joints with glued-in rods (discussed in Section 2.2). However, the main advantage of the use of LTRs is the easy manufacture. The joints with glued-in rods must be manufactured by skilled personnel in a climate-controlled environment. Furthermore, strength and stiffness of the joints with glued-in rods depend on the efficiency of the gluing operation, which is difficult to assess. On the contrary, the necessary embedment length in order to achieve tensile failure in the rods is in general smaller for glued-in rods, compared to LTRs (i.e. shorter rods can be used). The glued-in rods can also be provided with an additional detailing at the rod-ends prior to gluing, making the assembly of the joints somewhat easier as illustrated in Figure 2.4 and Figure 2.5.

4.1.2 *Joint alternatives*

The main difference between the two proposed joint alternatives is the orientation of the rods with respect to the grain, which is associated with various pros and cons. A simplified summary of the effects of the rod inclination on the joint performance is given in Table 4-1.

Table 4-1 Effects of the rod inclination on the joint performance

	Parallel to the grain	Inclined to the grain
Loading of rods	☺ Pure axial	☹ Axial and transversal
Withdrawal stiffness	☺ Higher	☹ Lower
Withdrawal capacity	☹ Lower	☺ Higher
Withdrawal ductility	☹ Lower	☺ Higher
Joint of LTRs	☺ Easier	☹ More complicated
Shrinkage cracks along rods	☹ Possible	☺ Prevented

Note: The withdrawal properties of LTRs are discussed in Section 3.2.3

The clear advantage of the *parallel-to-grain orientation of LTRs* (see details in [95]) is the effective force transfer in the axial direction of the rods. In addition, the joint of the mating rods is relatively simple. In the proposed solution, LTRs are mutually joined by grouting (gluing) in the steel couplers (similar to systems used for reinforced pre-cast concrete). The grouted joint enables the use of commonly available LTRs. The grout-filled couplers are fully embedded in timber and thus protected. However, the final setting time is affected by the curing of the glue, and the gluing operation on site implies quality control issues. If a mechanical, rather than a glued joint of the rods is preferred, the purpose-made LTRs with threaded ends can be used. The mechanical splicing of the rods can be facilitated similarly to the mechanical couplers used for splicing of reinforcing bars in concrete (see e.g. solutions by BAR-US® - SimGrip™ [96] or Lenton® [97]). Note that the mechanical couplers cannot be fully embedded in timber.

The main motivation behind the *inclined orientation of LTRs* (see details in [79]) is preventing a potential failure due to the occurrence of shrinkage cracks in the vicinity of the rods. Since the rods cross several "layers" of wood, the potential shrinkage cracks parallel to the grain cannot develop along the rods. As discussed in Section 3.2.2, the design equations for axially loaded screws provided by EC5 are not valid for the screw-to-grain angle below 30˚. The argumentation for this validity limit is not given in EC5; however, one of the possible explanations is that the capacity of short screws can be significantly reduced if a shrinkage crack along grains occurs in the vicinity of the screw. For long screws and threaded rods, the probability of such significant cracks is low, and the EC5 restriction becomes questionable. Nevertheless, the inclined rods present undoubtedly a more robust design also with respect to the ductility of the joint failure. The drawback of the rod inclination is the induced transversal force component at the rod-ends, which reduces the stiffness and the capacity of the rods [98]. In addition, splicing of the mating inclined rods is more complex. It is evident that the rod inclination should be as small as possible, but sufficient to bridge the potential cracks. In the present work, a rod-to-grain inclination of 5˚ is used, based on an engineering judgement. The optimisation of the rod inclination is suggested for future research work.

The reduced stiffness due to the acting transversal force can effectively be minimised by a stiff connection of the rod-ends in the rod couplers, and additionally by preventing the transversal displacements of the couplers [98]. In the present work, this problem was addressed by anchoring the couplers to the timber and by using special fitted washers for the connection of the rods and the couplers (see details in [79]). It should be noted that the mechanical couplers used in the present work are *prototypes* allowing an easy and flexible use in experiments. The couplers were designed assuring that plastic deformations would not arise before reaching the capacity of the rods. For application in the structures, the plastic deformation of the couplers is, on the contrary, beneficial, since it increases the ductility and the energy dissipation of the joint. The deformations in the steel parts can conveniently be controlled by design. The focus of the current work was on the structural performance of the rods and the timber. Further developments of the splicing of the inclined rods should be carried out prior to the practical applications of the joint.

4.2 Scope of the research work – Publication list

Paper i **MOMENT RESISTING SPLICE OF TIMBER BEAMS USING LONG THREADED RODS AND GROUT-FILLED COUPLERS – EXPERIMENTAL RESULTS AND PREDICTIVE MODELS**
Martin Cepelka, Kjell Arne Malo
In: Construction and Building Materials (2017), https://doi.org/10.1016/j.conbuildmat.2017.08.089 [95]
Scope: ***Beam splicing by LTRs embedded parallel to the grain***
- Moment capacity and rotational stiffness of the splice joint
- Capacity and stiffness of the grouted joint of LTRs
- Development of analytical models for the prediction of moment capacity and rotational stiffness of the splice joint

Paper ii **EFFECT OF ROD-TO-GRAIN ANGLE ON CAPACITY AND STIFFNESS OF AXIALLY AND LATERALLY LOADED LONG THREADED RODS IN TIMBER JOINTS**
Martin Cepelka, Kjell Arne Malo, Haris Stamatopoulos
Under review in an international scientific journal (2017) [98]
Scope: ***Investigation of effects of the rod-to-grain and the load-to-rod angles on capacity and stiffness of LTRs***
- Development of analytical models for laterally and axially loaded LTRs

Paper iii **MOMENT RESISTING ON-SITE SPLICE OF LARGE GLULAM ELEMENTS BY USE OF MECHANICALLY COUPLED LONG THREADED RODS**
Martin Cepelka, Kjell Arne Malo
Under review in an international scientific journal (2017) [79]
Scope: ***Beam splicing by LTRs embedded with an inclination to the grain***
- Mechanical coupling of the purpose-made LTRs with metric threaded ends
- Moment capacity and rotational stiffness of the splice joint
- Modification of the analytical models developed in *Paper i* to account for the transversal loading of rods
- Investigation of a combined action of bending moment and normal force

Paper iv **EXPERIMENTAL STUDY OF END GRAIN EFFECTS IN TIMBER JOINTS UNDER UNIAXIAL COMPRESSION LOAD**
Martin Cepelka, Kjell Arne Malo

In: Proceedings of the World Conference on Timber Engineering (WCTE 2016), Vienna, Austria (2016) [99]
Scope: ***Investigation of capacity and stiffness at an interface zone of two mutually compressed timber end faces***
- Effects of a direct timber-to-timber contact compared to a timber-steel-timber configuration

Paper v **EFFECT OF ON-SITE SPLICE JOINTS FOR TIMBER NETWORK ARCH BRIDGES**
Martin Cepelka, Kjell Arne Malo
In: Proceedings of the International Conference on Timber Bridges (ICTB 2017), Skellefteå, Sweden (2017) [100]
Scope: ***Stability of timber network arch bridges spliced by joints with LTRs***

Not appended **REVIEW ON ON-SITE SPLICE JOINTS IN TIMBER ENGINEERING**
Martin Cepelka, Kjell Arne Malo
In: Proceedings of the COST - Timber Bridges Conference 2014, Biel, Switzerland (2014) [101]
Scope: ***State-of-the-art review on on-site splice joints with possible application in timber bridges***

Not appended **SPLICING OF LARGE WOODEN MEMBERS**
Martin Cepelka; Kolbein Bell; Kjell Arne Malo
In: Durable Timber Bridges - Final Report and Guidelines (2017) [13]
Scope: ***Introduction to the topic of splicing of large wooden members***

4.3 Research methods

In the following, a brief summary with main features of the applied research methods related to the different investigations is given. For details, see the corresponding publications.

4.3.1 *Experimental*

The following short-term quasi-static experimental investigations were carried out in conjunction with the present research work:

1 **Beam splice test of the prototype joints with LTRs embedded parallel to the grain and mutually spliced by grout-filled couplers**
In: *Paper i [95]*
Features: Four-point bending configuration, 3 m long beams, 12 tests, LTRs SFS-WB-T-20, coupling of rods by grout-filled couplers, deformation

monitored by displacement transducers (LVDT) and digital image correlation (DIC) system ARAMIS [102]

2 Beam splice test of the prototype joints with LTRs inclined to the grain and mutually spliced by mechanical couplers

In: *Paper iii [79]*

Features: Four-point bending configuration, 8.5 m long beams, 4 tests, purpose-made LTRs, mechanical coupling of rods, deformation monitored by LVDTs and DIC [102]

3 Effect of combined axial and lateral loading on capacity and stiffness of LTRs

In: *Paper ii [98]*

Features: Pull-beam withdrawal configuration, 11 tests, LTRs SFS-WB-T-20, deformation monitored by LVDTs

4 Determination of capacity and stiffness at an interface of two mutually compressed timber end faces

In: *Paper iv [99] and Paper i [95]*

Features: Uniaxial compression parallel to the grain, 24 tests, deformation monitored by LVDTs

5 Tensile test of the rod splice by grout-filled couplers

In: *Paper i [95]*

Features: 6 tests, deformation monitored by LVDTs

6 Tensile test of the purpose-made LTRs

In: *Paper iii [79]*

Features: 3 tests

The timber specimens were made of glulam strength class GL30c [103] and conditioned at the standard environment of 20˚ C and 65 % relative humidity, resulting in approximately 12 % moisture content. The specimens in test 1, 3 and 4 were fabricated with 45 mm thick lamellas of Norwegian spruce, while the beams in test 2 were fabricated with 33 mm thick lamellas of Scots pine.

The threaded rods in tests 1, 3 and 5 were of type SFS WB-T-20 [75] complying with DIN 7998 [104]. In tests 2 and 6, the purpose-made LTRs were used, see Section 3.1.

Tests 1, 2 and 3 were carried out in collaboration with master students. Their respective master theses [92], [93] and [105] can provide additional materials to an interested reader (in the Norwegian language).

4.3.2 *Numerical*

Numerical 3D finite element analyses, corresponding to the experimental investigations 1-3 specified in Section 4.3.1, were carried out by the use of ABAQUS software [106]. The use of the numerical simulations enabled a deeper insight into the mechanical behaviour of the tested connections as well as the execution of parametric studies. In general, a good agreement between the results obtained by the finite element models and the experiments was achieved. The analyses corresponding to the investigations 1 and 3 were formulated as linear, and they were used to study the related stiffness properties. The model corresponding to the investigation 2 was in addition to stiffness predictions used also to predict the joint capacity by using nonlinear material properties and yield criterions (Hill's criterion for wood and von Mises's criterion for steel).

In *Paper v* [100], a case-study timber network arch bridge was analysed by using 2D and 3D numerical models. The 2D models (in-plane and out-of-plane) were analysed in RSAPRO [107], while the 3D model was analysed in ABAQUS [106]. The 2D models were mainly used to validate the complex 3D model. Static nonlinear analyses and linear (perturbation) buckling analyses were performed to investigate the effect of the splice rotational joint stiffness on the stability of the bridge selected for the case study.

4.3.3 *Analytical*

Analytical relations for practical design of the splice joint are proposed for determining the rotational stiffness, the moment capacity and the combined capacity for bending moment and normal force.

Tests of timber splice connections using glued-in hardwood dowels [38, 41] and glued-in rods [37, 39] demonstrated the importance of incorporating the slip of the connectors for predicting the height of the compression zone and the rotational stiffness. Moreover, it was observed in [37] that the stiffness of timber in compression is affected by the deformation at end grains of the timber end faces. The proposed analytical model derived in *Paper i* [95] accounts for both the slip of the connectors and for the deformation at the end grains.

No design models are currently available for the combined axial and lateral loading of LTRs. In *Paper ii* [98], analytical expressions for determining stiffness and capacity of axially and laterally loaded LTRs are proposed, intended as a basis for practical joint design.

The analytical models proposed in *Paper i* [95] were modified in *Paper iii* [79] to reflect the transversal force component at the rod-ends, imposed by the non-axial loading of the inclined rods. In addition, an interaction formula is proposed for the verification of the joint capacity under the combined actions of bending moment and normal force.

4.4 Limitations

Even though the following problems were kept in mind while developing the joining technique (see discussions in Sections 4.5.6 and 4.6), their thorough investigation was outside the scope of the present research work:

- Long-term behaviour
- Response to moisture induced stresses
- Effects of moisture content variation in timber
- Fatigue resistance
- Shear capacity

4.5 Main results and conclusions

4.5.1 *Paper i [95]*

The investigation revealed that high moment capacity and rotational stiffness of a timber splice connection can be achieved by the application of LTRs. The experimentally measured efficiency (see Appendix A) of the splice connection with regard to moment capacity and rotational stiffness was 69 % and 66 %, respectively. The tested connections showed no initial slip.

The effective (embedment) length of the LTRs (SFS WB-T-20 [75]) was 600 mm. A rather brittle failure, caused by the withdrawal of the threaded rods, was encountered for all experimental tests of the splice connection. It was concluded that both ductility and capacity of the connection can be enhanced by yielding in the rods, achieved by the use of a larger effective length of the rods.

The capacity and the withdrawal stiffness of the rod splice, by grout-filled couplers, were sufficient. None of the experimental tests failed at the joint of the rods. The grouting process was straightforward and easy to implement.

The proposed analytical models yielded slightly conservative estimates of both the rotational stiffness and the moment capacity of the splice connection.

4.5.2 *Paper ii [98]*

The investigation showed that both the capacity and the stiffness of LTRs are significantly reduced by the increased rod-to-grain and load-to-rod angles. The rod-to-grain angle of 45˚, leading to the load-to-rod angle of 45˚ in the current investigation, resulted in approximately 50 % reduction of the capacity and 70 % reduction of the stiffness compared to pure axial loading normal grain.

It was further shown that an increased stiffness of the rods can be obtained by restraining the rotation at the rod-ends. A significant increase of the stiffness can be achieved providing support at the rod-end transversally to the load direction (e.g. by anchoring the steel couplers to the timber member).

The analytical prediction of the capacity, by the use of the relations given in EC5 or the model proposed in [87] for connections with inclined screws, gave good agreement with the experimental results. The proposed analytical model for predicting the stiffness was well validated by the experimental results and the finite element simulations.

4.5.3 *Paper iii [79]*

The investigation showed that splicing of massive glulam sections can effectively be achieved by the use of LTRs with a small inclination to the grain. The experimentally investigated prototype joints featured large rotational stiffness, corresponding to 72 % efficiency. The ductile tensile rupture of the purpose-made LTRs was encountered for the effective rod length (l_{ef}) of 1200 mm, while specimens with the effective length of 1000 mm failed due to the withdrawal of the rods. The obtained efficiency in terms of capacity was not higher than 40 %, which was caused by: 1) insufficient stiffness of the connection of LTRs in the couplers for specimens with l_{ef} = 1200 mm, and 2) insufficient rod length for specimens with l_{ef} = 1000 mm. It was shown that the capacity efficiency could be increased by 10 % by anchoring the rod couplers and using LTRs with l_{ef} = 1200 mm.

The analytical and numerical models assumed no slip between the rods and the couplers, and the predicted moment capacity was, therefore, higher compared to the experimental results. A good mutual agreement was obtained for the moment capacity predicted by the analytical and the numerical models. The analytically predicted rotational stiffness corresponded well to the numerical and the experimental results. Based on the numerical investigations, it was furthermore concluded that the proposed simple analytical interaction model enables a reasonable prediction of the joint capacity under combined action of bending moment and normal force.

4.5.4 *Paper iv [99]*

The investigation showed that neither strength nor contact stiffness at the interface of two mutually compressed timber end faces was enhanced by the application of an intermediate contact steel plate. Furthermore, the tests with the intermediate contact steel plate were characterized by higher initial slip and less ductile post-elastic behaviour.

4.5.5 *Paper v [100]*

The investigation indicated that the splicing by LTRs can provide a sufficient rotational stiffness in order to maintain the stability of the timber network arch bridges. The results showed the in-plane stability of the arches was large compared to the out-of-plane stability, and even for very low values of the in-plane rotational joint stiffness, the critical load of the arch was governed by the out-of-plane buckling (note that no wind truss was used in between the arches). It was also shown that the splice joints had a negligible impact on the extreme values of the internal forces in the arches.

4.5.6 *Evaluation of the proposed joining technique performance*

Based on the performed investigations, the proposed joining technique showed to satisfy the requirements defined in Section 1.2 quite well. The particular fulfilment of the different requirements is summarised and evaluated in the following:

Sufficient strength

The bending capacity and the capacity under combined bending and normal force were investigated in *Paper i* [95] and *Paper iii* [79]. A preliminary assessment, based on the extreme values of the internal forces obtained for the case-study arch bridge analysed in *Paper v* [99], indicates that the proposed splicing technique provides sufficient strength to withstand the actions of the loading. As stated in Section 4.1.1, the transfer of shear forces is expected to be realised by shear keys. The design of the shear keys is not covered by the present work.

Sufficient stiffness without initial slip

The rotational stiffness was investigated in *Paper i* [95] and *Paper iii* [79]. The proposed solution features no initial slip, facilitating an immediate load take-up in the joint. The investigations performed in *Paper v* [99] indicates that the proposed splicing technique provides a sufficient rotational stiffness in order to maintain the stability of timber network arch bridges.

Ductility

The experimentally investigated prototype joints in *Paper i* [95] failed by rather brittle withdrawal failure of the rods. A considerably better ductility by tensile rupture of the rods was achieved for prototype joints in *Paper iii* [79] by inclining the rods and providing a sufficient embedment length. Additional ductility of the joint can be obtained by an appropriate design allowing plastic deformations of the rod couplers (so-called capacity design).

Detailing with respect to moisture induced stresses

The moisture induced cracks in joints are associated with restrained shrinkage and swelling in timber in the perpendicular-to-grain direction. The proposed splicing technique utilises LTRs embedded parallel or slightly inclined to the grain. The hygroscopic deformations in timber normal grain are thus not restrained, resulting in a favourable solution regarding the moisture induced stresses. However, in the experimental investigation in *Paper iii* [79], STSs were used to reinforce the joint and to anchor the couplers to the timber. As shown in [108-110], reinforcement in perpendicular-to-grain direction can initiate moisture induced cracks. In the present work, the amount of reinforcement was based on preliminary results from numerical models and on the visual observations during testing of the beam splices in *Paper i* [95]. It should be noted that the STSs were not optimised and further investigations should be carried out to eliminate the possible effect on the development of the moisture induced cracks.

Detailing with respect to fatigue

The fatigue resistance was not covered by the scope of the present work. Yet, the preliminary results of fatigue tests of axially loaded LTRs indicate that the fatigue resistance of timber is large compared to steel, and the fatigue capacity of joints with this type of connector is thus governed by the resistance of the steel components [13, 14]. The fatigue assessment of steel parts in joints is covered in detail by design codes, such as EN 1993-1-9 [15].

Fast, easy and reliable assembly

As discussed in 4.1.1, the application of LTRs is very fast and easy to carry out. The force transfer from timber to LTRs is realised through a mechanical contact providing an easily assessable solution in terms of quality control. Since the rods are driven to timber prior to transport, the on-site joint assembly can be very fast. The on-site assembly with the mechanical couplers is clearly superior to the grout-filled couplers. However, as discussed in Section 4.1.2, the mechanical couplers used in the investigation in *Paper iii* [79] were *prototypes* designed for the purpose of the experimental testing. Further developments of the couplers should be carried out prior to the practical applications of the joint.

Durability

It is discussed in the introductory section of this thesis that the main motivation behind the present research work is to enable the construction of timber bridges with massive glulam arches, which present a more durable alternative to the currently used truss arches due to the substantially lower number of connections. A durable solution of the joint itself depends on the proper detailing, as discussed in Section 1.2. The threaded rods can be galvanised, and since they are embedded in timber, a quite good durability is achieved. The rod couplers and additional steel detailing should be anti-corrosion treated. The joint as a whole should be covered by cladding both on the top and on the sides. An additional level of protection can be achieved by grout-filling the slots in timber, as shown in the example in Figure 2.6. Nevertheless, due to different shrinkage of the timber and the grouting material, the joint should always be additionally protected by cladding.

Epoxy mortar is often used to fill the space between the timber members in timber bridges due to its ease of application. However, cases with a serious degradation of the epoxy filling have been reported [111]. Computer-Numerical-Control (CNC) cutting machines allow nowadays a very precise manufacturing of the timber interface planes. The study in *Paper iv* [99] shows that splice joints with direct contact of timber end faces feature essentially the same axial capacity and stiffness as joints with a steel plate used in between the timber faces.

4.6 Proposals for future work

Prior to practical use of the proposed joining technique, further research should be carried out to investigate the aspects not covered by the scope of the present work. The following recommendations for future work are given:

Development of a practical mechanical coupling of the inclined rods

In the present work, prototype couplers were used for the purpose of the experimental investigation. Prior to potential applications of the joint, practical mechanical coupling of the rods should be developed. See further discussion in Section 4.1.2.

Optimisation of the rod-to-grain angle

As discussed in Section 4.1.2, a potential shrinkage crack in the vicinity of the threaded rod can limit the rod performance. Even though the probability of such a significant crack is low, the problem can be overcome by inclining the rods relative to the grain. However, since the inclined rods feature lower capacity and stiffness, the inclination should be as small as possible. Thus, further investigations can focus on optimising the rod-to-grain angle to ensure an optimal joint performance in terms of capacity and stiffness, but at the same time, preventing the shrinkage cracks from developing along the rods.

Shear capacity

The shear joint capacity should be investigated focusing on the two following aspects:

As discussed in Section 4.1.1, the transfer of the shear forces is expected to be realised by shear keys. However, the threaded rods feature a certain transversal capacity, especially in the inclined configuration, in which a part of the shear load is transferred in the strong axial direction of the rods.

In the case of a direct timber-to-timber contact of the end faces, the acting shear force may initiate tensile stresses perpendicular to the grain due to mutual interlocking of the end grains.

Effects of joint reinforcement in perpendicular-to-grain direction

Reinforcement normal grain by STSs was used in the experimental beam splice investigation in *Paper iii* [79]. As discussed in Section 4.5.6, the reinforcement was not optimised, and further investigations should be carried out in order to identify: 1) the necessary amount, and 2) the optimal configuration of the reinforcement considering the potential initiation of moisture induced cracks.

Effects of the load duration and the moisture content variation in wood on the performance of LTRs

To the author's knowledge, no research has been performed regarding the time-dependent behaviour of LTRs. Long-term withdrawal tests with STSs (with 8 mm diameter and 100 mm effective length) [77] showed that for the applied load levels lower than approximately 73 % of the ultimate strength, the behaviour of STSs was covered by the application of k_{mod} as currently present in EC5. For the actual connection, which is intended for the use in timber bridges, the permanent load levels are expected to be well below the threshold of 73 %. Furthermore, as discussed in Section 3.1, the long-term tests [77] showed that screws positioned parallel to the grain reached comparable long-term behaviour with screws inclined 45˚ and 90˚ to the grain if the beginning of the thread was embedded in timber. LTRs feature significantly larger effective lengths compared to STSs. It is thus expected that their behaviour is less vulnerable to the long-term effects. Nevertheless, the long-term performance of LTRs should be verified, especially for the end-grain applications with none or small inclination to the grain.

Withdrawal properties of LTRs in bending-related problems

As discussed in 3.2.3, the available analytical expressions for the determination of withdrawal capacity and stiffness of LTRs are based on the Volkersen theory [81]. The theory assumes a symmetrical stress distribution along the perimeter of the rod and the solution is further dependent on the mode of force transfer between the rods and the timber (pull-pull, pull-push, or pull-shear configurations). The use of expressions derived for pull-push or pull-pull configurations is in practice problematic due to the high dependence on the chosen timber area A_w, which has no physical basis in the bending-related problems. As shown in *Paper iii* [79], the use of the pull-shear boundary condition yields very conservative estimates of the withdrawal stiffness. The withdrawal stiffness monitored both in *Paper i* [95] and *Paper iii* [79] was also considerably larger when compared to the experimental results of Stamatopoulos et al. [80], which were obtained from the pull-push test configurations. A good agreement was obtained in the present work between the experimentally and the numerically obtained values for the withdrawal stiffness. This may indicate that the Volkersen theory is not fully adequate considering the bending-related problems with LTRs.

The observed withdrawal capacity of the rods was lower compared to the prediction by the analytical expressions and the experiments by Stamatopoulos et al. [78]. This discrepancy was justified by the actions of the transversal loading of the rods and it was taken into account by a reduction of the effective length of the rods in the analytical model.

In order to achieve a wider versatility of the analytical estimates of the rotational stiffness and the moment capacity, the analytical predictions of the withdrawal properties of LTRs in bending-related problems should be investigated more thoroughly. Besides numerical simulations, a pull-bending pull-out test set-up (see e.g. [27]) could be utilised for experimental investigations.

5 Declaration of authorship

Martin Cepelka wrote the first version of all the manuscripts. Opinions and changes from the co-authors were then added. The specific research tasks related to the different investigations are summarised in the following:

Paper i [95]

Martin Cepelka co-supervised the experimental investigation of the beam and the rod splices, conducted the experimental investigation of the timber interface in compression, evaluated all the experimental work, and performed and evaluated the numerical simulations. Both authors contributed to the derivation of the analytical models.

Paper ii [98]

Martin Cepelka evaluated the experimental work, and further-developed the numerical and analytical models based on the work of H. Grytting and E.D. Sæle in their master thesis [105].

Paper iii [79]

Martin Cepelka prepared and evaluated the experimental investigation, assisted with the experimental work, performed and evaluated the numerical simulations, and derived the analytical models.

Paper iv [99]

Martin Cepelka prepared, performed and evaluated the experimental work.

Paper v [100]

Martin Cepelka performed and evaluated the numerical simulations. The 3D numerical model was built in Abaqus by Anna Ostrycharczyk.

6 References

[1] K. Bell, E. Karlsrud, Large glulam arch bridges - a feasibility study, Proceedings of the World Conference on Timber Engineering (WCTE 2004), Lahti, Finland, 2004.

[2] P. Tveit, Considerations for Design of Network Arches, Journal of Structural Engineering 113 (1987) 2189-2207.

[3] J. Veie, M. Østgårdstrøen, Steibrua, Norwegian Public Roads Administration, Brukonferansen 2016 - available at https://www.vegvesen.no/_attachment/1606923/binary/1145671?fast_title=Steibrua.pdf, (last accessed 06/2017).

[4] J. Veie, Network arch bridge with glulam arches. Lessons learned and further development, International Conference on Timber Bridges (ICTB2017), Skellefteå, Sweden, 2017.

[5] K. Bell, Structural systems for glulam arch bridges, International Conference on Timber Bridges (ICTB 2010), Lillehammer, Norway, 2010.

[6] K.A. Malo, A. Ostrycharczyk, R. Barli, I. Hakvåg, On development of network arch bridges in timber, International Conference on Timber Bridges (ICTB 2013), Las Vegas, USA, 2013.

[7] K. Bell, L. Wollebæk, Large, mechanically joined glulam arches, Proceedings of the World Conference on Timber Engineering (WCTE 2004), Lahti, Finland, 2004.

[8] L. Wollebæk, K. Bell, Stability of glulam arches, Proceedings of the World Conference on Timber Engineering (WCTE 2004), Lahti, Finland, 2004.

[9] A.J.M. Leijten, Requirements for moment connections in statically indeterminate timber structures, Engineering Structures 33 (2011) 3027-3032.

[10] CEN, EN 1995-1-1:2004: Design of timber structures. Part 1-1: General-Common rules and rules for buildings, European committee for standarization, Brussels, 2004.

[11] S. Thelandersson, Wood as Construction Material, in: S. Thelandersson, H.J. Larsen (Eds.), Timber Engineering, Wiley, 2003.

[12] CEN, EN 1995-2: 2004: Design of timber structures. Part 2: Bridges

European committee for standarization, Brussels, 2004.

[13] K.A. Malo, A. Pousette, S. Thelandersson, S. Fortino, L. Salokangas, J. Wacker, Durable timber bridges Final report and guidelines, RISE Research Institutes of Sweden, 2017.

[14] H. Stamatopoulos, K.A. Malo, Fatigue strength of axially loaded threaded rods embedded in glulam at 45º to the grain, International Conference on Timber Bridges (ICTB2017), Skellefteå, Sweden, 2017.

[15] CEN, EN 1993-1-9:2005: Design of steel structures - Part 1-9: Fatigue, European Committee for Standardization, Brussels, 2005.

[16] T. Dyken, Trebruer - Statens Vegvesens rapport Nr.422 (Timber bridges - Norwegian Public Roads Administration report Number 422), Statens Vegvesen (Norwegian Public Roads Administration), 2017.

[17] M. Augustin, Ultimite Limit States – Joints, Educational Materials for Designing and Testing of Timber Structures – TEMTIS Handbook 1 – Timber Structures, Leonardo da Vinci Pilot Project CZ/06/B/F/PP/168007, 2008.

[18] J. Sjödin, C.-J. Johansson, Influence of initial moisture induced stresses in multiple steel-to-timber dowel joints, Holz als Roh- und Werkstoff 65 (2007) 71-77.

[19] H.J. Larsen, Fasteners, Joints and Composite Structures, in: S. Thelandersson, H.J. Larsen (Eds.), Timber Engineering, Wiley, 2003.

[20] D. Lathuillière, L. Bléron, T. Descamps, J.-F. Bocquet, Reinforcement of dowel type connections, Construction and Building Materials 97 (2015) 48-54.

[21] F. Lam, M. Schulte-Wrede, C.C. Yao, J.J. Gu, Moment resistance of bolted timber connections with perpendicular to grain reinforcements, Proceedings of the World Conference on Timber Engineering (WCTE 2008), Miyazaki, Japan, 2008.

[22] F. Lam, M. Gehloff, M. Closen, Moment-resisting bolted timber connections, Proceedings of the Institution of Civil Engineers - Structures and Buildings 163 (2010) 267-274.

[23] F. Brühl, U. Kuhlmann, Connection Ductility in Timber Structures Considering the Moment-rotation Behavior, Proceedings of the World Conference on Timber Engineering (WCTE 2012), July 16-19, 2012, Auckland, New Zeland, 2012.

[24] F. Brühl, J. Schänzlin, U. Kuhlmann, Ductility in Timber Structures: Investigations on Over-Strength Factors, in: S. Aicher, H.W. Reinhardt, H. Garrecht (Eds.), Materials and Joints in Timber Structures: Recent Developments of Technology, RILEM Bookseries 9, Springer Netherlands, Dordrecht, 2014, pp. 181-190.

[25] C. Bengtsson, C.-J. Johansson, GIROD – Glued-In Rods for Timber Structures - Final Report, 2002.

[26] G. Tlustochowicz, E. Serrano, R. Steiger, State-of-the-art review on timber connections with glued-in steel rods, Materials and Structures 44 (2011) 997-1020.

[27] C. O'Neill, D. McPolin, S.E. Taylor, A.M. Harte, C. O'Ceallaigh, K.S. Sikora, Timber moment connections using glued-in basalt FRP rods, Construction and Building Materials 145 (2017) 226-235.

[28] N. Gattesco, A. Gubana, M. Buttazi, Cyclic behaviour of glued-in joints under bending moments, Proceedings of the World Conference on Timber Engineering (WCTE 2010), June 20-24, Riva Del Garda, Trento, Italy, 2010.

[29] E. Gehri, High Performing Jointing Technique Using Glue-in Rods, Proceedings of the World Conference on Timber Engineering (WCTE 2010), June 20-24, Riva Del Garda, Trento, Italy, 2010.

[30] R. Steiger, E. Gehri, R. Widmann, Pull-out strength of axially loaded steel rods bonded in glulam parallel to the grain, Materials and Structures 40 (2007) 69-78.

[31] Y. Wakashima, K. Okura, K. Kyotani, Development of ductile semi-rigid joints with lagscrewbolts and glued-in rods, Proceedings of the World Conference on Timber Engineering (WCTE 2010), June 20-24, Riva Del Garda, Trento, Italy, 2010.

[32] G. Parida, H. Johnsson, M. Fragiacomo, Provisions for Ductile Behavior of Timber-to-Steel Connections with Multiple Glued-In Rods, Journal of Structural Engineering 139 (2013) 1468-1477.

[33] J. Kangas, Design of connections based on in V-form glued-in rods, Proceedings of the World Conference on Timber Engineering (WCTE 2000), July 31-August 3, Whistler Resort, British Columbia, Canada, 2000.

[34] J. Kangas, Capacity, fire resistance and gluing pattern of the rods in V-Connections, Paper 33-7-10 In: Proceedings of 33th conference of CIB-W18, Delft, The Netherlands, 2000.

[35] J. Kangas, A. Kevarinmäki, Quality control of connections based on in V-shape glued-in steel rods, Paper 34-7-4 In: Proceedings of 34th conference of CIB-W18, Venice, Italy, 2001.

[36] W. Minder, Swiss timber bridges, http://www.swiss-timber-bridges.ch/detail/171, (last accessed 06/2017).

[37] J.L. Jensen, P. Quenneville, Connections with glued-in rods subjected to combined bending and shear actions, CIB-W18/42-7-9 International council for research and innovation in building and construction working commission W18 - Timber structures, 2009.

[38] T. Sasaki, A. Koizumi, J.L. Jensen, Y. Iijima, Y. Tamura, K. Komatsu, End joint with glued-in hardwood dowels in timber construction I. Bending properties of beams jointed with single row of dowels, Mokuzai Gakkaishi/Journal of the Japan Wood Research Society 45 (1999) 17-24.

[39] B.H. Xu, A. Bouchaïr, P. Racher, Analytical study and finite element modelling of timber connections with glued-in rods in bending, Construction and Building Materials 34 (2012) 337-345.

[40] J. Ogrizovic, F. Wanninger, A. Frangi, Experimental and analytical analysis of moment-resisting connections with glued-in rods, Engineering Structures 145 (2017) 322-332.

[41] K. Komatsu, A. Koizumi, T. Sasaki, J.L. Jensen, Y. Iijima, Flexural behavior of GLT beams end-jointed by glued-in hardwood dowels, CIB-W18 Timber Structures, 30-7-1, 1997.

[42] M. Stepinac, F. Hunger, R. Tomasi, E. Serrano, V. Rajcic, J.W.G. Van de Kuilen, Comparison of design rules for glued-in rods and design rule proposal for implementation in European standards, Proceedings of CIB-W18 Timber Structures, Meeting 46, Vancouver (Canada) 26-29 August, 2013, Timber Scientific Publishing, Vancouver, Canada, 2013.

[43] R. Steiger, E. Serrano, M. Stepinac, V. Rajčić, C. O'Neill, D. McPolin, R. Widmann, Strengthening of timber structures with glued-in rods, Construction and Building Materials 97 (2015) 90-105.

[44] T. Vallée, T. Tannert, S. Hehl, Experimental and numerical investigations on full-scale adhesively bonded timber trusses, Materials and Structures 44 (2011) 1745.

[45] K.-U. Schober, T. Tannert, Hybrid connections for timber structures, European Journal of Wood and Wood Products 74 (2016) 369-377.

[46] L. Bathon, O. Bletz-Mühldorfer, J. Schmidt, F. Diehl, Fatigue design of adhesive connections using perforated steel plates, Proceedings of the World Conference on Timber Engineering (WCTE 2014), August 10-14, Quebec City, Canada, 2014.

[47] L. Bathon, O. Bletz-Mühldorfer, J. Schmidt, F. Diehl, Fatigue Performance of Adhesive Connections for Wooden Wind Towers, in: S. Aicher, H.W. Reinhardt, H. Garrecht (Eds.), Materials and Joints in Timber Structures: Recent Developments of Technology, RILEM Bookseries 9, Springer Netherlands, Dordrecht, 2014.

[48] K.-U. Schober, W. Becker, J. Weber, Grouted joints in timber engineering, in: W.W. J. Eberhardsteiner, A. Fadai, M. Pöll (Ed.) Proceedings of the World Conference on Timber Engineering (WCTE 2016), August 22-25, 2016, Vienna University of Technology, Austria, ISBN: 978-3-903039-00-1, Vienna, Austria, 2016.

[49] S. Aicher, Geklebte Vollstöße großformatiger Brettschichtholzträger (Glued full butt joints for large-format glulam beams), 17. Internationales Holzbau-Forum 11, Garmisch-Partenkirchen, 2011.

[50] S. Aicher, J. Hezel, G. Stapf, Mechanical and glued joints in glulam of ultra high efficiency, Proceedings of the World Conference on Timber Engineering (WCTE 2012), July 16-19, 2012, Auckland, New Zeland, 2012.

[51] Hess Limitless - Reference project - Tennis and Bowling centre, Petange, Louxembourg, http://www.hess-timber.com/en/projects/timber-architecture/detail/tennis-and-bowling-centre/, (last accessed 05/2017).

[52] www.bertsche-office.de/us, (last accessed 08/2014)

[53] G. Pirnbacher, G. Schickhofer, Load bearing- and optimization potential of self-tapping wood screws, Proceedings of the World Conference on Timber Engineering (WCTE 2010), June 20-24, Riva Del Garda, Trento, Italy, 2010.

[54] H.J. Blaß, Joints with Dowel-type fasteners, in: S. Thelandersson, H.J. Larsen (Eds.), Timber Engineering, Wiley, 2003.

[55] H.J. Blaß , I. Bejtka, Screws with Continous Threads in Timber Connections, in: S.Aicher, H.-W.Reinhardt (Eds.), PRO 22: Proceedings of the International RILEM Symposium on Joints in Timber Structures, Stuttgard, Germany, 2001, pp. 193-201.

[56] P. Dietsch, R. Brandner, Self-tapping screws and threaded rods as reinforcement for structural timber elements – A state-of-the-art report, Construction and Building Materials 97 (2015) 78-89.

[57] S. Intec, SFS WR - Mehr Power im konstruktiven Holzbau mit dem effizienten Befestigungssystem WR für leistungsstarke Verbindungen und Verstärkungen, https://sfs.biz/sfs_download/media/de/general_media/downloadcenter/sfs_unimarket_1/befestigungstechnik/konstruktiver_holzbau/broschuere_wr___wt___wb_.pdf, (last accessed 06/2017).

[58] R. Tomasi, A. Crosatti, M. Piazza, Theoretical and experimental analysis of timber-to-timber joints connected with inclined screws, Construction and Building Materials 24 (2010) 1560-1571.

[59] I. Bejtka, H.J. Blaß, Joints with inclined screws, CIB W18-Meeting 35, Kyoto, Japan, 2002, pp. Paper 7-5.

[60] H. Krenn, G. Schickhofer, Joints with inclined Screws and Steel Plates as outer Members, Proceedings of the 42nd CIB-W18 meeting, Dübendorf, Switzerland, 2009.

[61] E. Mondou, CESM Soccer Center in Montreal, 20. Internationales Holzbau-Forum 2014, Garmisch-Partenkirchen, 2014.

[62] Saint-Michel Environmental Complex Soccer Stadium, Nordic Structures, http://nordic.ca/en/projects/structures/smec-soccer-stadium, (last accessed 06/2017).

[63] SWG, Innovative application for ASSY plus VG, http://www.swg-produktion.de/fileadmin/Bilder/Produkte/ZD-Platte/ZD-Platte_rigid_frame.pdf, (last accessed 06/2017).

[64] M. Closen, F. Lam, Performance of Moment Resisting Self-tapping Screw Assembly Under Reverse Cyclic Load, Proceedings of the World Conference on Timber Engineering (WCTE 2012), July 16-19, 2012, Auckland, New Zeland, 2012.

[65] R. Gohlich, J. Erochko, Development of a heavy timber moment-resisting frame with ductile steel links, Proceedings of the World Conference on Timber Engineering (WCTE 2016), August 22-25, 2016, Vienna University of Technology, Austria, ISBN: 978-3-903039-00-1, Vienna, Austria, 2016.

[66] T. Mori, M. Nakatani, S. Tesfamariam, Performance of semirigid timber frame with Lagscrewbolt connections: experimental, analytical, and numerical model

results, International Journal of Advanced Structural Engineering (IJASE) 7 (2015) 387-403.

[67] M. Nakatani, K. Komatsu, Development and verification of theory on pull-out properties of lagscrewbolted timber joints, Proceedings of the World Conference on Timber Engineering (WCTE 2004), Lahti, Finland, 2004.

[68] M. Nakatani, T. Mori, K. komatsu, Development of moment-resisting joint system using lagscrewbolts, Proceedings of the World Conference on Timber Engineering (WCTE 2006), August 6-10, Portland, Oregon, USA, 2006.

[69] P. Ellingsbø, K.A. Malo, Cantilever Glulam Beam Fastened with Long Threaded Steel Rods, Proceedings of the World Conference on Timber Engineering (WCTE 2010), June 20-24, Riva Del Garda, Trento, Italy, 2010.

[70] K.A. Malo, P. Ellingsbø, On Connections for Timber Bridges, International Conference on Timber Bridges (ICTB 2010), Lillehammer, Norway, 2010.

[71] H.J. Blaß, O. Krüger, Schubverstärkung von Holz mit Holzschrauben und Gewindestangen (Shear reinforcement of wood with wood screws and threaded rods), Universität Karlsruhe, Karlsruhe: KIT Scientific Publishing, 2010.

[72] R. Jockwer, R. Steiger, Performance of self-tapping screws and threaded steel rods in shear reinforcement of glulam beams, in: W.W. J. Eberhardsteiner, A. Fadai, M. Pöll (Ed.) Proceedings of the World Conference on Timber Engineering (WCTE 2016), August 22-25, 2016, Vienna University of Technology, Austria, ISBN: 978-3-903039-00-1, Vienna, Austria, 2016.

[73] DiBt, Allgemeine bauaufsichtliche Zulassung - Z-9.1-777 - Gewindestangen mit Holzgewinde als Holzverbindungsmittel (General building approval - Z-9.1-777 - Threaded rods with wood threads as wood connectors), Deutches Institut für Bautechnik, Berlin, 2015.

[74] DiBt, Allgemeine bauaufsichtliche Zulassung - Z-9.1-832 - SPAX Gewindestangen als Holzverbindungsmittel (General building approval - Z-9.1-832 - SPAX Threaded rods as wood connectors), Deutches Institut für Bautechnik, Berlin, 2016.

[75] SFS-Intec, https://www.sfsintec.ca/mo/us/en/web/construction/timber_work/system_wb/wb_system.html, (last accessed 06/2017).

[76] SPAX, https://www.spax.com/en/craftsmen/screw-finder/products/specials/spax-for-timber-construction/spax-threaded-rod-with-hex-head, (last accessed 06/2017).

[77] G. Pirnbacher, G. Schickhofer, Zeitabhängige Entwicklung der Traglast und des Kriechverhaltens von axial beanspruchten, selbstbohrenden Holzschrauben, Research report, holz.bau forschungs gmbh, 2012.

[78] H. Stamatopoulos, K.A. Malo, Withdrawal capacity of threaded rods embedded in timber elements, Construction and Building Materials 94 (2015) 387-397.

[79] M. Cepelka, K.A. Malo, Moment resisting on-site splice of large glulam elements by use of mechanically coupled long threaded rods, Submitted for publication in an international scientific journal (Submitted 06/2017).

[80] H. Stamatopoulos, K.A. Malo, Withdrawal stiffness of threaded rods embedded in timber elements, Construction and Building Materials 116 (2016) 263-272.

[81] O. Volkersen, Die nietkraftverteilung in zugbeanspruchten nietverbindungen mit konstanten laschenquerschnitten (The rivet-force distribution in tension-stressed rivet joints with constant adherends thickness), Luftfahrtforschung 15 (1938).

[82] H. Stamatopoulos, Withdrawal properties of threaded rods embedded in glued-laminated timber elements. Dissertation, vol Doctoral thesis, NTNU, Norwegian University of Science and Technology, Trondheim, 2016.

[83] J.L. Jensen, A. Koizumi, T. Sasaki, Y. Tamura, Y. Iijima, Axially loaded glued-in hardwood dowels, Wood Science and Technology 35 (2001) 73-83.

[84] H. Stamatopoulos, K.A. Malo, Withdrawal of pairs of threaded rods with small edge distances and spacings, European Journal of Wood and Wood Products (2017) 1-12.

[85] J.L. Jensen, M. Nakatani, P. Quenneville, B. Walford, A simple unified model for withdrawal of lag screws and glued-in rods, European Journal of Wood and Wood Products 69 (2011) 537-544.

[86] J.L. Jensen, M. Nakatani, P. Quenneville, B. Walford, A simplified model for withdrawal of screws from end-grain of timber, Construction and Building Materials 29 (2012) 557-563.

[87] R. Jockwer, R. Steiger, A. Frangi, Fully Threaded Self-tapping Screws Subjected to Combined Axial and Lateral Loading with Different Load to Grain Angles, in: S. Aicher, H.W. Reinhardt, H. Garrecht (Eds.), Materials and Joints in Timber Structures: Recent Developments of Technology, RILEM Bookseries 9, vol 9, Springer Netherlands, Dordrecht, 2014, pp. 265-272.

[88] P.K. Buene, Design of mountable moment stiff joint with long screws in tension, vol Master thesis, Norwegian university of science and technology, 2009.

[89] A.F. Drageset, T.H. Hoff, Numerical Analyses of Moment Resisting Beam-to-Column Connections in Timber Structures, vol Master thesis, Norwegian university of science and technology, NTNU, 2017.

[90] H. Larsen, Momentbærende forbindelser i limtrebjelker (Rigid connections in glulam beams), vol Master thesis, Norwegian university of science and technology, NTNU, 2012.

[91] K.I. Nordal, K.S. Lied, A conceptual study of glulam connections using threaded rods and connecting circular steel profiles, vol Master thesis, Norwegian university of science and technology, NTNU, 2016.

[92] M. Strøm, C.A. Moe, Skjøting av lange aksialbærende skruer for momentstive forbindelser i trekonstruksjoner (Splicing of long threaded rods for moment resisting connections in timber structures), vol Master thesis, Norwegian university of science and technology, NTNU, 2015.

[93] H.O. Veium, Aksialbelastede gjengestenger i limtreforbindelse (Axially Loaded Threaded Rods in Glulam Connection), vol Master thesis, Norwegian university of science and technology, NTNU, 2016.

[94] N. Westerheim, Konseptstudie av knutepunkt i limtre og lange aksialbærende treskruer utsatt for brannbelastning (Conceptual study of connections using glulam and long threaded bars exposed to fire loading), vol Master thesis, Norwegian university of science and technology, NTNU, 2013.

[95] M. Cepelka, K.A. Malo, Moment resisting splice of timber beams using long threaded rods and grout-filled couplers – Experimental results and predictive models, Construction and Building Materials 155 (2017) 560-570.

[96] BAR-US, Mechanical Rebar Splice Solutions, http://www.bar-us.com/en/brochures/Bar-us-SimGrip-System-Brochure-2012.pdf, (last accessed 07/2017).

[97] ERICO, Lenton reinforcing bar splicing, http://www.bag-mannheim.de/pdf/LENTON_COUPLER_INSTRUCTION_MANUAL_2004.pdf, (last accessed 07/2017).

[98] M. Cepelka, K.A. Malo, H. Stamatopoulos, Effect of rod-to-grain angle on capacity and stiffness of axially and laterally loaded long threaded rods in timber joints, Submitted for publication in an international scientific journal (Submitted 05/2017).

[99] M. Cepelka, K.A. Malo, Experimental study of end grain effects in timber joints under uniaxial compression load, in: W.W. J. Eberhardsteiner, A. Fadai, M. Pöll (Ed.) Proceedings of the World Conference on Timber Engineering (WCTE 2016), August 22-25, 2016, Vienna University of Technology, Austria, ISBN: 978-3-903039-00-1, Vienna, Austria, 2016.

[100] M. Cepelka, K.A. Malo, Effect of on-site splice joints for timber network arch bridges, International Conference on Timber Bridges (ICTB 2017) Skellefteå, 2017.

[101] M. Cepelka, K.A. Malo, Review on on-site splice joints in timber engineering, COST-Timber Bridges Conference 2014, Biel/Bienne, 2014.

[102] GOM Optical Measuring Techniques, ARAMIS, User Manual-Software, 2009.

[103] CEN, EN 14080:2013: Timber structures-Glued laminated timber and glued solid timber - Requirements, European Committee for Standardization, 2013.

[104] DIN, DIN 7998: Gewinde und Schraubenenden für Holzschrauben (Threads and screws for wood), Deutsches Institut für Normung, Berlin, 1975.

[105] H. Grytting, E.D. Sæle, Aksial- og tverrbelastede gjengestenger i trekonstruksjoner (Axial and Lateral Loaded Threaded Rods in Timber Structures), vol Master thesis, Norwegian university of science and technology, NTNU, 2015.

[106] D.S.S.C. DSS, Abaqus analysis user's guide, Version 6.14, 2014.

[107] Autodesk, Autodesk Robot Structural Analysis Proffesional (RSAPRO), 2017.

[108] V. Angst, K.A. Malo, Effect of self-tapping screws on moisture induced stresses in glulam, Engineering Structures 45 (2012) 299-306.

[109] P. Dietsch, Effect of reinforcement on shrinkage stresses in timber members, Construction and Building Materials 150 (2017) 903-915.

[110] P. Dietsch, H. Kreuzinger, S. Winter, Effects of changes in moisture content in reinforced glulam beams, Proceedings of the World Conference on Timber Engineering (WCTE 2014), August 10-14, Quebec City, Canada, 2014.

[111] H. Burkart, Learning Experiences from Timber Bridge Inspections, NPRA reports, Statens Vegvessen (Norwegian Public Roads Administration), 2016.

Part II:

Appended Papers

Paper i

Moment resisting splice of timber beams using long threaded rods and grout-filled couplers – Experimental results and predictive models

Martin Cepelka, Kjell Arne Malo

In: Construction and Building Materials (2017)

https://doi.org/10.1016/j.conbuildmat.2017.08.089

Construction and Building Materials 155 (2017) 560–570

Contents lists available at ScienceDirect

Construction and Building Materials

journal homepage: www.elsevier.com/locate/conbuildmat

Moment resisting splice of timber beams using long threaded rods and grout-filled couplers – Experimental results and predictive models

Martin Cepelka [*], Kjell Arne Malo

Department of Structural Engineering, Norwegian University of Science and Technology (NTNU), Rich. Birkelandsvei 1A, 7491 Trondheim, Norway

HIGHLIGHTS

- A novel rotationally stiff on-site splice timber joint is presented.
- Long threaded rods are used as main fasteners in moment resisting joint.
- Predictive models for the rotational stiffness and the strength are proposed.
- Experimental and numerical methods were used.

ARTICLE INFO

Article history:
Received 12 February 2017
Received in revised form 29 July 2017
Accepted 16 August 2017
Available online 23 September 2017

Keywords:
Timber beam splice connection
Long threaded rods
Grout-filled couplers
Experimental testing
3D finite element model
Rotational stiffness
Moment capacity

ABSTRACT

In order to achieve larger spans of timber arch bridges, glulam massive timber sections must be spliced on-site by moment resisting and rotationally stiff joints. In this paper, a novel timber splice connection utilizing long threaded rods and grout-filled couplers is presented. Flexural characteristics of the splice joint were investigated by full-scale experimental tests and 3D finite element models. An analytical model is proposed for determining the moment capacity and the rotational stiffness of the splice connection. The experimentally measured efficiency of the splice connection with regard to moment capacity and rotational stiffness was 69% and 66%, respectively.

1. Introduction

The development of glued laminated timber (glulam) allows for production of timber elements with nearly unlimited cross-sectional dimensions. However, production and transportation impose limitations on the length of timber elements. The maximum length of glulam elements is in a range of 30–40 m for straight elements, and approximately 20–30 m for curved elements in dependence on the radius of curvature and means of impregnation [1,2]. In order to obtain larger spans, it is necessary to splice the timber elements on site. Feasibility studies of glulam arches with network hanger configuration have shown that it is possible to achieve timber bridges with spans in a range of 100–120 m [3,4]. In order to maintain stability and reduce buckling problems of the timber arches, it is crucial to incorporate flexural rigidity in splice connections.

The pros and cons of different splice connection techniques in timber engineering are discussed in [5]. Recent research on self-tapping screws and long threaded rods has demonstrated the capability of these axially loaded fasteners to achieve effective connections by utilizing their high axial withdrawal capacity and stiffness. Currently, self-tapping screws and long threaded rods are mostly used as reinforcement of timber beams [6] or as connectors in a shear or axially loaded lap connections [7]. However, the performance of long threaded rods in moment resisting connections remains to be revealed. The present investigation deals with the application of long threaded rods as the main fasteners in timber splice connections subjected to bending moments. Grout-filled steel couplers (similar to systems used for reinforced pre-cast concrete) are used to connect the long threaded rods inserted in the two parts of the timber beam. The main objective of the investigation is to determine the flexural characteristics of the splice connection. Prototype splice connections were produced and investigated by full-scale experimental tests. Complementary experimental investigations were carried out to 1) identify

---

[*] Corresponding author.

E-mail addresses: martin.cepelka@ntnu.no (M. Cepelka), kjell.malo@ntnu.no (K.A. Malo).

http://dx.doi.org/10.1016/j.conbuildmat.2017.08.089
0950-0618/

withdrawal properties of the grouted rod splice, and 2) to establish the contact stiffness of two mutually compressed mating timber end faces. The numerical simulations performed by finite element models enabled a deeper insight into the mechanical behaviour of the tested connections. Based on the findings from both the experimental and the numerical investigations, analytical relations are proposed for determining the rotational stiffness and the moment capacity intended for practical design.

2. Problem definition

The present splice connection is intended for large glulam sections with special focus on timber network arch bridges. The dominating internal force in such structures is compression transferred by the contact of timber end faces. Shear force can be transferred via shear keys. The design philosophy is based on utilizing high withdrawal stiffness and virtually non-existing initial slip of threaded rods to achieve rotationally stiff joints that can transfer the moderate bending moments. By providing sufficient effective length, the failure mode is driven by yielding of the steel rods. This enables a more reliable prediction of the structural properties and increased ductility of the joint. Since both the threaded rods and the steel couplers are embedded in the timber, the connection is durable, fire resistant and aesthetic. Both the threaded rods and the couplers can be pre-assembled prior to transport of the timber sections; this eases the mounting process on site. It should be noted, however, that the final setting time is affected by the curing of the glue, and the gluing operation on site implies quality control issues.

The main concern regarding implementation of splice joints in glulam arches is the required rotational stiffness of the joints. The flexural characteristics of this splice connection were studied using prototype splices of timber beams. The principal layout of the prototype beam splice connection is presented in Fig. 1.

3. Experimental tests

3.1. Tensile test of the rod splice

Tensile testing of the rod splice was carried out in order to verify sufficient strength and to determine the withdrawal stiffness of the system of rods and grout-filled couplers. In total, 6 tensile tests were conducted. In 3 of these tests, the relative displacements of the rods were monitored by two displacement transducers (confer Fig. 2). The mean value of these two measurements from each test was used to determine the deformation characteristics. Load was applied according to the loading procedure given in EN 26891:1991 [8].

3.2. Experimental determination of the stiffness at the interface of two mutually compressed mating timber end faces

The contact stiffness at the interface of two mutually compressed mating timber end faces was determined experimentally.

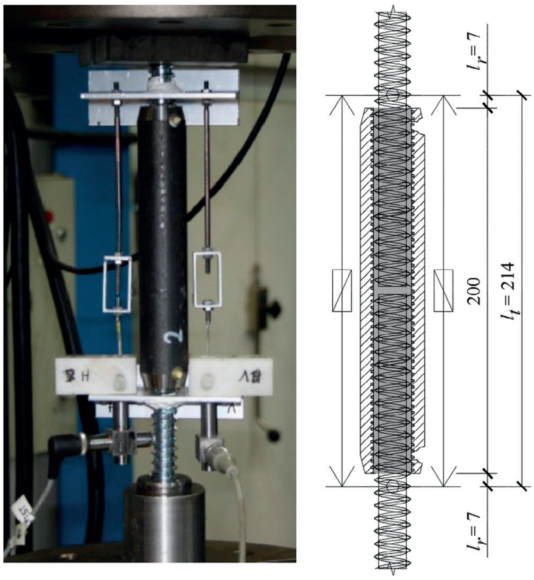

Fig. 2. Test set-up of tensile test of the rod splice (dimensions given in mm).

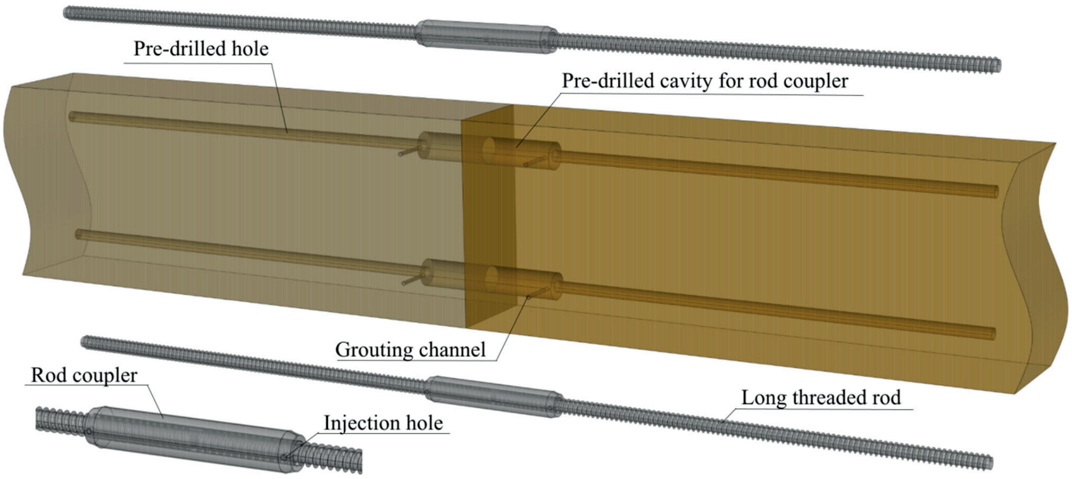

Fig. 1. Principal layout of splice connection with long threaded rods and grout-filled couplers.

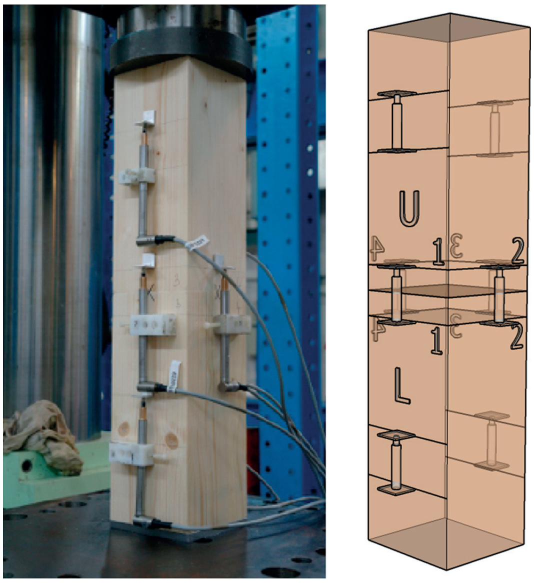

Fig. 3. Test configuration for determining the stiffness at the interface of two mutually compressed mating timber end faces.

The test configuration is shown in Fig. 3. Two timber specimens were placed on top of each other, with direct contact of end fibers, and compressed parallel to the grain. Displacements were monitored by 8 displacement transducers. Two transducers were attached to each specimen (U and L) at two opposite faces. Four other transducers were placed at each face at the interface between the specimens. In total, 12 tests were carried out. The specimens had rectangular cross-sections of 130 × 130 mm^2 and the length along the grain was 300 mm. The timber specimens were sawn from glulam beams of quality GL30c [9]. The test procedure followed EN 408 [10]. More details regarding the experimental test can be found in [11].

3.3. Beam splice test

The beam splice was tested in a four-point bending configuration leading to pure bending in the splice connection. The experimental set-up is shown in Fig. 4. The deformation characteristics were obtained by the digital image correlation (DIC) system ARAMIS [12] and subsequent linear regression of the measured horizontal displacement field for each time step. The measurements by DIC were validated by use of additionally applied transducers. In total, two rotational transducers (denoted T1 and T2 in Fig. 4) and three displacement transducers (denoted T3, T4 and T5) were placed across the end faces of the splice joint. The load was applied according to the loading procedure given in EN 26891:1991 [8].

Four test configurations were tested, see summary in Table 1 and illustrations in Fig. 5. The timber end faces of the spliced parts of the beam were placed in direct mutual contact in the configurations denoted by "C" ("C" for Contact). In the "G" configurations ("G" for Gap), the two timber parts were assembled with a 10 mm gap between the timber end faces.

The timber beams were made of glulam strength class GL30c [9] and had 140 mm width and 270 mm depth. The beams were fabricated with 45 mm thick lamellas of Norwegian spruce. The timber specimens were conditioned at the standard environment of 20 °C and 65% relative humidity.

The threaded rods were of type SFS WB-T-20 complying with DIN 7998 [13]. The outer diameter of the rods is 20 mm, the inner diameter is 15 mm. The strength class is 8.8 according to the manufacturer. The total length of the rods was 700 mm, but the initial 100 mm was glued in the rod coupler giving an effective length of the rods equal to $l_{ef} = 600$ mm (the rod length screwed in timber).

The steel couplers (Fig. 5 and Fig. 2) were purpose made, and manufactured from steel S355. The couplers were 200 mm long with an outer diameter of 35 mm. The inner surface of the couplers was machined with metric threads M24 giving a minimum inner diameter of approximately 22 mm. Grouting, by two-component epoxy adhesive Mapei Mapepoxy L, was carried out through inserted pair of metal injection tubes, see Fig. 5 (right).

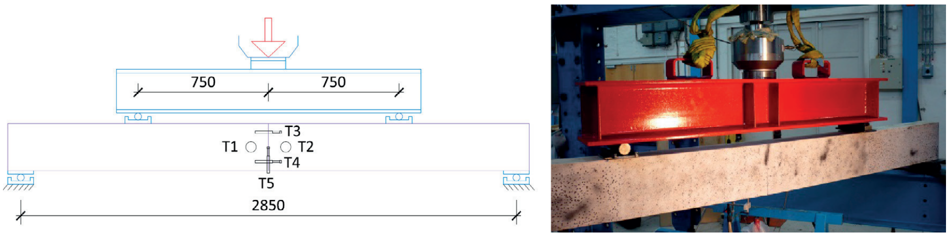

Fig. 4. Experimental set-up of beam splice test (dimensions given in mm).

Table 1
Summary of the tested beam splice configurations.

Config.	No. of tests	No. of rods		Timber faces
		Tension	Compression	
C1	3	1	0	Contact
C2	3	2	0	Contact
G1	3	1	1	Gap 10 mm
G2	2	2	2	Gap 10 mm

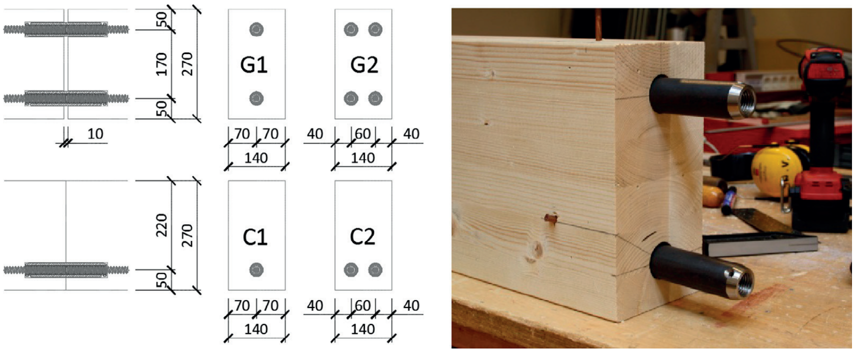

Fig. 5. Test configurations of beam splice and example of production of G1 specimen (dimensions given in mm).

4. Experimental results

4.1. Tensile test of the rod splice

All tensile tests exhibited tensile failures of the threaded rods, proving that the rod splice was stronger than the rods. Fig. 6 shows the force-displacement curves of the tensile tests, carried out by the arrangement of Fig. 2. The connection showed no initial slip. The mean determined axial stiffness of the rod splice, K_{co}, was 299 kN/mm (COV = 0.045). The stiffness was obtained by subtracting the deformation of the free lengths of the rods within the measured range outside the coupler (length $2l_r$ depicted in Fig. 2) from the total deformation measured in the experiments (over length l_t depicted in Fig. 2). Compared to the stiffness of just threaded rods of equal length, the rod splice is approximately 1.5 times stiffer. All couplers were cut open after the tests in order to visually verify the gluing efficiency. It was observed that glue filled the entire section of couplers with very low occurrence of air bubbles.

4.2. Experimental determination of the stiffness at the interface of two mutually compressed mating timber end faces

The stiffness at the interface of two mutually compressed mating timber end faces is affected by end grain effects. More details can be found in [11]. These end grain effects are described analytically by introducing a crushing zone in the vicinity of the timber end faces characterized by a crushing modulus, E_{cr}, and a crushing length, l_{cr}, schematically shown in Fig. 7.

The crushing length l_{cr} is assumed to be of equal size on both sides of the contact interface of the timber parts. With reference to Fig. 7, this length is:

$$l_{cr} = \frac{1}{2} \cdot (l_M - l_U - l_L) \tag{1}$$

where l_M is the range over which the displacements Δ_M were monitored and l_U and l_L are the lengths of the upper and the lower specimen within l_M, but outside the crushing zone. Displacements monitored by displacement transducers at the interface Δ_M involve 4 contributions (after deduction of initial slip): displacements due to deformation of the upper part, Δ_U, and of the lower part, Δ_L, and two displacements due to contact at end grains Δ_{cr}. This can be expressed as:

$$\Delta_M = \Delta_U + \Delta_L + 2 \cdot \Delta_{cr} \tag{2}$$

By assuming material and dimensional homogeneity along the entire length of the test specimens and applying a relation for axially loaded strut, $\Delta = F \cdot l/(E \cdot A)$, Eq. (2) can be written as:

$$\Delta_{cr} = \frac{1}{2} \cdot \left(\Delta_M - \frac{F \cdot l_U}{E_U \cdot A} - \frac{F \cdot l_L}{E_L \cdot A} \right) \tag{3}$$

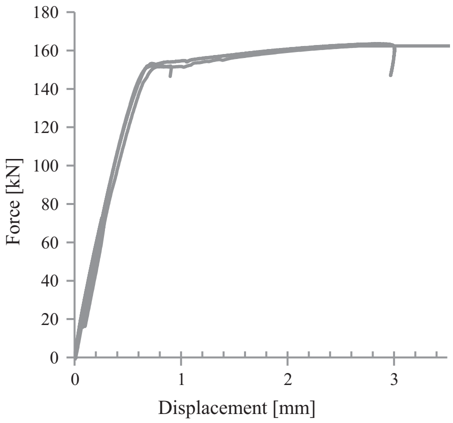

Fig. 6. Force-displacement curves obtained from the tensile tests of the rod splices.

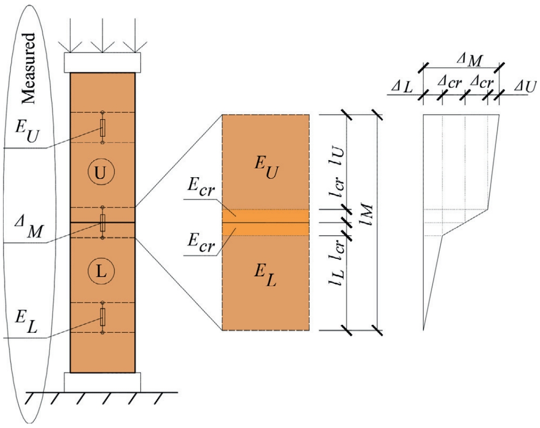

Fig. 7. Schematic illustration of the analytical representation of the crushing zone characteristics.

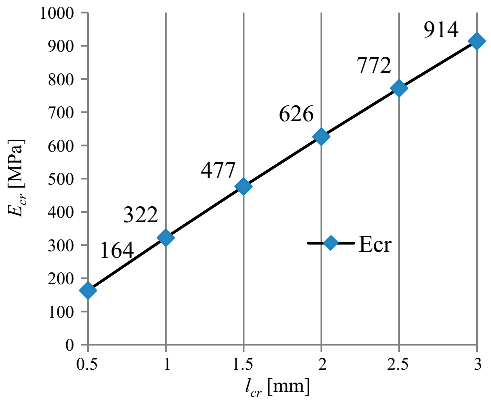

Fig. 8. Experimentally determined stiffness at the interface of two mating timber end faces.

where F is the applied force corresponding to the displacements Δ_M, E_U and E_L represent the modulus of elasticity of the upper and the lower specimen, respectively, and A is the cross-sectional area of the timber specimens.

The stiffness of the crushing zone is finally expressed by the crushing modulus E_{cr} and the crushing length l_{cr} as:

$$\frac{E_{cr}}{l_{cr}} = \frac{F}{A \cdot \Delta_{cr}} \tag{4}$$

The mean values of the experimental results (COV = 0.225) are presented in Fig. 8 for an extent of the crushing length up to 3 mm, which is considered to be the upper limit, based on observations during testing. The experimental results show that the crushing stiffness is much lower than the material stiffness. However, the extent of the crushing zone is very limited, of the order of 1 mm, as observed visually and identified from the measurements by displacement transducers. The deformation of the crushing zone during and after testing is illustrated in Fig. 9.

By comparing the stiffness of the crushing zone E_{cr}/l_{cr} given in Fig. 8, it can be noticed that the stiffness is not significantly affected by the extent of the crushing zone. For practical use, it is thus suggested to use $l_{cr} = 3$ mm with the corresponding $E_{cr} = 914$ MPa, yielding the stiffness of the crushing zone $E_{cr}/l_{cr} \cong 300\,\mathrm{N/mm^3}$.

4.3. Beam splice test

Experimental results of bending tests of the splice connections are given in terms of moment vs. rotation in the joint, see the plots in Fig. 10. The ultimate moment M_u, the elastic rotational stiffness k_θ and the distance of neutral axis from the upper timber edge a_0 (illustrated in Fig. 14) are presented in Table 2. The splice efficiency with respect to moment capacity, η_M, is the ratio between the measured ultimate moment and the mean bending capacity of the unspliced timber cross-section. The efficiency with respect to rotational stiffness, η_k, relates the mid-span deflection of an unspliced beam to that of a beam containing a splice connection (the respective deflections were obtained analytically by the principle of virtual work).

Fig. 9. Deformation of the crushing zone during testing (left), and deformation pattern at the end faces after testing (right).

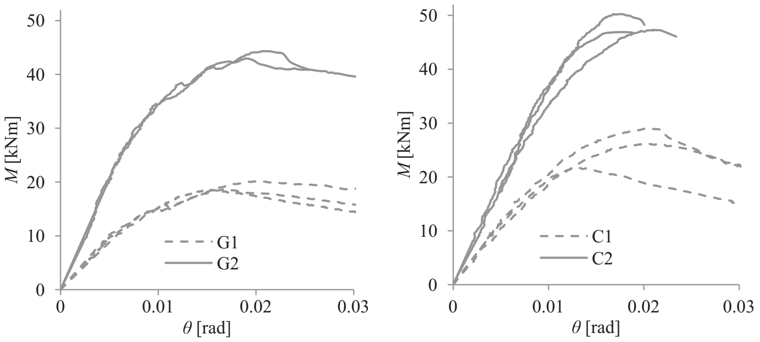

Fig. 10. Moment-rotation curves based on data from DIC monitored during bending tests.

Table 2
Experimental results of bending tests of splice connection.

Config. Mean	No. of tests	M_u			k_θ			a_0	
		[kNm]	COV	η_M[(a)]	[kNm/rad]	COV	η_k[(b)]	[mm]	COV
G1	3	19.1	0.05	27%	1826	0.08	48%	105	0.16
G2	2	43.6	0.02	62%	4016	0.02	67%	100	0.06
C1	3	25.6	0.14	36%	2093	0.08	52%	112	0.05
C2	3	48.1	0.04	69%	3749	0.07	66%	143	0.12

Input: GL30c.
(a) $f_{m,m} = 41.4$ MPa.
(b) $E = 13000$ MPa, $G = 650$ MPa.

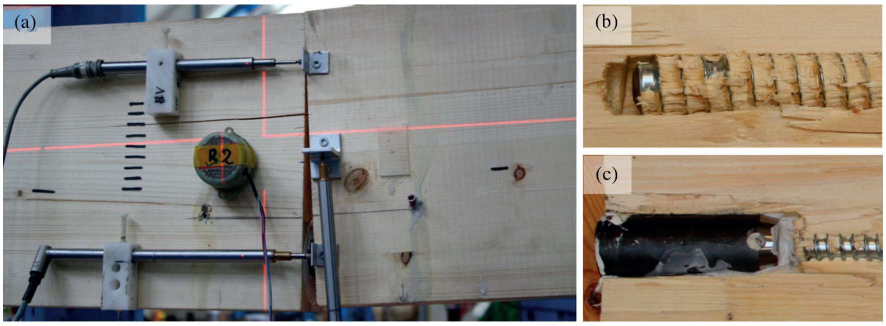

Fig. 11. Detail of a C2 specimen during testing (a), Cut-opened specimens after testing: Withdrawal failure of a tension rod (b), a compression coupler with the cavity in timber filled with glue (c).

All specimens failed due to withdrawal of the tension rods, see the detail at the rod-end in Fig. 11b. The C2 configuration was characterized by brittle failure occurring shortly after the ultimate capacity had been reached (see Fig. 10). This may indicate a risk of progressive failure of the group of rods caused by low ductility of withdrawal failure of rods parallel to the grain [14]. A crack parallel to the grain and close to the neutral axis occurred for two C2 specimens, see Fig. 11a. This crack is most likely induced by tensile stresses perpendicular to the grain caused by a change of slope at the rotated end faces.

The curves plotted in Fig. 10 are limited either by a rotation of 0.03 rad or by specimen failure. The relative rotations θ were obtained by linear regression of horizontal displacements, monitored by DIC along the entire length of the vertical sections (i.e. considering both deformations above and under the neutral axis) placed in the vicinity of the timber end faces. The values obtained by linear regression of DIC results were in good agreement with the rotations measured by the rotational transducers. Common for all tests: no initial slip was observed, facilitating an immediate load take-up in the joint. This is an important prerequisite for the moment resisting connections, especially in statically indeterminate structures, for which an additional deformation in the joint causes a redistribution of internal forces within the structure [15].

The relative moment capacities and rotational stiffnesses for configurations with two rods as compared to one rod show no obvious signs of a group effect in case of two rods (which suggests $n_{ef} = n$ with reference to EC5 [16] 8.7.2).

Some additional parameters obtained from the analysis of the bending test results in conjunction with the proposed analytical model, are summarized in Table 3.

It is interesting to notice that the withdrawal stiffness K_w obtained here, is considerably larger than the value obtained by withdrawal tests reported by Stamatopoulos et al. [14]. The latter was obtained from pure axial withdrawal of threaded rods in pull-push test configuration.

The crushing modulus E_{cr}, obtained from the bending tests, is much smaller than the value obtained from the separate tests, as described in Section 4.2. While the tests of end grain effects yield a uniform stress distribution in the compressed area, the bending tests produce a varying stress distribution in the compression zone. Another factor is uncertainty in the fabrication process of the splice connections. The joints were not pre-compressed during hardening of the glue in the rod couplers, and the planeness of the end surfaces was in general lower for the specimens of the bending tests. Consequently, the end faces may have had non-uniform contact.

5. Numerical model of beam splice tests

Numerical simulations of the beam splice were carried out by ABAQUS [17]. Each geometrical configuration tested in the

Table 3
Ultimate tensile force in rod F_{tu}, withdrawal stiffness of rod K_w, and crushing modulus E_{cr} obtained by analysis of beam splice test results.

All conf.	F_{tu}		K_w		E_{cr}[(a)]	
	[kN]	COV	[kN/mm]	COV	[MPa]	COV
Mean	128	0.11	264	0.10	114	0.24

(a) For C-configuration and assuming $l_{cr} = 3$ mm.

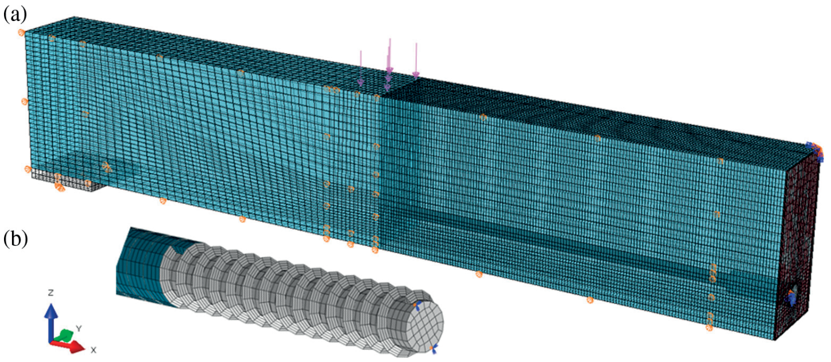

Fig. 12. Finite element model for C1 configuration (a) and detail of threaded rod with female part of surrounding timber (b).

experiments was modelled by eight-node brick elements with reduced integration and hour-glass control (C3D8R). Given the symmetry of the problem, only half the beam was modelled, see Fig. 12. Transverse displacements of the beam were prevented. Loading was applied by normal pressure at the top of the beam, corresponding to 4-point bending as shown in Fig. 4.

The contact stiffness between the end timber faces at the splice joint was modelled by implementing the "crushing zone" in the vicinity of the joint. The experimental values from the bending tests were used as an input to the numerical model (l_{cr} = 3 mm and E_{cr} = 114 MPa, see Table 3 and further discussion in Section 7.2).

The rods and their interaction with the timber were based on a numerical model presented in [14]. Contact properties between rod and timber utilize a "hard" contact behaviour in the normal direction and isotropic tangential behaviour with a coefficient of friction of 0.2. The rod couplers were not included in the numerical model. The axial stiffness of the rod splice in the coupler was accounted for by converting the experimentally obtained stiffness (K_{co} = 299 kN/mm, see Section 4.1) into an equivalent modulus of elasticity (338 GPa), applied to the initial 100 mm portion of the rod core (see Fig. 12b).

Material properties of wood were assumed to be transversely isotropic, see Table 4. Here, E is modulus of elasticity, G is shear modulus and ν is Poisson's ratio. The longitudinal direction (L) is the grain direction, and no distinction is made between tangential (T) and radial (R) directions. Steel was modelled as isotropic with E = 210 GPa and ν = 0.3.

6. Analytical model

Tests of timber splice connections using glued-in hardwood dowels [19] and glued-in rods [20,21] demonstrated the importance of incorporating the slip of connectors when predicting the height of the compression zone and the rotational stiffness. Moreover, it was observed in [20] that the stiffness of timber in compression is affected by deformation at end grains of the timber end faces. The present analytical model accounts for both slip of connectors and for deformation at end grains.

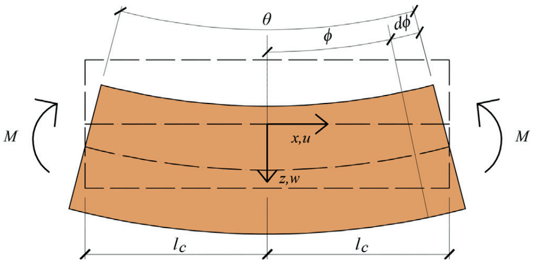

Fig. 13. Beam portion subjected to a bending moment.

6.1. Prediction of rotational stiffness

Fig. 13 shows the deformed state of a portion of a beam of length $2l_c$ subjected to a bending moment M. The bending moment produces a relative rotation θ at the end sections of the beam portion. By assuming small deformations and rotations, and Navier's hypothesis of plane sections remaining plane during deformation, the following relations of the Euler-Bernoulli beam theory apply:

$$\begin{aligned} &\phi \approx \tan\phi = -\tfrac{dw}{dx} \\ &\kappa = \tfrac{d\phi}{dx} = -\tfrac{d^2w}{dx^2} \\ &\varepsilon_x = z \cdot \tfrac{d\phi}{dx} = z \cdot \kappa \end{aligned} \tag{5}$$

The slope ϕ is also the rotation of the beam section (Navier), κ is the curvature of the deformed beam and ε_x is the longitudinal strain. Using (5), the relative rotation of the end sections of the beam portion is found to be:

$$\theta = \int_{-l_c}^{l_c} \frac{d\phi}{dx} dx = 2 \cdot \kappa \cdot l_c \tag{6}$$

Table 4
Material properties of wood used in numerical simulations.

E_L [MPa][a]	$E_R = E_T$ [MPa][a]	$G_{LR} = G_{LT}$ [MPa][b]	G_{RT} [MPa][b]	$\nu_{LR} = \nu_{LT}$ [–][b]	ν_{TR} [–][b]
13000	400	600	30	0.6	0.315

[a] Manufacturer: Moelven industrier ASA, class L40 (GL30c).
[b] Norwegian spruce [18].

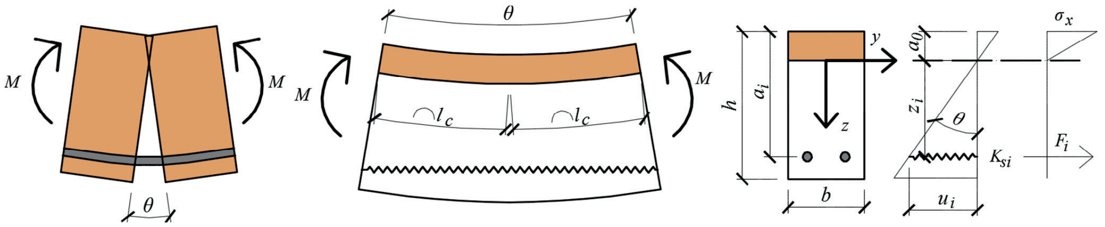

Fig. 14. Analytical model characteristics.

Solving Eq. (6) with respect to κ and inserting the result into the expression for ε_x in (5), Hooke's law gives:

$$\sigma_x = E \cdot \varepsilon_x = E \cdot z \cdot \frac{\theta}{2 \cdot l_c} \tag{7}$$

where σ_x is normal axial stress and E is modulus of elasticity parallel to the grain.

The analytical model is based on Eq. (6). Fig. 14 shows a deformed splice connection with a relative rotation θ of the end faces caused by the bending moment M. Here, h and b are height and width of cross-section respectively, a_0 is the height of wood in compression, a_i is a coordinate along z-axis of i-th row of the rods determined from the upper edge of wood in compression, l_c represents equivalent length of compression zone at each side of the connection, σ_x is normal stress in wood, K_{si} is axial stiffness of the i-th row of the rods, u_i is horizontal displacement at the i-th row of the rods and $z_i = a_i - a_0$ is the z-coordinate of the the i-th row of steel rods.

The relative rotation of the end faces of the splice connection is approximated by a relative rotation of the end sections of a beam portion of length $2l_c$. The flexural stiffness is thus governed by the deformation of the wooden part in compression and the elongation of a spring representing the axial stiffness of the steel rods.

The axial force in the i-th row of steel rods is found by:

$$F_i = K_{si} \cdot u_i = K_{si} \cdot \theta \cdot z_i \tag{8}$$

The horizontal force equilibrium reads:

$$\sum_{i=1}^{n} F_i - \int_0^{-a_0} \int_{-\frac{b}{2}}^{\frac{b}{2}} \sigma_x dydz = 0 \tag{9}$$

Using Eqs. (7) and (8), Eq. (9) takes the following form:

$$\sum_{i=1}^{n} K_{si} \cdot (a_i - a_0) - \frac{E \cdot b \cdot a_0^2}{4 \cdot l_c} = 0 \tag{10}$$

Finally, the height of wood in compression is obtained by solving Eq. (10) for a_0. The equation yields two roots, only one of which is physically possible:

$$a_0 = \frac{-\sum_{i=1}^{n} K_{si} + \sqrt{\left(\sum_{i=1}^{n} K_{si}\right)^2 + \frac{E \cdot b}{l_c} \cdot \sum_{i=1}^{n} K_{si} \cdot a_i}}{\frac{E \cdot b}{2 \cdot l_c}} \tag{11}$$

The moment at the connection about the y-axis is:

$$M = \sum_{i=1}^{n} F_i \cdot z_i - \int_0^{-a_0} \int_{-\frac{b}{2}}^{\frac{b}{2}} \sigma_x \cdot zdydz \tag{12}$$

Using Eqs. (7) and (8), Eq. (12) takes the following form:

$$M = \theta \cdot \left(\sum_{i=1}^{n} K_{si} \cdot z_i^2 + \frac{E \cdot b \cdot a_0^3}{6 \cdot l_c} \right) \tag{13}$$

The rotational stiffness of the connection k_θ is then obtained as:

$$k_\theta = \frac{M}{\theta} = \sum_{i=1}^{n} K_{si} \cdot z_i^2 + \frac{E \cdot b \cdot a_0^3}{6 \cdot l_c} \tag{14}$$

The axial stiffness of the i-th row of steel rods, K_{si}, is given by Eq. (15) and it is obtained as an effective stiffness of a system of three springs representing the axial withdrawal stiffnesses of the threaded rods at each side of the connection, denoted as K_w, and the axial stiffness of the joint of threaded rods in the rod coupler, denoted as K_{co}. The number of steel rods in one row is denoted as n_r.

$$K_{si} = n_r \cdot \frac{K_w \cdot K_{co}}{2 \cdot K_{co} + K_w} \tag{15}$$

The equivalent length of compression zone, l_c, consists of two contributions as shown in Fig. 15, and is given by the following equation:

$$l_c = l_0 + l_{cr} \cdot \frac{E}{E_{cr}} \tag{16}$$

where l_0 is the effective length of the compression zone, and E_{cr} and l_{cr} are the crushing modulus and the crushing length, respectively.

The effective length of the compression zone, l_0, characterizes the compliance of the wood in compression. This length approximately defines a local area, in close proximity to the splice joint, for which the Navier's hypothesis is violated and where the stress state is a combination of compression stresses parallel to the grain, tensile stresses perpendicular to the grain and shear stresses.

It is proposed to estimate l_0 as a simple function of the height of the timber cross-section h:

$$l_0 = 0.85 \cdot h \tag{17}$$

This relation was obtained based on investigations using numerical models. Given validity of the form of Hooke's law and Navier's hypothesis adopted for the model, the length l_0 within the compression zone reads $l_0 = E \cdot u / \sigma_x$. The extent of the

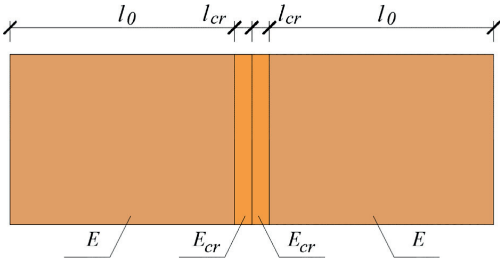

Fig. 15. Graphical representation of the equivalent length of the compression zone.

horizontal displacements u is a function of the height of the cross-section h, elastic moduli parallel (E_0) and perpendicular (E_{90}) to the grain, and shear modulus G. A parametric numerical study showed that l_0 is constant for constant relations between E_0, E_{90}, and G, which is the case for structural timber ($G = E_0/16$, $E_{90} = E_0/30$ in [22]) and which can also be assumed to be valid for glulam. The suggested length l_0 in Eq. (17) is thus independent of the timber strength class.

The deformation at the end grains of two mutually compressed mating timber end faces is described by the second contribution in Eq. (16). It is derived by introducing a crushing zone characterized by a crushing modulus, E_{cr}, and a crushing length, l_{cr}. The parameters of the crushing zone were obtained experimentally. A comparison of the horizontal displacements at the splice joint, obtained by numerical models, with and without a crushing zone, is demonstrated in Fig. 16 (left). An example of the horizontal displacements over the beam height at the splice joint, obtained by DIC during one of the bending tests, is shown to the right in Fig. 16. Fig. 16 demonstrates good agreement between the numerical model with the crushing zone (blue line) and measurement by DIC.

The determination of the position of the neutral axis and the rotational stiffness in the configuration with no contact of timber end faces is carried out by use of Eqs. (10) and (14), respectively, with omitting the terms associated with the compression stresses in the timber.

6.2. Prediction of moment capacity

For one single row of threaded rods in the tension side, or one in the tension and one in the compression side, the moment capacity is obtained from simple moment equilibrium of compression and tension force acting at the joint:

$$M_u = \min(F_{tu}; F_{cu}) \cdot z_c \tag{18}$$

where F_{tu} and F_{cu} are the ultimate strengths of components in tension and compression obtained by Eq. (19), and z_c is the lever arm of the internal forces. With reference to Fig. 14, z_c is determined by assuming that F_{cu} acts at $a_0/3$.

$$\begin{aligned} F_{tu} &= n_r \cdot \min(R_{axu}; R_u) \\ F_{cu} &= \tfrac{1}{2} \cdot b \cdot a_0 \cdot f_{c,0} \end{aligned} \tag{19}$$

Here, $f_{c,0}$ is the timber strength in compression parallel to the grain, R_u is the tensile strength of the rods (provided by the manufacturer) and R_{axu} is the ultimate withdrawal strength of threaded rods.

6.3. Ultimate withdrawal strength of threaded rods

The withdrawal strength of threaded rods R_{ax} was determined by Stamatopoulos et al. [23]. However, in this particular connection, the rods are loaded by a combination of axial withdrawal force and local bending moment induced by the rotational restraint at the point where the rod enters the coupler. Hence, the ultimate withdrawal strength of the rods, R_{axu}, is less than that of rods in pure tension, R_{ax}. Since the withdrawal strength of threaded rods is (approximately) a linear function of the effective length [23], the ultimate withdrawal strength is determined on the basis of a reduced effective length of the threaded rods:

$$R_{axu} = R_{ax} \cdot \left(\frac{l_{ef} - l_x}{l_{ef}} \right) \tag{20}$$

The effective length of the threaded rods (length of the rod screwed in timber) is denoted l_{ef}, whereas l_x is a free length of rod that is not considered to contribute to the withdrawal capacity.

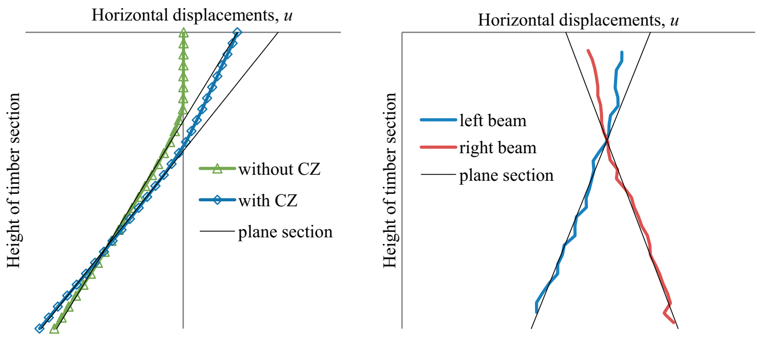

Fig. 16. Horizontal displacements along vertical sections at beam joint: Left: Output from numerical models with and without crushing zone (CZ), Right: Example of results obtained by DIC during one of the bending tests.

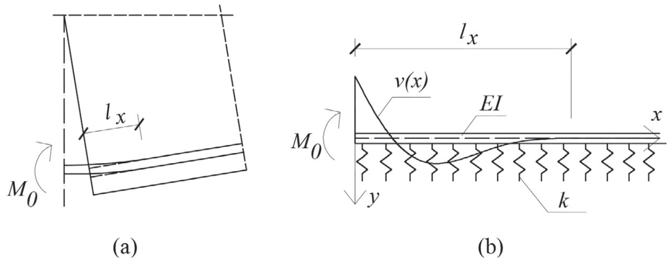

(a) (b)

Fig. 17. Simplified illustration (rod couplers are not included) of an imposed local bending moment at the end of the rod (a), analogy with semi-infinite beam on elastic foundation (b).

This free length is estimated as follows. In the same way as the models developed for connections with fully threaded self-tapping screws [24], the threaded rod is considered as a semi-infinite beam on elastic foundation loaded by a bending moment M_0, see Fig. 17.

The differential equation for the deflection curve of a beam supported on an elastic foundation is:

$$EI\frac{d^4y}{dx^4} = -k \cdot y \tag{21}$$

where k is the foundation stiffness (N/mm^2) and EI represents the flexural stiffness of the beam. By introducing the characteristic length λ and solving the differential equation with boundary conditions corresponding to the arrangement shown in Fig. 17b, the deflection curve becomes [25]:

$$y = \frac{2M_0 \cdot \lambda^2}{k} e^{-\lambda \cdot x}(\cos(\lambda \cdot x) - \sin(\lambda \cdot x)); \lambda = \sqrt[4]{\frac{\mathrm{k}}{4\mathrm{EI}}} \tag{22}$$

The length l_x is found by solving Eq. (22) with respect to x for $y = 0$, and considering the second period, see Fig. 17b:

$$l_x = \frac{5\pi}{4\lambda} = \frac{5}{8}\pi \cdot d_c \cdot \sqrt[4]{\frac{\pi \cdot E_s}{k_t}} \tag{23}$$

where d_c is the core diameter of the threaded rods, E_s is the elastic modulus of steel and k_t is the foundation modulus of timber transverse to the grain.

7. Model evaluation compared to experimental results

Table 6 presents an overview of experimentally, analytically and numerically obtained parameters. The input parameters to the analytical model are summarized in Table 5. For the nomenclature of the input parameters, see Section 6.

7.1. Analytical model comparison to experimental results

The analytical model gives, in general, good estimates of both the rotational stiffness and the moment capacity, see Table 6. The predicted rotational stiffness for the C configurations is conservative due to the assumed planeness of end timber sections (Navier). However, the Navier's hypothesis is, in fact, violated in close proximity to the end timber faces, as shown in Fig. 16. In the experiments, the reduced horizontal displacements within the compression zone result in a lower monitored rotation and thus a higher rotational stiffness.

The prediction of moment capacity for the C configurations, with the neutral axis determined by the assumed elastic behaviour by Eq. (11), is somewhat conservative. Conferring Table 6, the predicted capacities are approximately 15% lower, compared to experimental results. As the tensile forces in the rods approach the ultimate withdrawal strength, the withdrawal stiffness of the rods gradually decreases [14,23]. The neutral axis thus gradually moves towards the upper edge of the timber cross-section and the lever arm of the internal forces increases. However, the increasing rotation in the joint gives rise to shear stresses and tensile stresses perpendicular to the grain in the compression zone, due to change of slope at the rotated end faces, as shown in Fig. 16. It was observed in the experiments that the possible "plastification" of the compression zone is accompanied by occurrence of cracks along the grain near the neutral axis, see Fig. 11a. If no measures are taken to reinforce the timber perpendicular to the grain, it is most appropriate to predict the moment capacity based on the elastic behaviour assumption.

The crushing modulus E_{cr} based on the experimental results obtained from the bending tests was used as an input parameter to the analytical model. The use of crushing modulus obtained from the uniaxial tests of end grain effects provided overly stiff predictions, compared to the results from the bending tests.

From the cut-outs of the specimens after tests, it was observed that voids in the timber around the steel couplers were well filled with glue (see Fig. 11c), which allowed a force transfer between the couplers and the timber at the compression side. Consequently, the axial stiffness K_{si} at the compression side, monitored in experiments, was 2.2 times higher than the stiffness at the tension side. This was taken into account in the neutral axis prediction by the analytical model. The "pushing-in" stiffness of long threaded rods was studied using numerical models. This stiffness was found to be 1.1 times higher than the withdrawal stiffness, K_w, of the rods.

7.2. Numerical model comparison to experimental results

The numerical model predicts the rotational stiffness for the C configurations with good accuracy, while the rotational stiffness for the G configurations is underestimated by approximately 25%, confer Table 6. The distance of the neutral axis from the upper timber edge a_0, obtained by the numerical models for the G configurations, is somewhat larger than obtained experimentally. These discrepancies are caused by the fact that the numerical model does

Table 5
Input parameters to the analytical model.

K_w [kN/mm]	K_{co} [kN/mm]	E [MPa]	E_{cr} [MPa]	l_{cr} [mm]	R_{ax} [kN]	k_t [MPa]
264 Table 3	299 Sect. 4.1	13000 Table 2	114 Table 3	3 Table 3	161 [23](a)	710 [26,27](b)

(a) Mean value from experimental investigation.
(b) Average of experimental results for spruce and steel dowels of diameter 16 mm (763 MPa [26] and 658 MPa [27]).

Table 6
Result comparison for ultimate moment M_u, rotational stiffness k_θ, and distance of neutral axis from the upper timber edge a_0.

Config. Mean	M_u [kNm]		k_θ [kNm/rad]			a_0 [mm]		
	Exp.	Anal.	Exp.	Anal.	Num.	Exp.	Anal.	Num.
G1	19.1	20.2	1826	1818	1294	105	103	132
G2	43.6	40.3	4016	3636	2762	100	103	132
C1	25.6	21.7	2093	1787	2126	112	113	108
C2	48.1	41.4	3749	2577	3458	139	136	137

not account for the contact forces between the rod couplers and the timber. A possible future improvement of the model can be facilitated by physically modelling the steel couplers and defining contact surfaces between the rods and the couplers, and between the couplers and the timber.

The mean withdrawal stiffness obtained by the numerical analyses was 258 kN/mm, which is in good agreement with the experimentally obtained value.

Similar to the analytical model, E_{cr} obtained from the bending tests was used as an input to the numerical models. The use of the crushing modulus obtained from the uniaxial tests of end grain effects yielded an excessively stiff model, compared to the results from the bending tests.

8. Concluding remarks

The investigation revealed that high moment capacity and rotational stiffness of timber splice connection can be achieved by application of long threaded rods. The tested connection showed no initial slip, which is an important pre-requisite for an application in moment-resisting connections. A rather brittle failure, caused by withdrawal of the threaded rods, was encountered for all experimental tests of the splice connection. The ductility was, however, much higher than for unspliced timber beams. Both ductility and capacity of the connection can be enhanced by yielding in rods, achieved by use of larger effective length of the rods.

Capacity and withdrawal stiffness of the rod splice, by grout-filled couplers, were sufficient and reliable. None of the experimental tests failed at the joint of the rods. The grouting process was straightforward and easy to implement.

The finite element model simulates effectively flexural behaviour of the joint. Application of a crushing zone at the joint allows for modelling of end grain effects of two mutually compressed timber end faces.

The proposed analytical models yield slightly conservative estimates of both the rotational stiffness and the moment capacity of the splice connection. Input parameters to these models are proposed based on the numerical analyses and the experimental tests.

The orientation of the threaded rods in the grain direction enables direct force transfer in the axial direction. It also utilizes the high withdrawal stiffness of rods parallel to the grain. On the other hand, since withdrawal of the rods is characterized by brittleness, it can lead to progressive failure of a group of rods. Furthermore, the development of shrinkage cracks (in the grain direction) in close proximity to the threaded rods can lead to loss of capacity. These shortcomings can be overcome by using long threaded rods with a small inclination to the grain. Further investigations are, however, necessary to examine for instance the effect of an implied lateral force component at the end of the rods.

Acknowledgments

This work was funded by the WoodWisdom-Net+ project DuraTB ("Durable Timber Bridges") and the support from the funding bodies and partners is gratefully acknowledged. The authors would also like to acknowledge Mathias Strøm and Christoffer Aune Moe for their important contributions and experimental work.

References

[1] T. Dyken, Trebruer – Statens Vegvesens rapport Nr.422 (Timber bridges – Norwegian Public Roads Administration report Number 422), Statens Vegvesen (Norwegian Public Roads Administration), 2017.
[2] F. Colling, Glued laminated timber – Production and strength classes, Timber Engineering STEP 1, 1995.
[3] K. Bell, Structural systems for glulam arch bridges, International Conference on Timber Bridges (ICTB 2010), Lillehammer, Norway, 2010.
[4] K.A. Malo, A. Ostrycharczyk, R. Barli, I. Hakvåg, On development of network arch bridges in timber, International Conference on Timber Bridges (ICTB 2013), Las Vegas, USA, 2013.
[5] M. Cepelka, K.A. Malo, Review on on-site splice joints in timber engineering, COST-Timber Bridges Conference 2014, Biel/Bienne, 2014.
[6] P. Dietsch, R. Brandner, Self-tapping screws and threaded rods as reinforcement for structural timber elements – a state-of-the-art report, Constr. Build. Mater. 97 (2015) 78–89.
[7] R. Tomasi, A. Crosatti, M. Piazza, Theoretical and experimental analysis of timber-to-timber joints connected with inclined screws, Constr. Build. Mater. 24 (9) (2010) 1560–1571.
[8] CEN, EN 26891:1991 (ISO 6891:1983) Timber structures, Joints made with mechanical fasteners, General principles for the determination of strength and deformation characteristics 1991.
[9] CEN, EN 14080:2013, Timber structures-glued laminated timber and glued solid timber – requirements, European Committee for Standardization, 2013.
[10] CEN, EN 408:2010+A1:2012: Timber structures – structural timber and glued laminated timber – determination of some physical and mechanical properties, European Committee for Standardization, 2012.
[11] M. Cepelka, K.A. Malo, Experimental study of end grain effects in timber joints under uniaxial compression load, in: W.W. J. Eberhardsteiner, A. Fadai, M. Pöll (Eds.) Proceedings of the World Conference on Timber Engineering (WCTE 2016), August 22–25, 2016, Vienna University of Technology, Austria, ISBN: 978-3-903039-00-1, Vienna, Austria, 2016.
[12] GOM Optical Measuring Techniques, ARAMIS, User Manual-Software, 2009.
[13] DIN, DIN 7998, Gewinde und Schraubenenden für Holzschrauben (Threads and screws for wood), Deutsches Institut für Normung, Berlin, 1975.
[14] H. Stamatopoulos, K.A. Malo, Withdrawal stiffness of threaded rods embedded in timber elements, Constr. Build. Mater. 116 (2016) 263–272.
[15] A.J.M. Leijten, Requirements for moment connections in statically indeterminate timber structures, Eng. Struct. 33 (11) (2011) 3027–3032.
[16] CEN, EN 1995-1-1:2004, Design of timber structures. Part 1–1: General-common rules and rules for buildings, European committee for standarization, Brussels, 2004.
[17] D.S.S.C. DSS, Abaqus analysis user's guide, Version 6.14, 2014.
[18] K.B. Dahl, Mechanical properties of clear wood from Norway spruce. Dissertation, Department of Structural Engineering, Norwegian University of Science and Technology, 2009.
[19] T. Sasaki, A. Koizumi, J.L. Jensen, Y. Iijima, Y. Tamura, K. Komatsu, End joint with glued-in hardwood dowels in timber construction I. Bending properties of beams jointed with single row of dowels, Mokuzai Gakkaishi/J. Jpn. Wood Res. Soc. 45 (1) (1999) 17–24.
[20] J.L. Jensen, P. Quenneville, Connections with glued-in rods subjected to combined bending and shear actions, CIB-W18/42-7-9 International council for research and innovation in building and construction working commission W18 -Timber structures, 2009.
[21] B.H. Xu, A. Bouchaïr, P. Racher, Analytical study and finite element modelling of timber connections with glued-in rods in bending, Constr. Build. Mater. 34 (2012) 337–345.
[22] CEN, EN 338:2009, Structural timber – Strength classes, European Committee for Standardization, 2009.
[23] H. Stamatopoulos, K.A. Malo, Withdrawal capacity of threaded rods embedded in timber elements, Constr. Build. Mater. 94 (2015) 387–397.
[24] F. Moshiri, R. Shrestha, K. Crews, The Predictive Model for Stiffness of Inclined Screws as Shear Connection in Timber-Concrete Composite Floor, RILEM Bookseries, 2014, pp. 443–453.
[25] M. Hetényi, Beams on Elastic Foundation: Theory with Applications in the Fields of Civil and Mechanical Engineering, The University of Michigan Press, Baltimore, 1946.
[26] N. Gattesco, Strength and local deformability of wood beneath bolted connectors, J. Struct. Eng. 124 (2) (1998) 195–202.
[27] N. Gattesco, I. Toffolo, Experimental study on multiple-bolt steel-to-timber tension joints, Mater. Struct. 37 (266) (2004) 129–138.

Paper ii

Effect of rod-to-grain angle on capacity and stiffness of axially and laterally loaded long threaded rods in timber joints

Martin Cepelka, Kjell Arne Malo, Haris Stamatopoulos

Under review in an international scientific journal (2017)

Effect of rod-to-grain angle on capacity and stiffness of axially and laterally loaded long threaded rods in timber joints

Martin Cepelka[1*], Kjell Arne Malo[1**], Haris Stamatopoulos [1***]

[1] Department of Structural Engineering, Norwegian University of Science and Technology (NTNU), Rich. Birkelandsvei 1A, 7491, Trondheim, Norway

[*] corresponding author, martin.cepelka@ntnu.no , +4795409031

[**] kjell.malo@ntnu.no

[***] haris.stamatopoulos@ntnu.no

Abstract

Long threaded rods have recently been widely used as a reinforcement of glued laminated timber in perpendicular to the grain direction. The recent research has thus focused mainly on the withdrawal properties of the threaded rods in the axial direction. Utilizing their large withdrawal stiffness and strength, the threaded rods can also effectively be used as connectors in moment resisting timber joints. Yet, in joints, the threaded rods are often imposed to a non-axial loading, due to inclination of the rod axis to the grain as well as loading direction different from the rod axis. No design models are currently available for the combined axial and lateral loading of the threaded rods. In the present work, the effects of the rod-to-grain and load-to-rod angles on capacity and stiffness of the threaded rods are investigated by use of experiments and finite element models. Based on those, analytical expressions for determining stiffness and capacity of axially and laterally loaded threaded rods are proposed, intended as a basis for practical joint design. Furthermore, effect of various boundary conditions applied at the rod-ends is studied.

Keywords: long threaded rod, timber joint, combined axial and lateral loading, glulam, 3D finite element model, capacity, stiffness

1. Introduction

The recently erected 14-storey timber building in Bergen in Norway – Treet, demonstrates new possibilities in the modern timber engineering design (Malo et al. 2016). The load-bearing structure consists of glulam column-beam trusses with slotted-in steel plates and dowels used in joints. The stability of the structure is ensured by diagonal components in the trusses. Alternatively, the horizontal stiffness of buildings can be enhanced by increased rotational stiffness in joints that also enables larger spans between columns. Compared to buildings made of massive cross-laminated panels (CLT), the glulam frames provide an open interior and thus more flexibility for architects and building owners.

Joints with large rotational stiffness can be obtained by use of long threaded rods (Malo and Stamatopoulos 2016). The rods are often inclined with respect to grains, as illustrated in Fig. 1. This allows accommodating longer rods in columns, and decreases risk for loss of capacity in beams, due to longitudinal shrinkage cracks in close proximity to the rods. The long threaded rods feature high withdrawal stiffness and capacity in the axial direction. However, the inclination of the rods, as well as simultaneous bending and shear actions in the joints, results in combined axial and lateral loading of the rods, which decreases their capacity and stiffness. Therefore, the designer must choose an optimal inclination of the rods. Currently, there are no available models for long threaded rods accounting for combined axial and lateral loading. The withdrawal properties of long threaded rods for pure axial load were studied by Stamatopoulos and Malo (2015); (2016) and Blaß and Krüger (2010). Several studies were conducted for timber-to-timber joints with inclined self-tapping screws, see e.g. (Bejtka and Blaß 2002; Jockwer et al. 2014; Tomasi et al. 2010). In addition, few design guidelines are given by Eurocode 5 (CEN 2004). The suitability of the different models for long threaded rods used in joints is, however, unclear.

The present work aims to assist the designer in optimizing the joint performance in terms of capacity and stiffness. The effects of rod-to-grain angle combined with different load and rod axis directions on capacity and stiffness are here investigated by use of experiments and numerical models. An analytical model for predicting the stiffness of threaded rods with varying rod-to-grain and load-to-rod angles is proposed, accounting for different boundary conditions at the rod-ends. Furthermore, an assessment of the applicability of the capacity prediction by Eurocode 5 (CEN 2004), and by the model proposed by Jockwer et al. (2014) for self-tapping screws, is carried out on basis of the experimental results.

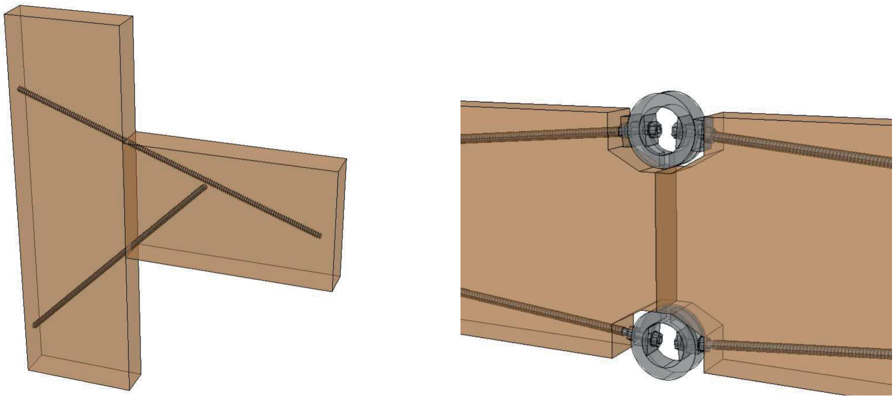

Fig. 1 Prototype timber joints by use of long threaded rods

2. Materials and methods

2.1. Theoretical prediction of capacity and stiffness

2.1.1. Capacity

Axial capacity

The withdrawal capacity of long threaded rods is commonly specified by producers in their respective technical approvals. According to the producer of the rods used in the present investigation (SFS WB) (DiBt 2015), the withdrawal capacity can be determined by:

$$R_{ax,k} = 70 \cdot 10^{-6} \cdot \rho_k^{\ 2} \cdot d \cdot l_{ef} \tag{1}$$

where $R_{ax,k}$ is the characteristic withdrawal capacity, ρ_k is the characteristic value of the timber density, d is the outer diameter of threaded rods and l_{ef} is the effective length of rods screwed in timber. The relation is independent of the rod-to-grain angle γ, however, its validity is restricted to γ = 45-90°, and $4 \cdot d \leq l_{ef} \leq 1000\,\text{mm}$.

The current version of Eurocode 5 (CEN 2004) provides the following relation for the determination of withdrawal capacity of a single screw with $d > 12$ mm and $\gamma \geq 30°$:

$$R_{ax,k} = \frac{f_{ax,k} \cdot d \cdot l_{ef}}{1.2 \cdot \cos^2 \gamma + \sin^2 \gamma} \cdot \left(\frac{\rho_k}{\rho_a} \right)^{0.8} \tag{2}$$

where $f_{ax,k}$ is the characteristic withdrawal parameter perpendicular to the grain determined in accordance with EN14592 for the associated density ρ_a. Since $f_{ax,k}$ must be determined experimentally, the relation is of little practical use.

Stamatopoulos and Malo (2015) determined the withdrawal capacity of long threaded rods valid for γ = 0-90°. The proposed relation is based on the classical Volkersen theory (Volkersen 1938), for which the particular solution depends on the assumed mode of force transfer between the rod and the surrounding timber. For a general use of rods in joints, it is considered most appropriate to adopt the so-called pull-shear boundary conditions, yielding the following relations:

$$\frac{R_{ax,mean}}{\pi \cdot d \cdot l_{ef} \cdot f_w} = \left(\frac{\sin(m \cdot \omega \cdot \lambda_u)}{m \cdot \omega} + \frac{\tanh((1-\lambda_u) \cdot \omega) \cdot \cos(m \cdot \omega \cdot \lambda_u)}{\omega} \right) \tag{3}$$

$$\begin{gathered} \omega = \sqrt{\frac{\pi \cdot d \cdot \Gamma_e \cdot l_{ef}^2}{A_s \cdot E_s}}; \ \Gamma_e = \frac{9.35}{1.5 \cdot \sin^{2.2}(\gamma) + \cos^{2.2}(\gamma)}; \\ f_w = \frac{4.35}{0.91 \cdot \sin^2(\gamma) + \cos^2(\gamma)}; \ m = \frac{0.332}{1.73 \cdot \sin(\gamma) + \cos(\gamma)} \end{gathered} \tag{4}$$

where E_s is the elastic modulus of steel, A_s is the cross-sectional area of the threaded rod (with a thread root diameter) and the parameter λ_u is determined from a chart provided by Stamatopoulos and Malo (2015), or conservatively taken equal to 1.0. The material parameters are optimized for glulam class GL30c of Norwegian spruce.

Lateral capacity

Eurocode 5 (CEN 2004) adopts the European Yield Model (Johansen 1949), and it provides a set of relations for the determination of the lateral capacity (per fastener and shear plane) depending on the expected failure mode. The failure mode associated with the present investigation is a single plastic hinge in the fastener located in the timber member, giving the following relation:

$$R_{v,Rk} = \sqrt{2 M_{y,Rk} \cdot f_{h,k} \cdot d_{ef}} + \frac{R_{ax,k}}{4} \tag{5}$$

where d_{ef} is the effective screw diameter, which for threaded rods is determined as $d_{ef} = 1.1 d_1$, $f_{h,k}$ is the characteristic embedment strength, and $M_{y,Rk} = 0.3 \cdot f_{u,k} \cdot d_{ef}^{2.6}$ is the characteristic fastener yield moment. For screws, the rope effect ($R_{ax,k} / 4$) is limited to 100 % of the Johansen's term. In the relation given in EC5, the Johansen's term is multiplied by a factor 1.15. This factor takes into account the different material safety factors (γ_M) for steel and timber, and it is not applicable when mean values are used.

For axially and laterally loaded self-tapping screws, Jockwer et al. (2014) proposed a modification of the Johansen's relation, assuming that timber does not resist lateral loads of screws within a distance x_1 from the timber edge:

$$R_{v,pulling} = -f_h \cdot x_1 \cdot d_{ef} + \sqrt{\left(2M_y + f_h \cdot x_1^2 \cdot d_{ef}\right) f_h \cdot d_{ef}} \tag{6}$$

$$x_1 = \frac{f_h \cdot d_{ef}}{2\tan(\gamma) \cdot f_{v,roll}} \tag{7}$$

where $f_{v,roll}$ is the rolling shear strength. A mean embedment strength proposed by Blaß et al. (2006) was used by Jockwer et al. (2014):

$$f_{h,mean} = \frac{0.022 \cdot \rho^{1.24} \cdot d^{-0.3}}{2.5 \cdot \cos^2(\gamma) + \sin^2(\gamma)} \tag{8}$$

While the relation in Eq. (8) was obtained by curve-fitting to the experimental results with self-tapping screws of d = 6-12 mm, Eurocode 5 (CEN 2004) suggests to determine the value of the embedment strength f_h for screws with d > 6mm as:

$$f_{h,\alpha,k} = \frac{0.082(1 - 0.01 \cdot d_{ef})\rho_k}{k_{90} \cdot \sin^2(\alpha) + \cos^2(\alpha)} \tag{9}$$

where α is the angle of the load to the grain, and k_{90} is, for softwoods, determined as $k_{90} = 1.35 + 0.015 \cdot d_{ef}$.

Capacity under combined axial and lateral loading

According to Eurocode 5 (CEN 2004), axially and laterally loaded screws shall satisfy the following condition:

$$\left(\frac{F_{ax}}{R_{ax}}\right)^2 + \left(\frac{F_v}{R_v}\right)^2 \le 1 \tag{10}$$

where F_{ax} and F_v are the load components in axial and lateral directions, respectively. By defining ψ as the angle between the rod axis and the resultant force (see Fig. 2a), the resultant force can be decomposed such as $F_{ax} = F \cdot \cos(\psi)$ and $F_v = F \cdot \sin(\psi)$, which inserted into Eq. (10), gives the following relation for the capacity R under combined axial and lateral loading:

$$R = \frac{R_{ax} \cdot R_v}{\sqrt{R_{ax}{}^2 \cdot \sin^2(\psi) + R_v{}^2 \cdot \cos^2(\psi)}} \tag{11}$$

Based on work of Bejtka and Blaß (2002), Jockwer et al. (2014) proposed to determine the capacity under combined axial and lateral loading for inclined screws as:

$$R = R_{ax,ef} \cdot \cos(\psi) + R_{v,pulling} \cdot \sin(\psi) \tag{12}$$

where $R_{ax,ef}$ is the withdrawal capacity determined with reduced effective length of screw by subtracting the length x_1 (Eq.(7)) from l_{ef}.

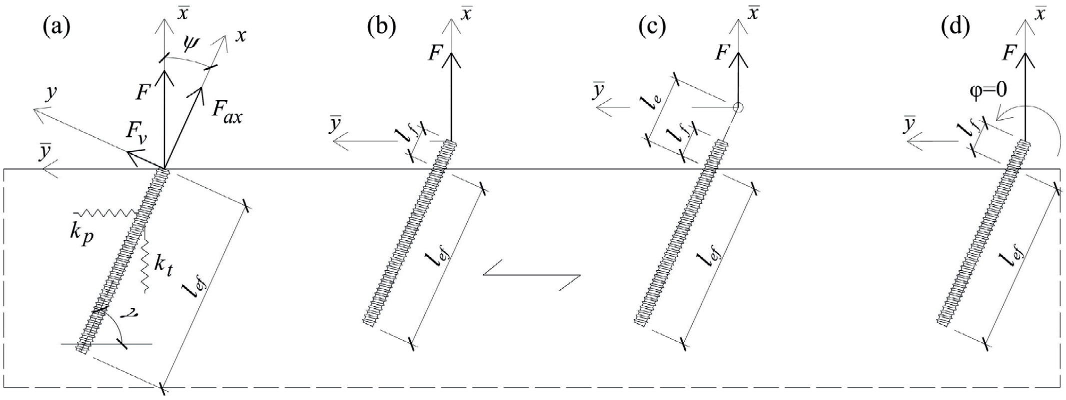

Fig. 2 Definition of terms in conjunction with stiffness prediction: (a) loading of the rod-end at the level of timber face, (b) loading of the rod-end eccentric to the timber face, (c) eccentric loading corresponding to the experimental set-up (see Section 2.2), (d) eccentric loading with restrained rotation (φ = 0) of the rod-end

2.1.2. Stiffness

Axial stiffness

The axial withdrawal stiffness of threaded rods can be determined based on the classical Volkersen theory (Volkersen 1938) by the relation proposed by Jensen et al. (2001) for glued-in hardwood dowels and later applied for threaded rods by Stamatopoulos and Malo (2016):

$$K_w = \pi \cdot d \cdot l_{ef} \cdot \Gamma_e \cdot \frac{\tanh(\omega)}{\omega} \tag{13}$$

The input parameters, by assuming a pull-shear boundary conditions, are defined in Eq. (4).

Neither the technical approval (DiBt 2015), nor Eurocode 5 (CEN 2004) provides a relation for determining the axial withdrawal stiffness of long threaded rods. Some expressions can be found in other technical approvals for self-tapping screws. However, these expressions cannot be extrapolated outside their valid range as they provide inaccurate predictions (Stamatopoulos 2016).

The axial stiffness of the free part of the rod not embedded in timber is determined as $K_{ax,f} = E_s \cdot A_s / l_f$, where l_f is the free part of the rod, see Fig. 2. The total axial stiffness in the rod direction K_{ax} is obtained by:

$$K_{ax} = \frac{K_w \cdot K_{ax,f}}{K_w + K_{ax,f}} \tag{14}$$

Lateral stiffness

To the authors' knowledge, there are no studies dealing with the lateral stiffness of long threaded rods. Eurocode 5 (CEN 2004) provides only a general relation for determining the total slip of a steel-to-timber joint with dowels, bolts, screws or nails, as $K_{ser} = 2 \cdot \rho_m^{1.5} \cdot d / 23$ (per shear plane and fastener).

It is here proposed to estimate the lateral stiffness of long threaded rods by considering the rod as a semi-infinite beam supported on an elastic foundation, similar to studies dealing with the application of self-tapping screws as shear connectors in timber-to-concrete joints (Moshiri et al. 2014; Symons et al. 2010). The main advantage of the proposed method is a straightforward analytical determination of the lateral stiffness for different boundary conditions imposed at the end of the rod.

The differential equation for the deflection curve of a beam supported on elastic foundation is:

$$EI\frac{d^4v}{dx^4} = -k \cdot v \tag{15}$$

where k is the foundation stiffness (N/mm^2) and EI represents the flexural stiffness of the beam. By introducing a parameter $\lambda = \sqrt[4]{k/(4EI)}$ and solving the differential equation with boundary conditions corresponding to the arrangement shown in Fig. 3 (the rod-end is loaded by a force P_0 and a moment M_0), the lateral displacement v_0 and rotation θ_0 at the rod-end become (Hetényi 1946):

$$\begin{aligned} v_0 &= \frac{2P_0 \cdot \lambda}{k} + \frac{2M_0 \cdot \lambda^2}{k} \\ \theta_0 &= \frac{2P_0 \cdot \lambda^2}{k} + \frac{4M_0 \cdot \lambda^3}{k} \end{aligned} \tag{16}$$

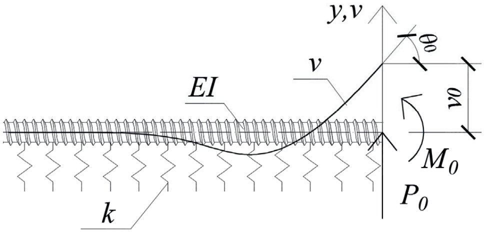

Fig. 3 Laterally loaded threaded rod considered as a semi-infinite beam on an elastic foundation

The lateral stiffness of the threaded rod K_v, in accordance with the configuration shown in Fig. 2a, can readily be obtained by inserting Eq. (16) with $M_0 = 0$ into a common force-displacement relation, and defining the flexural stiffness of rods as $EI = E_s \cdot \pi \cdot d_1^4 / 64$, giving:

$$K_v = \frac{k}{2\lambda} = \frac{d_1}{4}\sqrt[4]{\pi \cdot E_s \cdot k^3} \tag{17}$$

where d_1 is the root diameter of the threaded rods, E_s is the elastic modulus of steel and k is the foundation modulus of timber. The modulus k is obtained in correspondence with Eq.(21) by a simple interaction of foundation moduli of timber longitudinal to the grain, k_l, and transverse to the grain, k_t, as:

$$k = \frac{k_l \cdot k_t}{k_l \cdot \cos^2(\gamma) + k_t \cdot \sin^2(\gamma)} \tag{18}$$

Note that in this simplification, the rod is approximated as semi-infinite.

Modification of the lateral stiffness for various boundary conditions

The application of long threaded rods in moment resisting connections implies different boundary conditions at the rod-ends, as shown in Fig. 2. If the rods are fastened to steel connectors at a distance from the timber face (see Fig. 1), the total displacement at the end of the rods is the result of the deformations of the rod part embedded in timber and the free part of the rod. The lateral stiffnesses at the rod-end associated with the boundary conditions shown in Fig. 2 are given in the following, and the derivation of the relations can be found in Appendix A (Online resource).

The lateral stiffness corresponding to the configuration illustrated in Fig. 2c (representing the boundary conditions in the experimental set-up, see Section 2.2) is found by:

$$K_v = \frac{3kEI}{6EI\left(2l_e^2\lambda^3 + 2l_e\lambda^2 + \lambda\right) + kl_f\left(l_f^2 - 3l_f l_e + 3l_e^2\right)} \tag{19}$$

The lateral stiffness corresponding to the case illustrated in Fig. 2b can simply be obtained by Eq. (19) for $l_e = l_f$.

If the rotation at the end of the rod is restrained (Fig. 2d), the lateral stiffness is obtained by:

$$K_v = \frac{12kEI\left(4EI\lambda^3 + kl_f\right)}{48\left(EI\right)^2\lambda^4 + 8kEI\lambda l_f\left(2l_f^2\lambda^2 + 3l_f\lambda + 3\right) + k^2 l_f^4} \tag{20}$$

Resultant stiffness in the load direction

The respective stiffnesses in the axial K_{ax} and lateral direction K_v are associated with the coordinate system of the rod $x - y$, see Fig. 2a. The resultant stiffness in the load direction is found by a transformation of the rod coordinate system into a coordinate system associated with loading, $\bar{x} - \bar{y}$, by applying a rotation ψ. The force-displacement relation in the rod coordinate system $x - y$, $\mathbf{F} = \mathbf{K} \cdot \boldsymbol{\delta}$, is transformed to the coordinate system $\bar{x} - \bar{y}$ by use of rotation tensor **Q,** such that $\bar{\mathbf{K}} = \mathbf{Q} \cdot \mathbf{K} \cdot \mathbf{Q}^T$, $\bar{\mathbf{F}} = \mathbf{Q} \cdot \mathbf{F}$ and $\bar{\boldsymbol{\delta}} = \mathbf{Q} \cdot \boldsymbol{\delta}$. The set of equations $\bar{\mathbf{F}} = \bar{\mathbf{K}} \cdot \bar{\boldsymbol{\delta}}$ is solved for the displacement along $\bar{x}$, $\bar{\delta}_x$, and the stiffness in the load direction is found by $K = F / \bar{\delta}_x$ as:

$$K = \frac{K_{ax} \cdot K_v}{K_{ax} \cdot \sin^2(\psi) + K_v \cdot \cos^2(\psi)} \tag{21}$$

If displacements along $\bar{y}$ are prevented ($\bar{\delta}_y = 0$), the stiffness in the load direction reads:

$$K = K_{ax} \cdot \cos^2(\psi) + K_v \cdot \sin^2(\psi) \tag{22}$$

It can be noted that the relation given in Eq. (21) is a variation of Hankinson's formula, and furthermore that Eq. (22) corresponds to the relation proposed by Tomasi et al. (2010) for stiffness prediction of timber-to-timber lap connections with inclined self-tapping screws.

2.2. Experimental tests

The effects of rod-to-grain angle combined with different load and rod axis directions on capacity and stiffness were investigated experimentally. The experimental tests were carried-out with a pull-beam test configuration. The experimental set-up is shown in Fig. 4. A purpose-made steel coupler was screwed onto the tip of the rods and connected to the load actuator through a bolt, hence forming a hinge allowing free rotation. The bolt location was used as a reference point for the displacement monitoring. The displacement was measured by 4 displacement transducers (LVDT). One pair of LVDTs was oriented vertically (TV), whereas the other pair was oriented horizontally (TH) (in the initial configuration, i.e. before loading). In each pair, the LVDTs were placed at the opposed sides of the timber beam. The mean value of the measurements was used in the evaluation. The vertical LVDTs were attached to the lower face of the beam, whereas the horizontal LVDTs were attached to a fixed point distant to the timber beams. Free rotation at the ends of the LVDTs was provided. The relative displacement in the vertical direction (perpendicular to the grain with reference to the timber beam), which is of interest in the current investigation, can be calculated knowing the distances between the reference points of LVDTs in the initial configuration. In addition, the horizontal displacement of the beam was monitored and was found to be insignificant.

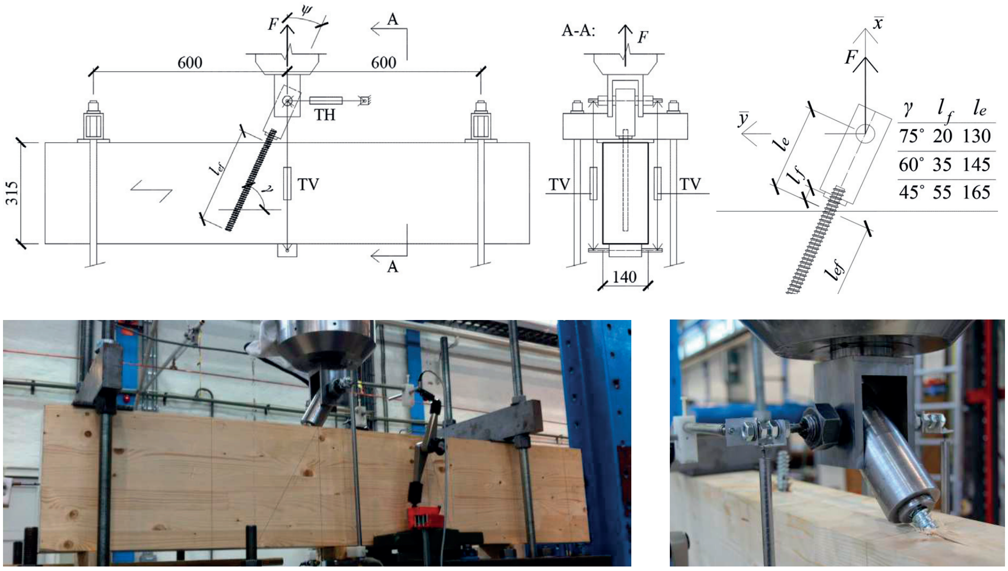

Fig. 4 Experimental set-up

The load was applied in perpendicular to the grain direction with a constant displacement rate of 2 mm/min. The load actuator was fixed through a hinge to a steel frame at a vertical distance of approximately 2.5 m from the timber beam. Since the horizontal displacement of the rod is of the order of tenths of millimeters, the applied force can be assumed acting vertically (the horizontal force component is negligible). Five tests were carried-out for specimens with rod-to-grain angles $\gamma = 60^\circ$ and 75°, and one additional test was performed for $\gamma = 45^\circ$, leading to load-to-rod angles $\psi = 90^\circ - \gamma$.

The timber beams were made of glulam strength class GL30c (CEN 2013) and had 140 mm width and 315 mm height. The beams were fabricated with 45 mm thick lamellas of Norwegian spruce (Picea Abies). The timber specimens were conditioned at the standard environment of 20º C and 65 % relative humidity, resulting in approximately 12 % moisture content.

The threaded rods were of type SFS WB-T-20 (DiBt 2015) complying with DIN 7998 (DIN 1975). The outer diameter of the rods, d, was 20 mm, whereas the inner diameter, d_1, was 15 mm. The strength class was 8.8 according to the manufacturer. The effective (embedment) length of the rods l_{ef} was 300 mm in all tests.

2.3. Numerical model

Numerical simulations were carried out by ABAQUS (DSS 2014). Three models corresponding to the experimental configurations ($\gamma = 45^\circ$, 60° and 75°) were used in order to determine the stiffness in direction of the applied load, see Fig. 5. The coupling steel part between the rod and the load actuator, used in the experiments, has much higher flexural and axial stiffness compared to the rods, and it was therefore omitted in the numerical models. The load was applied in perpendicular to the grain direction through a distant reference point coupled rigidly to the rod-end. In addition, three models with no eccentricity of the load, and the rod-end located at the level of the upper timber face (case (a) in Fig. 2), were used for verification of the proposed analytical model. Out-of-the-plane displacements were prevented at the reference point used for the load application. The timber beams were supported by removing all translational degrees of freedom at the support regions (at locations in correspondence with the experiments).

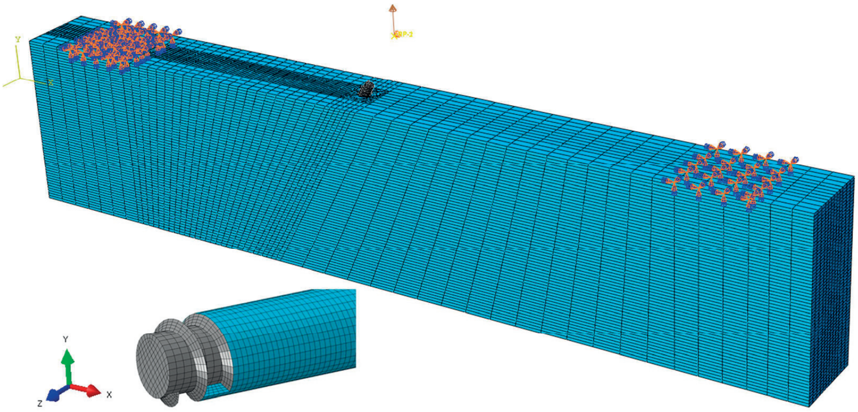

Fig. 5 Numerical model

Eight-node brick elements with reduced integration and hour-glass control (C3D8R) were used in the models. A sensitivity study was carried out in order to determine a satisfactory mesh size. The mesh was denser in the vicinity of the rods. The rod and its interaction with the timber was based on a numerical model presented by Stamatopoulos and Malo (2016). Contact properties between rod and timber utilized a "hard" contact behaviour in the normal direction and isotropic tangential behaviour with a coefficient of friction of 0.2, which was based on the study by Koubek and Dedicova (2014).

Wood was modelled as transversally isotropic with the material properties summarized in Table 1. Here, E is the modulus of elasticity, G is the shear modulus and v is the Poisson's ratio. The longitudinal direction (L) is the grain direction, and no distinction is made between tangential (T) and radial (R) directions. Steel was modelled as isotropic with $E = 210$ GPa and $v = 0.3$.

Table 1 Material properties of wood used in numerical simulations

E_L [MPa] (a)	$E_R=E_T$ [MPa] (a)	$G_{LR}=G_{LT}$ [MPa] (b)	G_{RT} [MPa] (b)	$v_{LR}=v_{LT}$ [-] (b)	v_{TR} [-] (b)
13000	400	600	30	0.6	0.315

(a) Manufacturer: Moelven industrier ASA, class L40 (GL30c)

(b) Norwegian spruce – estimations based on (Dahl 2009)

3. Results and discussion

3.1. Experimental results

The average values of the ultimate force F_u and the stiffness in the load direction K are presented in Table 2.

Table 2 Experimental results in terms of the ultimate force F_u and the stiffness K (COV: coefficient of variation)

γ	No.of tests	F_u		K	
		[kN]	COV	[N/mm]	COV
75°	5	85	0.10	7300	0.09
60°	5	64	0.16	1200	0.13
45°	1	49	-	390	-

Note: $\gamma+\psi = 90°$

The stiffness was obtained by linearization of the initial elastic part of the force-displacement curves shown in Fig. 6. After the initial elastic part, yielding in the steel rods propagates due to bending, characterized by a decreasing stiffness. The rods are increasingly bended causing the end part of the rods to rotate towards the direction of the applied force. This phase is characterized by "opening" of the timber specimens in close proximity to the point where the rods penetrate the timber beams, see Fig. 6. The failure is finally reached due to withdrawal of the rods.

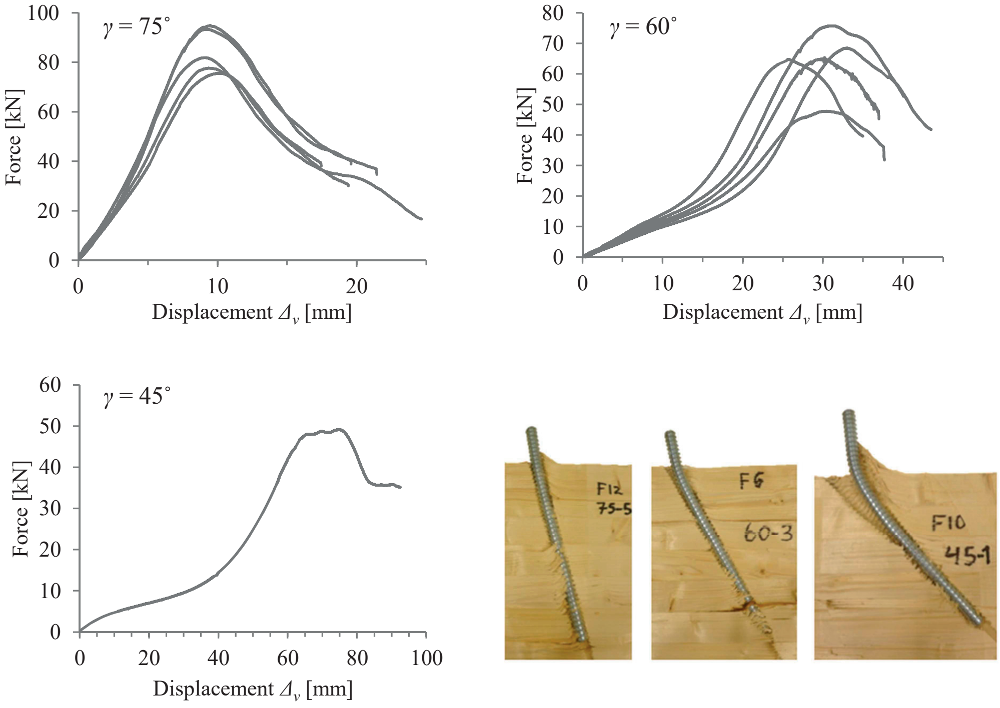

Fig. 6 Experimentally obtained force-displacement curves and examples of cut-opened specimens after testing; Δv is a vertical displacement (in the direction of the applied force). Note: $\gamma+\psi = 90°$

3.2. Theoretically predicted capacity and stiffness compared to experimental results

3.2.1. Capacity

The ultimate force obtained from the experiments is compared with the analytically predicted values. Two different analytical models were used, see Table 3. Model 1 represents the capacity prediction by Eurocode 5 (CEN 2004). Model 2 utilizes the design model for self-tapping screws presented by Jockwer et al. (2014) with two different embedment strengths f_h. In both models, the axial capacity by the producers' technical approval (TA (DiBt 2015)) was used. As shown in Table 4, the axial capacity obtained by use of Eq. (3) (Stamatopoulos and Malo 2015) is very similar to the values obtained by the prediction of TA, resulting in minor variations of the total capacity. It should, however, be kept in mind that the use of TA is not valid for rod-to-grain angles $\gamma < 45°$.

Table 3 Definition of the analytical models used for the capacity prediction

Model	R_{ax}	R_v	f_h	R
M.1	SFS TA Eq.(1)	EC5 Eq.(5)	EC5 Eq.(9)	EC5 Eq.(11)
M.2a	SFS TA [(a)] Eq.(1)	Jockwer et al. Eq.(6)	Blaß et al. Eq.(8)	Jockwer et al. Eq.(12)
M.2b	SFS TA [(a)] Eq.(1)	Jockwer et al. Eq.(6)	EC5 Eq.(9)	Jockwer et al. Eq.(12)

[(a)] with l_{ef} reduced by x_1

The results obtained by the analytical models and the experiments are summarized in Table 4. Mean values of the input parameters were used in the calculations in order to obtain the capacity mean values. The mean value of $f_{v,roll,m}$ was obtained by modifying the characteristic strength for glulam of $f_{v,roll,k} = 1.2$ MPa (CEN 2013) by COV = 0.15, which was taken from (JCSS 2006). The mean value of $f_{u,m}$ was obtained from test results by Stamatopoulos and Malo (2015), for which the mean tensile strength of the threaded rods was found to be 176 kN (d_{ef} was used in the calculations). The mean density of timber ρ_m is declared by the producer of the glulam specimens. The value corresponds well to experiments carried out earlier with the same glulam class (Cepelka and Malo 2016).

Table 4 Comparison of mean capacity obtained by the analytical models and the experiments

γ	$R_{ax,m}$ [kN]		$R_{v,m}$ [kN]			R_m, F_u [kN]			
	Eq.(3)	Eq.(1)	M.1	M.2a	M.2b	M.1	M.2a	M.2b	Exp.(F_u)
90°	89.6	92.8	41.1	15.5	20.5	92.8	92.8	92.8	97 [(a)]
75°	89.1	92.8	40.3	9.6	7.7	81.7	85.0	78.4	85
60°	87.5	92.8	38.3	7.0	4.4	62.3	72.8	59.5	64
45°	85.3	92.8	36.1	5.5	2.9	47.5	57.3	38.8	49

[(a)] Mean experimental capacity taken from (Stamatopoulos and Malo 2015)

Input to the anal. models: $\rho_m = 470$ kg/m^3, $E_s = 210$ GPa, $f_{v,roll,m} = 1.55$ MPa, $f_{u,m} = 905$ MPa, $l_{ef} = 300$ mm, $d_1 = 15$ mm, $d = 20$ mm

Note: $\gamma + \psi = 90°$

The graphical visualization of the results in Fig. 7 (left) shows clearly that both design models yield good estimates of the ultimate force. For the design model of Jockwer et al. (2014), it seems to be more appropriate to use embedment strengths f_h based on Eurocode 5. The effect of the rod inclination on the capacity as obtained by the experiments is shown in Fig. 7 (right). The rod-to-grain angle $\gamma = 45^\circ$ leading to load-to-rod angle $\psi = 45^\circ$ results in approximately 50 % reduction of the capacity compared to the capacity under pure axial loading normal grain $F_{u,90}$.

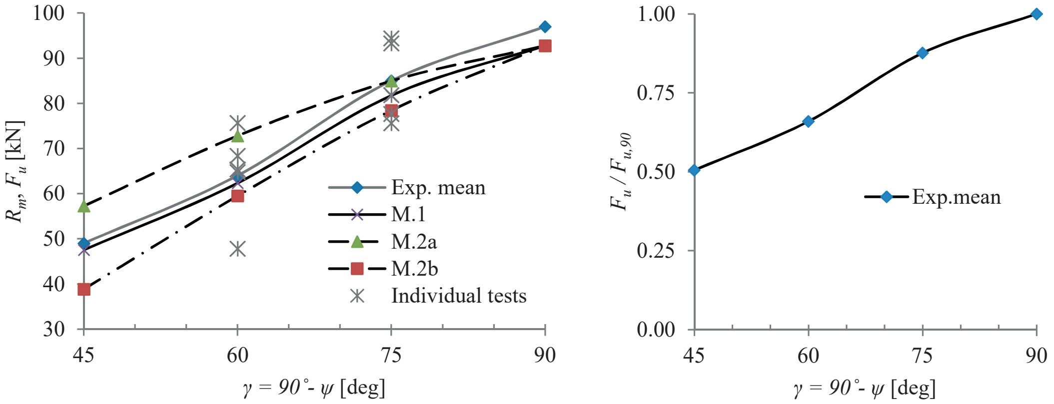

Fig. 7 Left: Comparison of capacity obtained by the analytical models and the experiments, Right: Effect of the rod-to-grain angle γ and load-to-rod angle $\psi = 90^\circ - \gamma$ on the capacity

3.2.2. Stiffness

Summary of mean experimental, analytical and numerical results of the stiffness in the load direction is presented in Table 5. Two different boundary conditions are analysed herein. The first set of results, $K^{(c)}$, is associated with the configuration used in the experiments (Fig. 2c). The second set, $K^{(a)}$, is associated with a basic configuration, for which the load is acting with no eccentricity from the timber member (Fig. 2a). The analytical prediction of $K^{(c)}$ was obtained by use of set of Eqs. (14), (19) and (21), while for the prediction of $K^{(a)}$, Eqs. (13), (17) and (21) were used. The values of $K^{(a)}$ obtained by the proposed analytical and numerical models are furthermore compared to the model by Jockwer et al. (2014). For joints with inclined self-tapping screws, Jockwer et al. (2014) proposed to determine the stiffness in the load direction (for load acting perpendicular to the grain) as an effective stiffness of springs in series: $K_{90} = K_{ax} \cdot K_{v,pulling} / (K_{ax} + K_{v,pulling})$, where $K_{v,pulling} = 3 \cdot E_s \cdot \pi \cdot d_1^4 / (64 \cdot x_1^3)$ represents the lateral stiffness (x_1 is obtained by Eq. (7)), while K_{ax} represents the axial withdrawal stiffness of the screw.

Table 5 Comparison of mean stiffness obtained by experiments, analytical and numerical models

γ	$K^{(c)}$ - test config. [N/mm]			$K^{(a)}$ - no eccentricity [N/mm]		
	Exp.	Anal.	Num.	Anal.	Num.	Anal. [(1)]
75°	7300	6600	7300	76800	72700	51500
60°	1200	1300	1200	50150	46000	18300
45°	390	430	440	30600	26600	8200

[(1)] Model by Jockwer et al. (2014)

Input to the anal. models: $\rho_m = 470$ kg/m^3, $E_s = 210$ GPa, $f_{v,roll,m} = 1.55$ MPa, $d = 20$ mm, $d_1 = 15$ mm, $l_{ef} = 300$ mm, $k_t = 710$ MPa, $k_l = 1300$ MPa, l_f and l_e see Fig. 4

Note: $\gamma + \psi = 90^\circ$

The mean values of input parameters were used in order to obtain the mean stiffness. The foundation moduli transverse (k_t) and longitudinal (k_l) to the grain were taken as the average of experimental results for spruce and steel dowels (diameter 16 mm) from investigations by Gattesco (1998) and Gattesco and Toffolo (2004). The remaining input parameters are discussed in Section 3.2.1.

The values of the stiffness $K^{(c)}$ obtained by the proposed analytical model show good agreement with the experimental results, confer Table 5. The numerical models predict very well the stiffness $K^{(c)}$ compared to the experimental results, and can thus be used as a validation for the analytically obtained $K^{(a)}$. Good agreement between numerical simulations and the results obtained from the proposed model is here achieved, while the model proposed by Jockwer et al. (2014) gives too low stiffness as shown graphically in Fig. 8 (left). Embedment strength f_h according to Blaß et al. (2006) was used in the analytical prediction by Jockwer et al. (2014). The use of f_h according to Eurocode 5 yields even lower values of the predicted stiffness.

Fig. 8 (right) shows the effect of the rod inclination relative to the grain and loading direction on the stiffness $K^{(a)}$ obtained by the proposed analytical model. The rod-to-grain angle $\gamma = 45^\circ$ leading to load-to-rod angle $\psi = 45^\circ$ results in approximately 70 % reduction of the stiffness compared to pure withdrawal stiffness normal grain $K_{w,90}$.

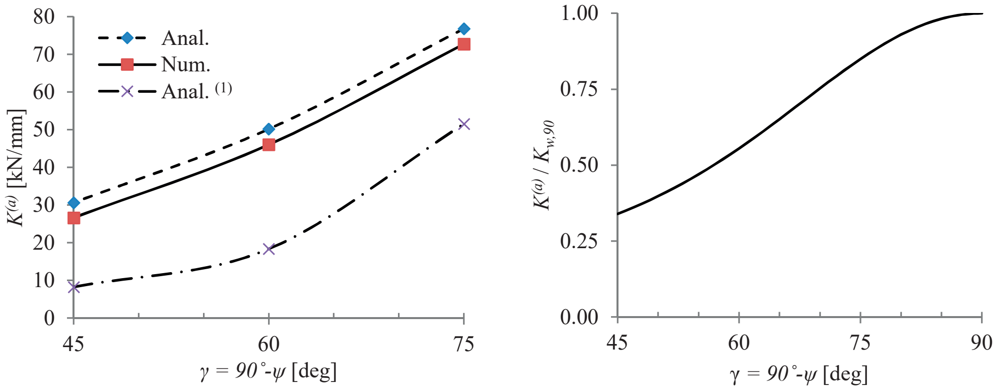

Fig. 8 Left: Comparison of stiffness $K^{(a)}$ obtained by numerical and analytical models, Right: Relation $K^{(a)}/K_{w,90}$ obtained by the proposed analytical model; (1) Model by Jockwer et al. (2014)

The influence of the boundary conditions and the extent of the free length of rod not embedded in timber l_f are studied in Fig. 9. The stiffness corresponding to the boundary conditions illustrated in Fig. 2b, $K^{(b)}$, was calculated with varying free lengths of rod l_f = 0, 10, 20, 30 and 40 mm. The comparison of $K^{(b)}$ with pure axial withdrawal stiffness normal grain is shown in Fig. 9 (left) as ratios $K^{(b)}/K_{w,90}$. Similarly, Fig. 9 (middle) shows the ratios of $K^{(d)}/K_{w,90}$, where $K^{(d)}$ is the stiffness corresponding to the boundary conditions illustrated in Fig. 2d. The comparison of Fig. 9 (left) and (middle) illustrates the significant effect of the rotational restraint at the end of the rod (case (d)). A considerably better performance, in terms of stiffness, can be achieved by restraining the displacement at the end of the rod, transversally to the loading (stiffness obtained by Eq. (22)), as demonstrated in Fig. 9 (right). It can moreover be noticed that, in such a configuration, the effect of the rotational restraint nearly vanishes.

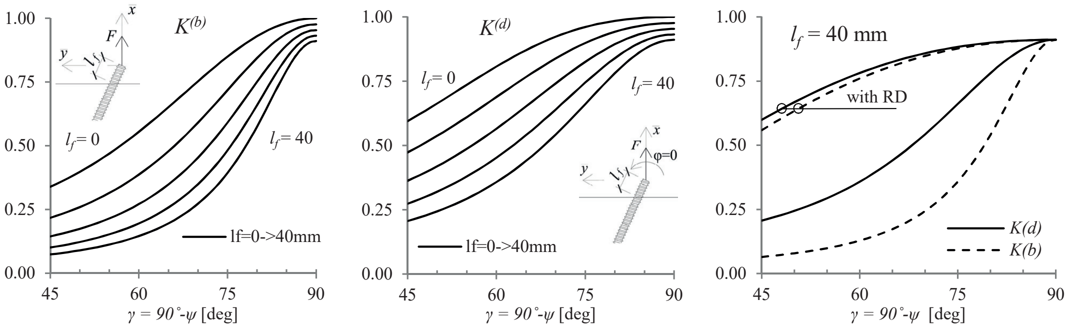

Fig. 9 Influence of boundary conditions and length l_f on the stiffness: Left: $K^{(b)}/K_{w,90}$, Middle: $K^{(d)}/K_{w,90}$, Right: effect of the restrained displacement (RD) at the rod-end transversally to the loading

4. Concluding remarks

The effect of rod-to-grain and load-to-rod angles on capacity and stiffness of axially and laterally loaded long threaded rods used as connectors in timber joints was investigated by use of experiments and numerical models. Analytical relations are proposed for determining the capacity and the stiffness. The main findings are summarized in the following:

- Both capacity and stiffness of the threaded rods are significantly reduced by the increased rod-to-grain and load-to-rod angles. The rod-to-grain angle of 45°, leading to load-to-rod angle of 45° in the current investigation, resulted in approximately 50 % reduction of the capacity and 70 % reduction of the stiffness compared to pure axial loading normal grain.
- Analytical prediction of capacity can be carried out by use of relations in Eurocode 5 (CEN 2004) or the model proposed by Jockwer et al. (2014) for connections with inclined screws. Both models yield good estimation of the ultimate load for varying rod-to-grain angle compared to the experimental results.
- An analytical model for predicting the stiffness is proposed and validated by experimental results and finite element simulations. The model can readily be modified for different boundary conditions at the rod-ends. Analytical relations are derived, associated with four different boundary conditions applicable for joints.
- In timber joints with threaded rods fastened to steel couplers, an increased stiffness of the rods can be obtained by restraining the rotation at the rod-ends. Significant increase of stiffness is achieved providing support at the rod-end transversally to the load direction (e.g. by anchoring the steel couplers to the timber member).

Acknowledgment

This work was funded by the WoodWisdom-Net+ project DuraTB ("Durable Timber Bridges") and the support from the funding bodies and partners is gratefully acknowledged. The authors would also like to acknowledge Halvor Grytting and Eirik Dimmen Sæle for their important contributions and good experimental work.

References

Bejtka I, Blaß HJ Joints with inclined screws. In: CIB W18-Meeting 35, Kyoto, Japan, 2002. pp Paper 7-5

Blaß HJ, Bejtka I, Uibel T (2006) Tragfähigkeit von Verbindungen mit selbst bohrenden Holzschrauben mit Vollgewinde (Load capacity of connections with self-drilling wood screws with full thread). Universität Karlsruhe, Karlsruhe: KIT Scientific Publishing

Blaß HJ, Krüger O (2010) Schubverstärkung von Holz mit Holzschrauben und Gewindestangen (Shear reinforcement of wood with wood screws and threaded rods). Universität Karlsruhe, Karlsruhe: KIT Scientific Publishing

CEN (2004) EN 1995-1-1:2004: Design of timber structures. Part 1-1: General-Common rules and rules for buildings. European committee for standarization, Brussels

CEN (2013) EN 14080:2013: Timber structures-Glued laminated timber and glued solid timber - Requirements. European Committee for Standardization,

Cepelka M, Malo KA (2016) Experimental study of end grain effects in timber joints under uniaxial compression load. Paper presented at the Proceedings of the World Conference on Timber Engineering (WCTE 2016), August 22-25, 2016, Vienna, Austria,

Dahl KB (2009) Mechanical properties of clear wood from Norway spruce. Dissertation. Norwegian University of Science and Technology

DiBt (2015) Allgemeine bauaufsichtliche Zulassung - Z-9.1-777 - Gewindestangen mit Holzgewinde als Holzverbindungsmittel (General building approval - Z-9.1-777 - Threaded rods with wood threads as wood connectors). Deutches Institut für Bautechnik, Berlin

DIN (1975) DIN 7998: Gewinde und Schraubenenden für Holzschrauben (Threads and screws for wood). Deutsches Institut für Normung, Berlin

DSS DSSC (2014) Abaqus analysis user's guide, Version 6.14.

Gattesco N (1998) Strength and local deformability of wood beneath bolted connectors. Journal of Structural Engineering 124:195-202

Gattesco N, Toffolo I (2004) Experimental study on multiple-bolt steel-to-timber tension joints. Materials and Structures/Materiaux et Constructions 37:129-138

Hetényi M (1946) Beams on elastic foundation: Theory with applications in the fields of civil and mechanical engineering. The University of Michigan Press, Baltimore

JCSS (2006) JCSS Probabilistic model code, Part 3: Resistance models, 3.05: Timber

Jensen JL, Koizumi A, Sasaki T, Tamura Y, Iijima Y (2001) Axially loaded glued-in hardwood dowels. Wood Science and Technology 35:73-83 doi:10.1007/s002260000076

Jockwer R, Steiger R, Frangi A (2014) Fully Threaded Self-tapping Screws Subjected to Combined Axial and Lateral Loading with Different Load to Grain Angles vol 9. doi:10.1007/978-94-007-7811-5_25

Johansen KW (1949) Theory of timber connectors. International Association of Bridges and Structural Engineering Publication No.9:249-262

Koubek R, Dedicova K (2014) Friction of wood on steel. Linnaeus University

Malo KA, Abrahamsen RB, Bjertnæs MA (2016) Some structural design issues of the 14-storey timber framed building "Treet" in Norway. European Journal of Wood and Wood Products 74:407-424 doi:10.1007/s00107-016-1022-5

Malo KA, Stamatopoulos H (2016) Connections with threaded rods in moment resisting frames. Paper presented at the Proceedings of the World Conference on Timber Engineering (WCTE 2016), August 22-25, 2016, Vienna, Austria,

Moshiri F, Shrestha R, Crews K (2014) The Predictive Model for Stiffness of Inclined Screws as Shear Connection in Timber-Concrete Composite Floor vol 9. doi:10.1007/978-94-007-7811-5_40

Stamatopoulos H (2016) Withdrawal properties of threaded rods embedded in glued-laminated timber elements. Dissertation. NTNU, Norwegian University of Science and Technology

Stamatopoulos H, Malo KA (2015) Withdrawal capacity of threaded rods embedded in timber elements. Construction and Building Materials 94:387-397 doi:http://dx.doi.org/10.1016/j.conbuildmat.2015.07.067

Stamatopoulos H, Malo KA (2016) Withdrawal stiffness of threaded rods embedded in timber elements. Construction and Building Materials 116:263-272 doi:http://dx.doi.org/10.1016/j.conbuildmat.2016.04.144

Symons D, Persaud R, Stanislaus H (2010) Slip modulus of inclined screws in timber-concrete floors. Proceedings of the Institution of Civil Engineers: Structures and Buildings 163:245-255 doi:10.1680/stbu.2010.163.4.245

Tomasi R, Crosatti A, Piazza M (2010) Theoretical and experimental analysis of timber-to-timber joints connected with inclined screws. Construction and Building Materials 24:1560-1571 doi:http://dx.doi.org/10.1016/j.conbuildmat.2010.03.007

Volkersen O (1938) Die nietkraftverteilung in zugbeanspruchten nietverbindungen mit konstanten laschenquerschnitten (The rivet-force distribution in tension-stressed rivet joints with constant adherends thickness). Luftfahrtforschung 15

APPENDIX A

Effect of rod-to-grain angle on capacity and stiffness of axially and laterally loaded long threaded rods in timber joints

Martin Cepelka[1*], Kjell Arne Malo[1], Haris Stamatopoulos [1]

[1] Department of Structural Engineering, Norwegian University of Science and Technology (NTNU), Rich. Birkelandsvei 1A, 7491, Trondheim, Norway

[*] corresponding author, martin.cepelka@ntnu.no , +4795409031

A1. Derivation of relations for predicting lateral stiffness of long threaded rods with various boundary conditions at the rod-ends

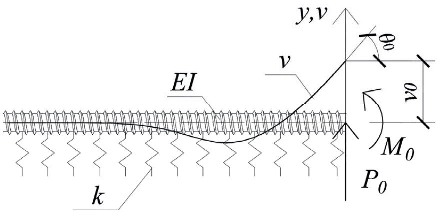

Fig. A.1 Laterally loaded threaded rod considered as a semi-infinite beam on an elastic foundation

The fundamental relations for the lateral displacement v_0 and rotation θ_0, at the point where the rod penetrates the timber, were obtained by solving the differential equation associated with the model of a threaded rod considered as a semi-infinite beam supported on an elastic foundation as:

$$v_0 = \frac{2P_0 \cdot \lambda}{k} + \frac{2M_0 \cdot \lambda^2}{k} \tag{A.1}$$

$$\theta_0 = \frac{2P_0 \cdot \lambda^2}{k} + \frac{4M_0 \cdot \lambda^3}{k} \tag{A.2}$$

A1.1. Lateral stiffness of rod loaded eccentric to the timber face

The total lateral displacement at point *1* (see Fig. A.2), v_1, consists of 3 contributions:

$$v_1 = v_0 + v_\theta + v_b \tag{A.3}$$

The lateral force P acts at a distance l_e from a point where the rod penetrates the timber (denoted as *0* in Fig. A.2), causing a moment M_0:

$$M_0 = P \cdot l_e \tag{A.4}$$

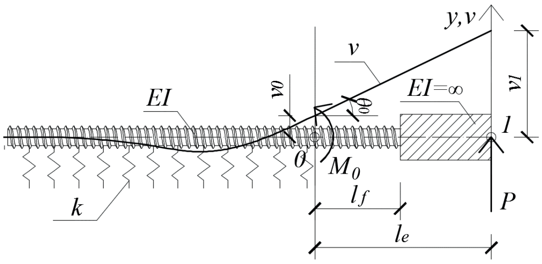

Fig. A.2 Threaded rod loaded eccentric to the timber face

The displacement at point *0*, v_0, is obtained by inserting Eq.(A.4) into Eq.(A.1), giving:

$$v_0 = \frac{2P \cdot \lambda}{k} + \frac{2P \cdot l_e \cdot \lambda^2}{k} \tag{A.5}$$

The displacement at point *1*, due to rotation at point *0*, is obtained by use of Eqs.(A.2) and (A.4):

$$v_\theta = \theta_0 \cdot l_e = \left(\frac{2P \cdot \lambda^2}{k} + \frac{4P \cdot l_e \cdot \lambda^3}{k} \right) \cdot l_e \tag{A.6}$$

The displacement at point *1*, due to bending of the free part of the rod, is:

$$v_b = \frac{P \cdot l_f^{\,2}}{6EI}\left(3l_e - l_f\right) + \frac{P \cdot \left(l_e - l_f\right) \cdot l_f}{2EI}\left(2l_e - l_f\right) \tag{A.7}$$

The lateral stiffness at point *1* is finally obtained by $K_v = P / v_1$:

$$K_v = \frac{3kEI}{6EI\left(2l_e^2\lambda^3 + 2l_e\lambda^2 + \lambda\right) + kl_f\left(l_f^2 - 3l_f l_e + 3l_e^2\right)} \tag{A.8}$$

A1.2. Lateral stiffness of rod loaded eccentric to the timber with restrained rotation at the rod-end

The total lateral displacement at point *1* (see Fig. A.3), v_1, consists of 3 contributions:

$$v_1 = v_0 + v_\theta + v_b \tag{A.9}$$

The moment equilibrium at the free part of the rod gives:

$$M_0 = P \cdot l_f - M_1 \tag{A.10}$$

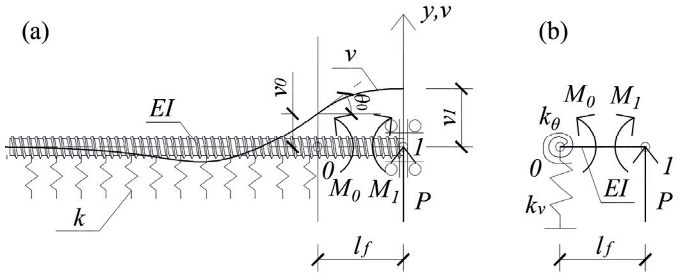

Fig. A.3 Threaded rod loaded eccentric to the timber face with restrained rotation at the rod-end (a), analytical model utilized in conjunction with application of principle of virtual work (b)

The moment at point *0*, determined by use of a principle of virtual work applied to the configuration shown in in Fig. A.3b is:

$$M_0 = \frac{P \cdot l_f^2 \cdot k_\theta}{2k_\theta \cdot l_f + 2EI} \tag{A.11}$$

Since $\theta_0 = M_0 / k_\theta$, the rotational stiffness at point *0*, k_θ, is found by inserting Eq.(A.11) into Eq.(A.2), giving:

$$k_\theta = \frac{k \cdot l_f^2 - 4EI \cdot \lambda^2}{4l_f \cdot \lambda^2 \left(l_f \cdot \lambda + 1\right)} \tag{A.12}$$

The displacement at point *0*, v_0, is obtained by inserting Eqs.(A.11) and (A.12) into Eq.(A.1), giving:

$$v_0 = \frac{P \cdot \lambda \left(4EI \cdot \lambda^3 + k\left(\lambda \cdot l_f^2 + 2l_f\right)\right)}{k\left(4EI \cdot \lambda^3 + k \cdot l_f\right)} \tag{A.13}$$

The displacement at point *1*, due to rotation at point *0*, is obtained by use of Eqs.(A.2) , (A.11) and (A.12) :

$$v_\theta = \theta_0 \cdot l_f = \frac{2P \cdot \lambda^2 \cdot l_f^2 \left(\lambda \cdot l_f + 1\right)}{4EI \cdot \lambda^3 + k \cdot l_f} \tag{A.14}$$

The displacement at point *1*, due to bending of the free part of the rod, was found by principle of virtual work applied to the configuration shown in Fig. A.3b (M_1 is obtained by use Eq.(A.10)):

$$v_b = \frac{1}{EI}\left(\frac{P \cdot l_f^{\,3}}{3} - \frac{M_1 \cdot l_f^{\,2}}{2}\right) \tag{A.15}$$

The lateral stiffness at point *1* is finally obtained by $K_v = P / v_1$:

$$K_v = \frac{12kEI\left(4EI\lambda^3 + kl_f\right)}{48\left(EI\right)^2 \lambda^4 + 8kEI\lambda l_f \left(2l_f^2\lambda^2 + 3l_f\lambda + 3\right) + k^2 l_f^4} \tag{A.16}$$

Paper iii

Moment resisting on-site splice of large glulam elements by use of mechanically coupled long threaded rods

Martin Cepelka, Kjell Arne Malo

Under review in an international scientific journal (2017)

Moment resisting on-site splice of large glulam elements by use of mechanically coupled long threaded rods

Martin Cepelka[1*], Kjell Arne Malo[1**]

[1] Department of Structural Engineering, Norwegian University of Science and Technology (NTNU), Rich. Birkelandsvei 1A, 7491, Trondheim, Norway

[*] corresponding author, martin.cepelka@ntnu.no, +4795409031

[**] kjell.malo@ntnu.no

Abstract

Large spans of modern timber bridges can be achieved by use of glulam arches with network hanger configuration. Since transportation and production limit the length of timber elements, the glulam arches must be spliced on bridge site. However, it is difficult to obtain practical moment resisting on-site splicing of massive glulam elements featuring flexural rigidity by the available timber splicing techniques. Consequently, the arches are often designed as trusses containing a large number of connections, which are costly and present a risk of decay development. In the present paper, a novel splicing technique suitable for large massive timber sections is presented. The flexural rigidity of the joint is obtained by the utilisation of long threaded rods having large withdrawal stiffness. Fast and easy on-site assembly is facilitated by mechanical coupling of the rods. The rods are oriented with a small inclination to grain, which prevents potential development of shrinkage cracks along the rods. Experimental and numerical methods were used to investigate the flexural joint characteristics. The joint prototypes featured large rotational stiffness without initial slip. As a basis for practical joint design, analytical relations are proposed for estimating the rotational stiffness, the moment capacity and the capacity under combined bending and normal force.

Keywords: long threaded rod, timber splice joint, glulam, 3D finite element model, rotational stiffness, moment capacity

1. Introduction

Feasibility studies of glulam arch bridges with network hanger configuration have shown excellent structural properties for bridges with massive glulam arches spanning up to 100-120 m [1, 2]. Since the timber arches cannot be produced and transported in one piece, the timber elements must be spliced on bridge site. In order to maintain the stability of the arches, it is crucial to incorporate flexural rigidity in the splice connections [3-5].

Figure 1 shows the recently erected network arch bridge Steibrua in Norway [6]. With a span of 88 m, the bridge is currently the longest single-span timber road bridge in the world. However, due to the lack of rotationally stiff splicing solution for large timber elements, the arches of Steibrua are formed as hybrid timber-steel trusses. This is probably not the most optimal solution since the trusses contain a large number of connections, which are expensive and vulnerable to decay developments. A more durable and cheaper solution could be achieved by the use of massive glulam arches, necessitating on-site splice joints with sufficient rotational stiffness.

Figure 1: Steibrua, Norway – Network arch bridge with glulam arches [6].

Large rotational stiffness and moment capacity of spliced timber beams was achieved by use of commonly available long threaded rods (SFS WB-T-20) in [7]. The rods were inserted parallel to the grain in the opposed parts of timber beams, and the mutual splicing of the rods was carried out by grout-filled steel couplers (similar to systems used for reinforced pre-cast concrete). The parallel to grain orientation of the threaded rods enables effective force transfer in the axial direction and allows the utilisation of the high withdrawal stiffness of rods parallel to the grain. On the other hand, the development of shrinkage cracks (in the grain direction) in close proximity to the threaded rods can lead to loss of capacity. In addition, the gluing operation on site implies quality control issues, and curing of the glue affects the final setting time of the joint.

In this paper, a novel splicing solution is presented, which overcomes the aforementioned shortcomings by the use of slightly inclined long threaded rods with a metric threaded part at one end. A principle layout of the joint is shown in Figure 2. Inserting the rods with a small inclination to the grain avoids the risk of failure due to the occurrence of shrinkage cracks since the rods cross several "layers" of wood. The mechanical joint of the rods allows easy and fast on-site mounting without the need of special tools. In order to transmit the normal force acting in the arch, mutual contact of the mating timber end faces is assured by tightening the rods in the couplers. The shear force can be transmitted through shear keys. A reliable prediction of the structural properties and ductile behaviour is achieved by design provisions enforcing a failure mode driven by yielding of the steel rods.

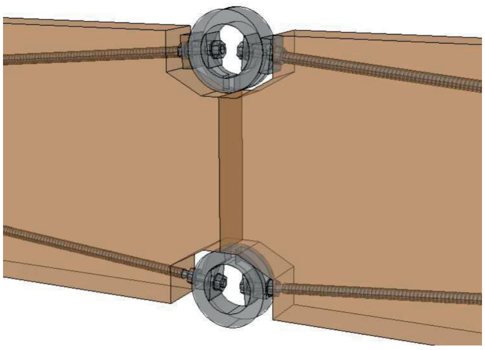

Figure 2: Principle layout of the splice joint with inclined mechanically coupled long threaded rods.

The key prerequisite regarding splicing of massive glulam arches is a sufficient and predictable rotational stiffness of the splice joints. Full-scale prototype joints and numerical models were herein used to study the flexural behaviour of the proposed joint. Analytical relations for practical design are proposed for the determination of the rotational stiffness, the moment capacity and the combined capacity for bending moment and normal force.

2. Materials and methods

2.1. Analytical prediction of flexural joint characteristics

2.1.1. Rotational stiffness

An analytical model for the determination of the rotational stiffness of a splice joint using long threaded rods inserted parallel to the grain was derived in [7]. However, due to the inclination of the rods in the proposed splicing solution, a lateral force component is present at the rod-ends. A modification of the model accounting for the lateral deformations of the rods is presented in the following, with input parameters specified in the Appendix. The model parameters are shown in Figure 3. Here, h and b are the height and the width of the cross-section respectively, a_0 is the height of wood in compression, a_i is a coordinate along z-axis of the i-th rod row determined from the upper edge of wood in compression (with reference to Figure 3, a_i is negative for the rods in compression), h_t is the height of timber end faces in mutual contact, θ represents the relative rotation of the end timber faces, γ is the rod-to-grain angle, σ_x is the longitudinal compression stress in wood, K_{si} is the stiffness of the i-th rod row, u_i is the horizontal displacement at the i-th rod row, $z_i = a_i - a_0$ is the z-coordinate of the the i-th rod row, and F_i is the force in the i-th rod row found by [7]:

$F_i = K_{si} \cdot u_i = K_{si} \cdot \theta \cdot z_i$.

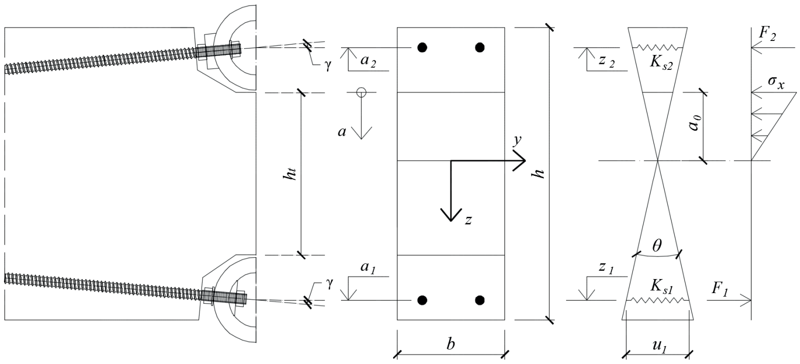

Figure 3: Analytical model nomenclature.

The position of the neutral axis is obtained by requiring no resulting axial force [7]:

$$a_0 = \frac{-\sum_{i=1}^{n} K_{si} + \sqrt{\left(\sum_{i=1}^{n} K_{si}\right)^2 + \frac{E \cdot b}{l_c} \cdot \sum_{i=1}^{n} K_{si} \cdot a_i}}{\frac{E \cdot b}{2 \cdot l_c}} \tag{1}$$

where E is the elastic modulus of timber parallel to the grain, l_c represents an equivalent length of the compression (crushing) zone at the mutual contact of the wooden parts, and n is the number of the rod rows. The rotational stiffness of the connection k_θ is determined by [7]:

$$k_\theta = \sum_{i=1}^{n} K_{si} \cdot z_i^2 + \frac{E \cdot b \cdot a_0^3}{6 \cdot l_c} \tag{2}$$

More information and expressions for the determination of K_{si} and l_c are given in the Appendix.

2.1.2. Moment capacity

The moment capacity of the splice joint, M_u, is estimated under the assumption of elastic distribution of forces until an ultimate force is reached in either of the rods or in the timber (bilinear approximation) by:

$$M_u = \min \left\{ \begin{matrix} F_{u,i} \cdot z_{eq,i} \\ M_{u,t} \end{matrix} \right\} \tag{3}$$

where $M_{u,t}$ is the moment capacity corresponding to the compression strength of timber, $F_{u,i}$ is the ultimate force in the i-th rod row and $z_{eq,i}$ is the equivalent lever arm of the i-th rod row given by:

$$z_{eq,i} = \frac{M}{F_i} = \frac{k_\theta}{K_{si} \cdot z_i} \tag{4}$$

The moment capacity corresponding to the compression strength of timber $M_{u,t}$ (with a linear distribution of compression stresses as illustrated in Figure 3) is determined by:

$$M_{u,t} = \frac{2 \cdot k_\theta \cdot l_c \cdot f_{c,0}}{E \cdot a_0} \tag{5}$$

where $f_{c,0}$ is the timber strength in compression parallel to the grain.

The ultimate force in the i-th rod row, $F_{u,i}$, is obtained by:

$$F_{u,i} = n_r \cdot \cos\gamma \cdot \min\left(R_{axu}, R_u\right) \tag{6}$$

where n_r is the number of the rods in one row, R_{axu} is the ultimate withdrawal strength of the rods and R_u is the tensile strength of the rods. See the Appendix for more details and determination of R_{axu}.

2.1.3. Capacity under combined action of bending moment and normal force

The interaction of bending moment and normal force acting in the splice joint was studied by the use of numerical models. It is proposed to verify the joint capacity by combined quadratic and linear terms in an interaction formula:

$$\left(\frac{N}{N_u}\right)^2 + \frac{M}{M_u} \le 1 \tag{7}$$

where N and M are the normal force and the bending moment acting in the joint, respectively, and N_u and M_u are the capacity in axial compression and bending, respectively.

The ultimate normal force, N_u, is determined assuming a ductile post-elastic behaviour in both the rods and the timber in compression by:

$$N_u = \sum_{i=1}^{n} F_{u,i} + 0.8 \cdot b \cdot h_t \cdot f_{c,0} \tag{8}$$

The factor 0.8 takes into account (in a similar way as design models for reinforced concrete) a non-uniform distribution of compression stresses within the compression zone.

2.2. Experimental tests

2.2.1. Experimental set-up

The prototype beam splices were tested in a four-point bending configuration yielding a pure bending in the splice connection. The experimental set-up and the detailing of the joint are shown in Figure 4 and Figure 5, respectively. The deformation characteristics were obtained by the digital image correlation (DIC) system ARAMIS [8] and subsequent linear regressions of the measured horizontal displacement field for each time step. The measurements by DIC were validated by use of additionally applied transducers. In total, two rotational transducers and five displacement transducers were placed across the end faces of the splice joint. The load was applied according to the loading procedure given in EN 26891:1991 [9].

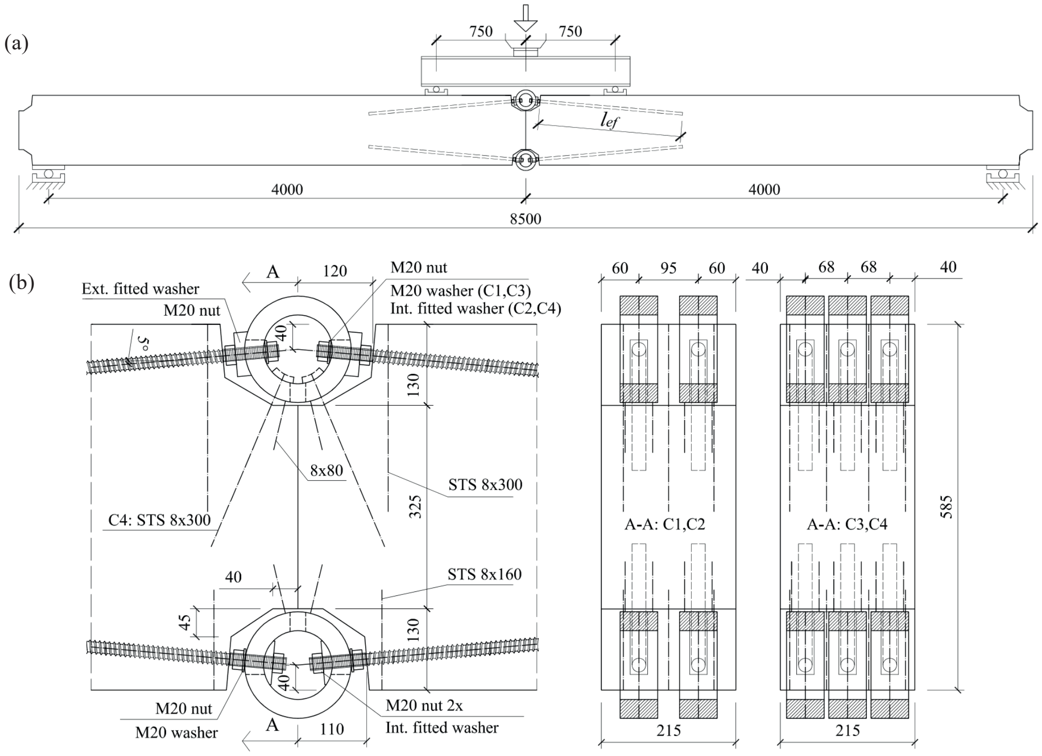

Figure 4: Experimental set-up: (a) the spliced beam, (b) technical specification of the joint. Measures given in mm.

The experimental programme is summarised in Table 1. The purpose of the experiments was to investigate the structural performance for different geometrical configurations, making available validation cases for numerical studies. Therefore, one test for each configuration was performed. Four geometrical configurations were tested, in which number of rods, effective length of rods, l_{ef} (the length of rod screwed in the timber), and detailing in the rod couplers were varied. The threaded rods, inserted in the opposed parts of the beams with a constant rod-to-grain angle of 5 degrees, were connected in the rod couplers. Purpose-made fitted washers were used to distribute the force from the rods onto the surface of the couplers. The detailing at the compression couplers was varied in the different configurations. The configurations C1 and C3 contained, besides the external fitted washers, standard M20 washers at the inner side (see Figure 5c), while in C2 and C4, the fitted internal washers were used (see Figure 5d and Figure 5e). The timber end faces of the spliced parts of the beams were placed in direct mutual contact, and a certain level of pre-stress at the end grains was gained through tightening the nuts.

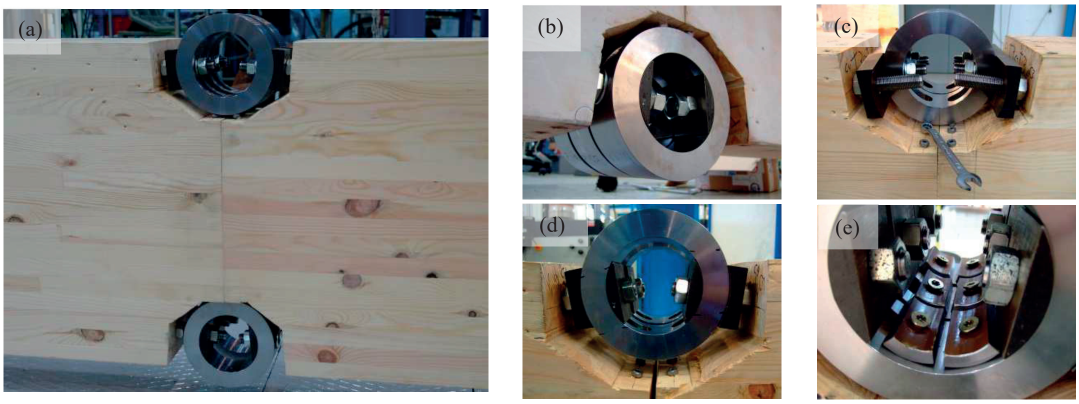

Figure 5: Detailing of the joint: (a) the assembled joint (C1), (b) detail at the tension side (C3). Details at the compression side: (c) C3 under assembly, (d) C2 after testing, (e) C4.

Table 1: Experimental programme

Config.	n_r	l_{ef} [mm]	DA1	DA2	Notation
C1	2	1850	no	no	C1-2-1850-0-0
C2	2	1200	yes	no	C2-2-1200-1-0
C3	3	1200	no	no	C3-3-1200-0-0
C4	3	1000	yes	yes	C4-3-1000-1-1

Design Alternative:
DA1 - Application of internal fitted washers in compression couplers
DA2 - Anchorage of compression couplers

Lateral displacements of the prototype rod couplers at the tension side were prevented by the use of screws inserted in pairs underneath the couplers at each side of the connection. The compression rod couplers were anchored to the timber by self-tapping screws in C4 (see Figure 5e). Perpendicular-to-grain reinforcement was applied by the use of self-tapping screws (STS). Three STS were used in the C1 and C2 configurations, while in the C3 and C4, four STS were used at each side of the timber beams.

2.2.2. Dimensions and materials

The timber beams were made of glulam strength class GL30c [10] and had 215 mm width and 585 mm height. The beams were fabricated with 33 mm thick lamellas of Scots pine. The timber specimens were conditioned at the standard environment of 20º C and 65 % relative humidity, resulting in approximately 12 % moisture content.

The purpose-made threaded rods allow fast mounting using rod couplers. The geometry of the rods is shown in Figure 6, and the average outer and inner diameters were d = 22.4 mm and d_1 = 16.9 mm, respectively. The initial 90 mm long part of the rods was manufactured with an M20 metric threaded part. The declared strength class is 8.8. In order to verify the strength of the rods, three tensile tests of the rods were carried out. The obtained mean capacity was 207.6 kN (COV = 0.01), which corresponds to a mean strength of 925 MPa if the average inner diameter is assumed.

Figure 6: Purpose-made long threaded rods used in the investigation (left) and geometry of the wood thread (right). Measures given in mm.

The rod couplers were manufactured from steel S355. The outer and inner diameters were 170 mm and 110 mm, respectively, and the width was 60 mm. The 28 mm wide slot in the couplers allowed the application of the couplers after the timber parts were brought together. It should be noted that the couplers were generally-suited prototypes designed for the purpose of the experimental investigation. The fitted washers were made of steel S355 and had a width of 60 mm and a height of 70 mm. The thickness was 15 mm at the axis of symmetry.

2.3. Numerical model

Numerical simulations were carried out by ABAQUS [11]. The geometrical layout of the numerical model corresponds to the experimental investigation shown in Figure 5. The splice joint details of the model are shown in Figure 7. Given the symmetry of the problem, only half of the beam was modelled. Transverse displacements of the beam and the rod couplers were prevented. Loading was applied through a displacement rate at the top of the beam, corresponding to the experiments (4-point bending).

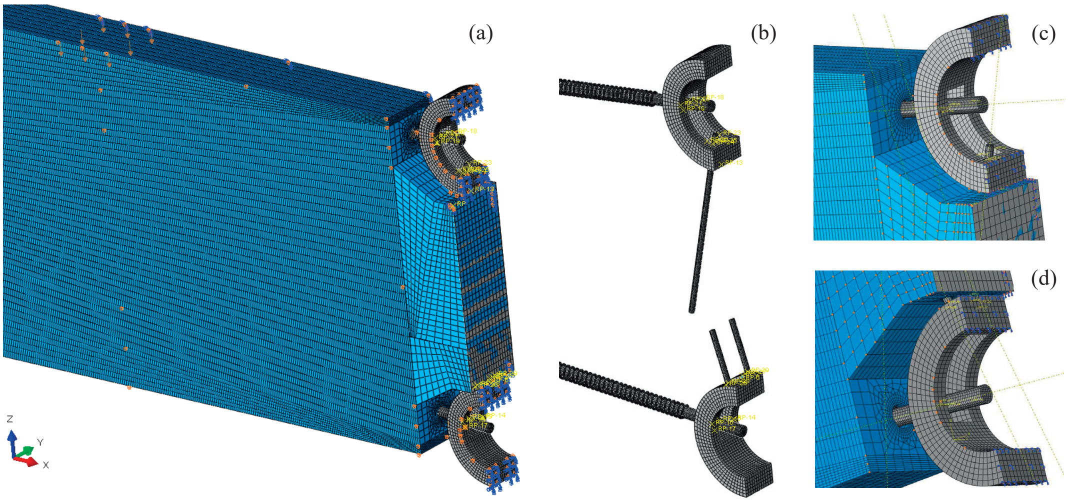

Figure 7: Visualisation of the numerical model: (a) detail at the splice joint, (b) steel parts of the joint, (c) detail at the compression coupler, (d) detail at the tension coupler.

Eight-node brick elements with reduced integration and hour-glass control (C3D8R) were used in the models. A sensitivity study was carried out in order to determine a satisfactory mesh size. The mesh was denser in the zones surrounding the rods.

The threaded rods and their interaction with timber were based on numerical models presented in [7, 12]. The effective length of the rods was 1200 mm, and the inner and the outer diameters of wood threads were 16.9 mm and 22.4 mm, respectively. Contact properties between rods and timber utilised a "hard" contact behaviour in the normal direction and isotropic tangential behaviour with a coefficient of friction of 0.2, which was based on the study in [13]. The anchorage screws of the rod couplers (see Figure 7b) were modelled without threads (by the outer diameter) and with the interaction with the timber realised through a tie-constraint. This simplified approach was shown to be suitable for self-tapping screws in [14].

The relative slip between the rods and the couplers is rigidly constrained for all degrees of freedom, while the relative displacements between the couplers and the anchoring screws are prevented only in the vertical direction (along z-axis with reference to Figure 7). The contact stiffness between the end timber faces at the splice joint was modelled according to [7] by defining a linear elastic contact stiffness at the timber end face of 304 MPa/mm (E_{cr} / l_{cr} = 914 MPa / 3 mm).

Material properties of wood are summarised in Table 2. Here, E is the modulus of elasticity, G is the shear modulus, v is the Poisson's ratio and σ_y represents the yield strength. The longitudinal direction (L) is the grain direction, and no distinction is made between tangential (T) and radial (R) directions.

Table 2: Material properties of wood used in numerical simulations

	[MPa]	[MPa]	[MPa]	[MPa]	[-]	[-]
Elastic	E_L (a)	$E_R=E_T$ (a)	$G_{LR}=G_{LT}$ (b)	G_{RT} (b)	$v_{LR}=v_{LT}$ (b)	v_{TR} (b)
	13000	400	600	30	0.6	0.315
Yield	σ_{yL} (b)	$\sigma_{yR}=\sigma_{yT}$ (b)	$\sigma_{yLR}=\sigma_{yLT}$ (b)	σ_{yRT} (b)		
	23	2.4	3	0.9		

(a) Manufacturer: Moelven industrier ASA, class L40 (GL30c)

(b) Estimations based on [15]

Hill's yield surface [16] was applied to wood together with a linear isotropic hardening and associated flow rule. It should be noted that the material model gives no distinction between positive and negative stresses. No damage coupling was defined in order to describe brittle failure in tension and shear. However, as long as the post-elastic behaviour of the joint is governed by the plastic deformations of the steel parts and crushing of the compression zone of timber, the model provides a suitable description of the joint behaviour also in the non-linear domain. The uniaxial strength parameters were thus chosen to represent the compression stress states, and the hardening was formulated to fit the experimental results in [15] in compression parallel to the grain, such that plastic strains of 0.0035 correspond to the stress level of 33 MPa.

Steel was modelled as isotropic with $E = 210$ GPa and $v = 0.3$. The plastic domain was described by von Mises's yield criterion, linear isotropic hardening and associated flow rule. The yield strength and the hardening formulation of the threaded rods were based on the conducted tensile tests giving the following approximate values of plastic strains at the corresponding stress levels: 0 at 758 MPa and 0.031 at 925 MPa. Corresponding properties for structural steel S355 were used as 0 at 355 MPa and 0.25 at 510 MPa.

3. Results and discussion

3.1. Experimental results

Experimental results of bending tests of the splice connections are presented in terms of moment vs. rotation in the joint, see the plots in Figure 8. The curves are limited either by a rotation of 0.05 rad or by specimen failure. The relative rotations θ were obtained by linear regression of the horizontal displacements, monitored by the digital image correlation (DIC) along vertical sections placed in the vicinity of the slots for the rod couplers. The values obtained by linear regression of DIC results were in good agreement with the rotations measured by the rotational and displacement transducers.

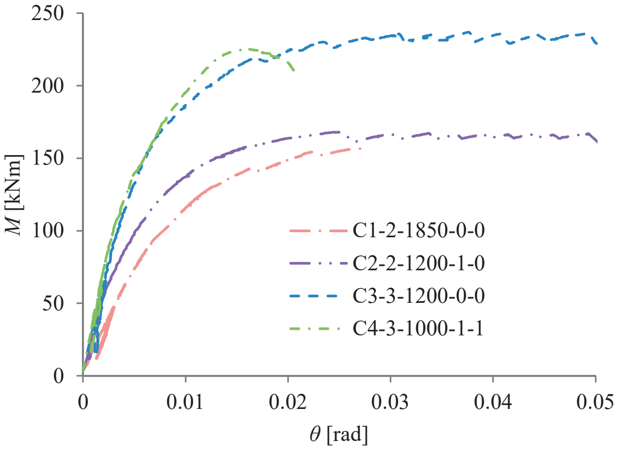

Figure 8: Moment-rotation curves based on data from digital image correlation monitored during bending tests.

The ultimate moment M_u and the elastic rotational stiffness k_θ are presented in Table 3. The splice efficiency with respect to moment capacity, η_M, is the ratio between the measured ultimate moment and the mean theoretical bending capacity of the unspliced timber cross-section. The efficiency with respect to rotational stiffness, η_k, relates the mid-span deflection of an unspliced beam to that of a beam containing a splice connection.

Table 3: Experimental results of bending tests of splice connection

Notation	M_u		k_θ		Failure mode
	[kNm]	η_M ^(a)^	[kNm/rad]	η_k ^(b)^	
C1-2-1850-0-0	161/169	30 %	14863	52 %	Nut/Steel rods
C2-2-1200-1-0	173	30 %	24952	65 %	Steel rods
C3-3-1200-0-0	241	42 %	29167	68 %	Timber compression
C4-3-1000-1-1	230	40 %	35324	72 %	Rods withdrawal

input: GL30c: (a) $f_{m,mean}$ = 41.4 MPa (b) E_{mean} = 13000 MPa, G_{mean} = 650 MPa

The test of C1 initially failed in a brittle manner due to a nut-thread failure. However, the joint was reassembled and by use of two nuts at the tension side, the new test resulted in the ductile tensile failure of the threaded rods. The plot of C1 in Figure 8 represents the first test until the nut-thread failure. The rotational stiffness of C1 is low, compared to C2, which also had 2 rods per row. This is due to the use of standard M20 washers at the connection of the compression rods in the couplers, which did not provide sufficient support in order to prevent rotation of the rod-ends in the couplers. A considerably better rotational stiffness was achieved by the use of fitted internal washers in the compression couplers in the C2 configuration. It was, however, observed that even the use of internal fitted washers did not prevent the outward bending of the compression rods under increasing loading (see Figure 9e). The force transfer in the compression rods was thus limited by instability, which in turn resulted in increased deformation of the timber in the compression zone. The failure was finally caused by a tensile rupture of the rods (see Figure 9d). As for C1, the standard M20 washers were also used in the C3 configuration. Insufficient rotational restraint of the compression rod-ends led to buckling of the rods and increased utilisation of timber in compression (see Figure 9b and Figure 9c). Compression of timber is very ductile and the test was stopped after reaching large deformations without any significant decrease in capacity. The buckling of the compression rods was prevented in the C4 configuration by anchoring the compression couplers and the use of internal fitted washers. However, shorter rods were used in C4 and the ultimate failure was caused by the withdrawal of the rods in tension. Note that no initial slips were observed in any of the performed tests.

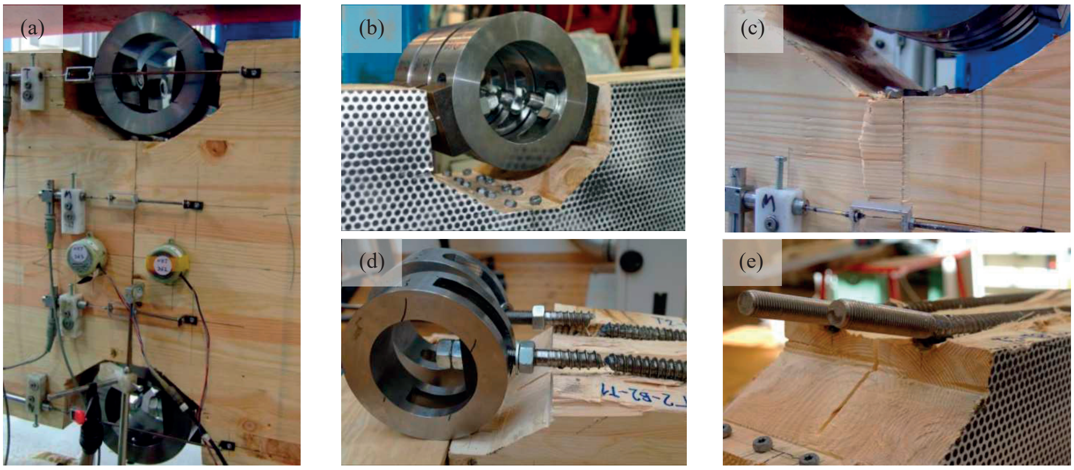

Figure 9: Joint details during and after tests: (a) C2 during test, (b) compression couplers of C3 after test, (c) failure at compression zone of C3, (d) tensile rupture of tension rods of C2, (e) compression rods of C2 after testing.

The experimental results demonstrate large rotational stiffness of the timber splice joints by the use of long threaded rods. In agreement with pure withdrawal tests of threaded rods [12], the relation between the effective length and the withdrawal stiffness is non-linear. This implies that increasing the effective length of the rods more than necessary in order to obtain the steel failure has a negligible effect on the withdrawal stiffness. Tensile ruptures of the rods were encountered for rods of 1200 mm effective length in the current investigation. In order to fully utilise the large withdrawal stiffness of the rods, slips between the rods and the couplers should be minimised. In addition, buckling of the compression rods can be avoided by anchoring the couplers to the timber.

3.2. Analytical prediction of capacity and stiffness compared to experimental and numerical results

The moment capacity M_u and the rotational stiffness k_θ of the joint obtained from experiments, numerical models and the proposed analytical model are summarised in Table 4. For the nomenclature of the input parameters, see Section 2.

Both analytical and numerical models are based on the assumption that both the position of the couplers and the slips between the rods and the couplers are restrained. Two sets of results are shown for the analytical model. The first set, denoted as Anal.A, was obtained by the use of the withdrawal stiffness of the threaded rods, K_w, obtained from the numerical models. In the second set, Anal.B, K_w was obtained by the model proposed in [12] with the assumption of the so-called pull-shear boundary conditions. The withdrawal stiffness obtained by numerical models corresponds well to the earlier investigation presented in [7] (in which the mean experimentally obtained withdrawal stiffness was 264 kN/mm), and when used in the proposed analytical model, a good agreement between the numerical and the experimental results is obtained in the prediction of the rotational stiffness. On the other hand, the use of the model in [12] gives a conservative prediction of K_w, which in turn, gives conservative estimates of the rotational stiffness of the joint.

Table 4: Experimental, numerical and analytical results

n_r	k_θ [kNm/rad]				M_u [kNm]		
	Exp.	Anal.A	Anal.B	Num.	Exp.	Anal.A	Num.
2	24952 (C2)	23227	18780	23755	169/173	188	190
3	35324 (C4)	34044	27513	36522	$241/230^*$	$284/243^*$	286

Note: Anal.A: with $K_w = 243$ kN/mm [num.] ; Anal.B: with $K_w = 176$ kN/mm by model in [12]
Input mat.: $E = 13000$ MPa, $E_s = 210$ GPa, $E_{cr} = 914$ MPa and $l_{cr} = 3$ mm [7], $k_t = 710$ MPa and $k_l =$ 1300 MPa [17, 18], $K_{co} = 450$ kN/mm [num.], $R_u = 207.6$ kN [tensile test], R_{ax} by model in [19]
Input geom.: $b = 215$ mm, $h_t = 325$ mm, $a_i = 415$ mm for lower and -90 mm for upper rods,
$d = 22.4$ mm, $d_l = 16.9$ mm, $l_f = 45$ mm, $^* l_{ef} = 1000$ mm, otherwise $l_{ef} = 1200$ mm

The experimentally obtained ultimate moments were affected by buckling of the compression rods in the configurations C1, C2 and C3 due to insufficient stiffness between the rods and the couplers, while the withdrawal of the tension rods limited the capacity in the C4 configuration. The analytical and numerical models assume no slip between the rods and the couplers, and the predicted moment capacity is, therefore, higher compared to the experimental results. A good mutual agreement is obtained for the moment capacity predicted by the analytical and the numerical models (note that the numerical models were not formulated to predict the withdrawal failure of the rods, which was the failure mode in the C4 configuration). The predicted values can thus be interpreted as a maximum moment capacity of the joint, assuring that buckling of the compression rods is prevented.

The moment-rotation curves obtained by the numerical simulations are presented together with the experimental results (for configurations containing the internal fitted washers) in Figure 10. The numerical simulations were performed both with the compression rod couplers anchored to the timber, i.e. in correspondence with the results in Table 4 (curves denoted as num.Alt.I) and without anchoring the compression couplers (curves denoted as num.Alt.II). The numerical results show that, by anchoring the compression couplers, the moment capacity is increased by 5 %, while the anchorage has a negligible effect on the rotational stiffness of the joint. When comparing the numerical and the experimental results in the case of 2 rods per row, it is observed that the moment capacity of the joint can be enhanced by 5 % if the slip between the rods and the couplers is entirely prevented and by an additional 5 % by anchoring the couplers. In the case of 3 rods per row, the couplers were anchored in the experimental setup (C4) and the failure was caused by the withdrawal of the tension rods. It is seen that by providing a sufficient effective length of the rods, an increase in moment capacity by 24 % can be achieved. With reference to Table 3, the joint efficiency, in terms of capacity, is thus improved from 40 % to 50 % in the configuration with 3 rods per row.

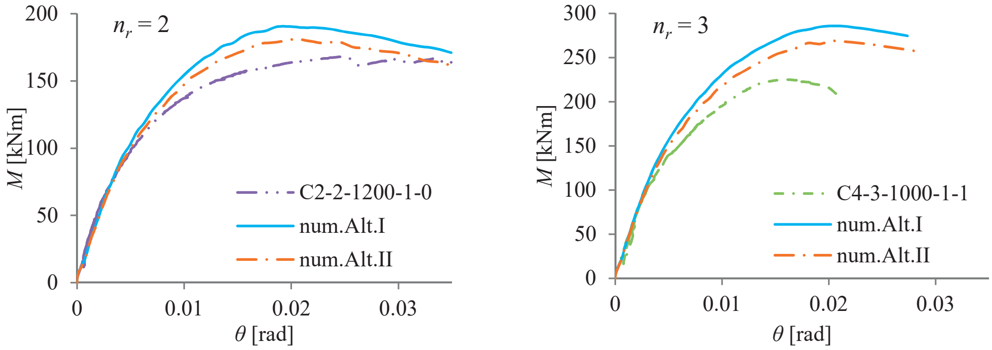

Figure 10: Moment-rotation curves obtained by the numerical models compared to the experimental results.

As discussed in Section 2.2, the rod couplers used in the current investigation were generally-suited prototypes not optimised for the particular joint layout. It is believed that the size of the couplers can be reduced, leading to smaller openings in the timber beams. If the height of the openings is reduced from the current 130 mm to 80 mm, the analytical model shows an increase of the rotational stiffness and the moment capacity by 7 % and 1%, respectively.

3.3. Combined action of bending moment and normal force

The capacity under the combined action of bending moment and normal force was studied by use of numerical models for the configuration of 2 rods per row. The results of the analyses together with the analytical solutions are shown in Figure 11 by the interaction diagrams of bending moment M and normal force N. In this study, two sets of analyses by numerical models were performed. In the first set, the rod couplers were anchored to the timber members both at the tension and the compression side (results denoted as Num.Anch.). In the second set, no interaction between the couplers and the timber was applied (results denoted as Num.Uanch.). The analytical solution was obtained by the use of Eq. (7). In the case of the "anchored" set of analyses, N_u and M_u were obtained by Eqs. (8) and (3), respectively. If the rod couplers are not anchored to the timber, the rods are susceptible to buckling and the force transfer through the rods is limited. The analytical solution shown in Figure 11 for the case of "unanchored" couplers was thus obtained for N_u determined by Eq. (8), disregarding the contribution from the rods, but assuming the full uniform distribution of compression stresses in the timber (factor 0.8 was omitted). M_u was obtained by the use of Eq. (3) with disregard of the compression rods. The input parameters to the analytical models are summarised in Table 4 (K_w from numerical models was used herein).

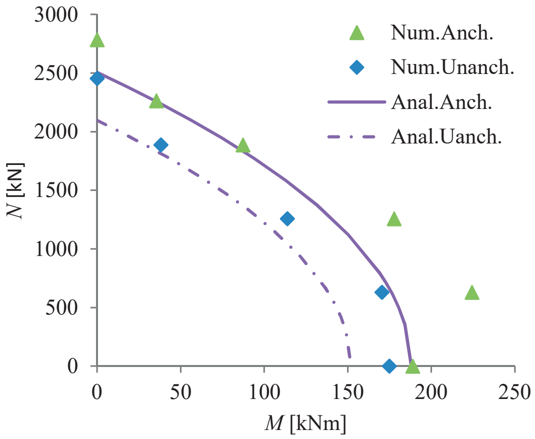

Figure 11: Interaction M-N diagram for joint with 2 rods per row.

The results in Figure 11 indicate that the proposed simple analytical interaction model enables a reasonable prediction of the joint capacity under combined action of bending moment and normal force.

4. Concluding remarks

The present investigation shows that splicing of massive glulam sections can effectively be achieved by use of inclined long threaded rods. The experimentally investigated prototype joint featured large rotational stiffness without any initial slip. It was shown that the boundary conditions at the rod-ends affect both the rotational stiffness and the moment capacity considerably. For practical design, analytical relations validated by experiments and numerical models are proposed for determination of the rotational stiffness, moment capacity and capacity under combined action of bending moment and normal force.

The rod inclination to grain prevents the loss of capacity in case of shrinkage cracks in close proximity to the threaded rods. In the current investigation, the rod-to-grain angle was 5 degrees, which is considered appropriate in order to bridge possible shrinkage cracks, as well as to maintain the large withdrawal stiffness and capacity of the rods. By providing sufficient effective length, the failure mode is ductile, due to yielding of the rods. As shown in [20], under the combined action of axial and lateral loads, both the capacity and the initial stiffness of the threaded rods are reduced for both increased rod-to-grain and load-to-rod angles.

The actual splice joint is intended for application in timber network arch bridges. In such cases, the bending moment acting in the joint will change orientations for different traffic load positions and different directions of wind loads. In addition, a considerable normal force will act in the connection, transmitted through both the contact of the timber end faces and the rods. Hence, the layout of the connection must be symmetric (i.e. the rod detailing at both sides of the connection must allow the transfer of both tension and compression) and the timber end faces must be in mutual contact provided by tightening of the rods during assembly.

Acknowledgment

This work was funded by the WoodWisdom-Net+ project DuraTB ("Durable Timber Bridges") and the support from the funding bodies and partners is gratefully acknowledged. The authors would also like to acknowledge Hallvard Oltedal Veium for his important contributions and experimental work.

Appendix

Input parameters to the expressions presented in Sections 2.1.1 and 2.1.2

The equivalent length of the compression (crushing) zone, l_c, is obtained by [7]:

$$l_c = 0.85 \cdot h_t + l_{cr} \cdot \frac{E}{E_{cr}} \tag{9}$$

where E_{cr} and l_{cr} represent experimentally obtained deformation characteristics at the end grains of two mutually compressed timber end faces.

The stiffness of the i-th rod row, K_{si}, given by Eq. (10), is obtained as a system of three springs in series representing: 1) the stiffnesses of the threaded rods in the direction of the applied force at each side of the connection denoted as K_p, and, 2) the stiffness of the rod coupler denoted as K_{co}. The number of steel rods in one row equals n_r.

$$K_{si} = n_r \cdot \frac{K_p \cdot K_{co}}{2 \cdot K_{co} + K_p} \tag{10}$$

The stiffness of the threaded rods in the direction of the applied force (parallel to the grain), K_p, is affected by the rod-to-grain and load-to-rod angles, and by the boundary conditions at the rod-end. These effects were studied and analytical relations for the stiffness prediction were derived in [20]. In the following, the relations associated with the actual geometrical layout are presented.

The rod stiffness in the direction of the applied force K_p is found as the interaction of the axial rod stiffness K_{ax} and the lateral rod stiffness K_v at the rod-end by [20]:

$$K_p = \frac{K_{ax} \cdot K_v}{K_{ax} \cdot \sin^2(\gamma) + K_v \cdot \cos^2(\gamma)} \tag{11}$$

If the displacements transverse to the load direction are prevented (by anchoring the coupler to the timber), the rod stiffness is determined by [20]:

$$K_p = K_{ax} \cdot \cos^2(\gamma) + K_v \cdot \sin^2(\gamma) \tag{12}$$

The stiffness in the axial direction K_{ax} of the rod is found by [20]:

$$K_{ax} = \frac{K_w \cdot K_{ax,f}}{K_w + K_{ax,f}} \tag{13}$$

where K_w is the withdrawal axial stiffness of the threaded rod. The axial stiffness of the free part of the rod not embedded in timber is determined as $K_{ax,f} = E_s \cdot A_s / l_f$, where l_f is the length of the free part of the rod between the timber member and the rod fastening in the coupler, E_s is the elastic modulus of steel and A_s is the cross-sectional area of the rods determined with the core diameter of the rods d_1.

Under the assumption of a rotational restraint at the rod-end implied by a connection in the couplers, the lateral stiffness at the rod-end, K_v, is found by [20]:

$$K_v = \frac{12kEI\left(4EI\lambda^3 + kl_f\right)}{48\left(EI\right)^2 \lambda^4 + 8kEI\lambda l_f\left(2l_f^2\lambda^2 + 3l_f\lambda + 3\right) + k^2 l_f^4} \tag{14}$$

where EI is the flexural stiffness of the rods obtained as $EI = E_s \cdot \pi \cdot d_1^4 / 64$, the parameter λ is found as $\lambda = \sqrt[4]{k / (4EI)}$ and k is the foundation modulus of timber obtained by the interaction of foundation moduli of timber longitudinal to the grain, k_l, and transverse to the grain, k_t, as [20]:

$$k = \frac{k_l \cdot k_t}{k_l \cdot \cos^2(\gamma) + k_t \cdot \sin^2(\gamma)} \tag{15}$$

The withdrawal strength of the rods is reduced compared to pure axial loading due to the inclination of the rods and the imposed rotational restraint at the rod-end (the rods are loaded by a combination of a lateral force and a bending moment). Similar to the model proposed in [7], the ultimate withdrawal strength of the rods R_{axu} is found by a linear reduction of the effective length of the threaded rods:

$$R_{axu} = R_{ax} \cdot \left(\frac{l_{ef} - l_x}{l_{ef}} \right) \tag{16}$$

where R_{ax} is the withdrawal strength of the threaded rods under pure axial loading (R_{ax} can be determined for the effective length of the threaded rods, l_{ef}, by the use of the model proposed in [19] with the assumption of the so-called pull-shear boundary conditions), and l_x is a free length of the rod that is not considered to contribute to the withdrawal capacity.

The free length of the rod, l_x, can be determined in the same manner as in [7] by assuming an interaction of lateral force and bending moment and respecting the actual boundary conditions at the rod-end. However, the exact analytical solution becomes unhandy to use and the following conservative simplification is thus proposed:

$$l_x = \pi \cdot d_1 \cdot \sqrt[4]{\frac{\pi \cdot E_s}{k}} \tag{17}$$

References

[1] K. Bell, Structural systems for glulam arch bridges, International Conference on Timber Bridges (ICTB 2010), Lillehammer, Norway, 2010.

[2] K.A. Malo, A. Ostrycharczyk, R. Barli, I. Hakvåg, On development of network arch bridges in timber, International Conference on Timber Bridges (ICTB 2013), Las Vegas, USA, 2013.

[3] K. Bell, L. Wollebæk, Large, mechanically joined glulam arches, Proceedings of the World Conference on Timber Engineering (WCTE 2004), Lahti, Finland, 2004.

[4] M. Cepelka, K.A. Malo, Effect of on-site splice joints for timber network arch bridges, International Conference on Timber Bridges (ICTB 2017) Skellefteå, 2017.

[5] L. Wollebæk, K. Bell, Stability of glulam arches, Proceedings of the World Conference on Timber Engineering (WCTE 2004), Lahti, Finland, 2014.

[6] J. Veie, M. Østgårdstrøen, Steibrua, Norwegian Public Roads Administration, Brukonferansen 2016 - available at https://www.vegvesen.no/_attachment/1606923/binary/1145671?fast_title=Steibrua.pdf, (last accessed 06/2017).

[7] M. Cepelka, K.A. Malo, Moment resisting splice of timber beams using long threaded rods and grout-filled couplers – Experimental results and predictive models, Submitted for publication in Construction and Building Materials (Submitted 01/2017).

[8] GOM Optical Measuring Techniques, ARAMIS, User Manual-Software, 2009.

[9] CEN, EN 26891:1991 (ISO 6891:1983) Timber structures, Joints made with mechanical fasteners, General principles for the determination of strength and deformation characteristics 1991.

[10] CEN, EN 14080:2013: Timber structures-Glued laminated timber and glued solid timber - Requirements, European Committee for Standardization, 2013.

[11] D.S.S.C. DSS, Abaqus analysis user's guide, Version 6.14, 2014.

[12] H. Stamatopoulos, K.A. Malo, Withdrawal stiffness of threaded rods embedded in timber elements, Construction and Building Materials 116 (2016) 263-272.

[13] R. Koubek, K. Dedicova, Friction of wood on steel, vol Master thesis, Linnaeus University, 2014.

[14] M. Oudjene, V.-D. Tran, E.-M. Meghlat, H. Ait-Aider, Numerical models for self-tapping screws as reinforcement of timber structures and joints, in: W.W. J. Eberhardsteiner, A. Fadai, M. Pöll (Ed.) Proceedings of the World Conference on Timber Engineering (WCTE 2016), August 22-25, 2016, Vienna University of Technology, Austria, ISBN: 978-3-903039-00-1, Vienna, Austria, 2016.

[15] K.B. Dahl, Mechanical properties of clear wood from Norway spruce. Dissertation, Department of Structural Engineering, vol Doctoral thesis, Norwegian University of Science and Technology, 2009.

[16] R. Hill, A Theory of the Yielding and Plastic Flow of Anisotropic Metals, Proceedings of the Royal Society of London 193 (1948) 281-297.

[17] N. Gattesco, Strength and local deformability of wood beneath bolted connectors, Journal of Structural Engineering 124 (1998) 195-202.

[18] N. Gattesco, I. Toffolo, Experimental study on multiple-bolt steel-to-timber tension joints, Materials and Structures/Materiaux et Constructions 37 (2004) 129-138.

[19] H. Stamatopoulos, K.A. Malo, Withdrawal capacity of threaded rods embedded in timber elements, Construction and Building Materials 94 (2015) 387-397.

[20] M. Cepelka, K.A. Malo, H. Stamatopoulos, Effect of rod-to-grain angle on capacity and stiffness of axially and laterally loaded long threaded rods in timber joints, Submitted for publication in European Journal of Wood and Wood Products (Submitted 05/2017).

Paper iv

Experimental study of end grain effects in timber joints under uniaxial compression load

Martin Cepelka, Kjell Arne Malo

In: Proceedings of the World Conference on Timber Engineering (WCTE 2016), Vienna (2016)

WCTE 2016
World Conference on
Timber Engineering
August 22-25, 2016 | Vienna, Austria

EXPERIMENTAL STUDY OF END GRAIN EFFECTS IN TIMBER JOINTS UNDER UNIAXIAL COMPRESSION LOAD

Martin Cepelka[1*], **Kjell Arne Malo**[1]

ABSTRACT: In the present study, the influence of end grain effects on strength and deformation characteristics for structural timber joints is studied. Two series of test configurations were tested. The first configuration consisted of two timber specimens with direct contact of end fibers. In the second configuration, a steel plate was placed in between the timber specimens. Both configurations were tested under uniaxial compression load parallel to the grain. The obtained results in form of capacity, initial slip, elastic surface contact stiffness and ductility factor from the respective test configurations were mutually compared. Spring stiffness model has been developed in order to quantify the surface contact stiffness. Deformation of interface area of timber-timber configuration was characterized by crushing of end fibers. The deformation pattern at the timber end faces related to crushing was described. The experiments revealed that the timber-timber configuration yielded slightly better results than the timber-steel-timber configuration regarding both strength and deformation properties.

KEYWORDS: timber joints, compression parallel to the grain, deformation properties, crushing of end fibers

1 INTRODUCTION

In various types of structural timber joints, elements are assembled lengthwise end to end. Examples of such joints are presented in Figure 1. In case of a dominating compression force, it is advantageous to transmit the compression force directly from one element to another by contact of end faces. It is then a choice of the designer whether the interconnected elements have direct timber to timber contact, or whether some supplementary agent (typically epoxy mortar Figure 1 (a) and (c), or steel plate Figure 1 (b)) is used between the two timber elements. Besides consideration of strength and deformation properties, the decision is taken based on several practical factors i.a. building and cutting tolerances, assembling techniques and not least durability issues. Epoxy mortar is often used in details in timber bridges due to ease of application. However, there have been reported cases with poor joint durability [1]. Example of epoxy mortar pushed away from joint is shown in Figure 1 (c). Deterioration of mortar allows water leakage into gaps between timber elements causing fast decay development and eventually joint damage. CNC cutting machines allow nowadays for very precise manufacturing of timber interface planes. Omitting any intermediate agent (with generally very different properties from timber), and having timber faces in direct contact is thus apparently promoted.

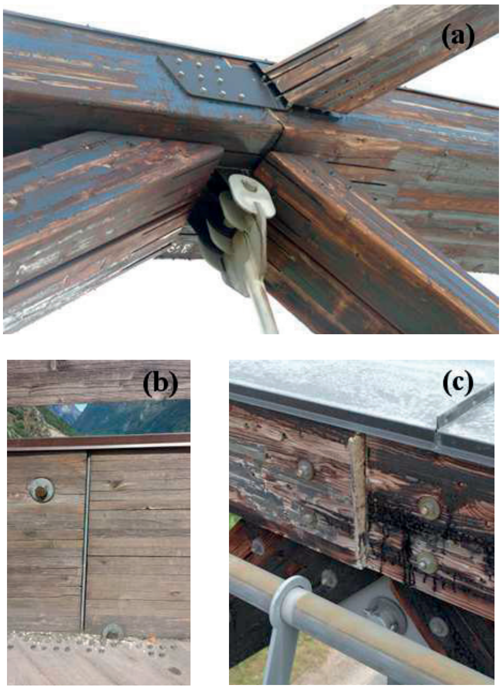

Figure 1: *(a) truss node joint at upper chord of Flisa Bridge in Norway, (b) splice connection with intermediate steel plate in Gudvangen bridge in Norway, (c) truss node joint at upper chord of Skubbersenga Bridge in Norway*

---

[1] Department of Structural Engineering, NTNU, Norwegian University of Science and Technology
[*] Corresponding author, martin.cepelka@ntnu.no

In the presented paper, the main focus is laid on investigation of strength and deformation characteristics of end joints under compression. The main motivation is to study whether avoiding an intermediate plate or mortar between timber elements results in a decrease of strength or/and stiffness. The investigation dealt with a study of end fibers crushing at timber end faces, and its influence on the joint properties. The term crushing is here used to characterize the local deformation at the two timber end surfaces (normal grain) mutually compressed.

2 TEST PROCEDURE

The tests were carried out at the laboratory of Norwegian Technical University, Department of Structural Engineering. The test procedure followed EN 408 [2], where the guidance given for determination of compression strength parallel to the grain was adopted.

2.1 DIMENSIONS, SAMPLING AND MATERIAL PROPERTIES

Dimensions of specimens were chosen to represent closely the actual problem in timber structures. The specimens had rectangular cross-section of 130x130 mm^2 and length along the grains was 300 mm. EN 408 [2] recommends the height of test pieces being six times the smaller cross-sectional dimension. This would however yield very large length without any practical benefit since the focus in the current test is on behaviour of timber interface area. The length was thus chosen to allow development of compression kinkband failure mechanism, and to accommodate measuring devices. A side benefit of rather large timber dimensions is reduced influence of local timber defects (knots) on a global behaviour.

The timber specimens were sawn from glulam beams of quality GL30c (ref. EN 14080 [3]). The glulam was fabricated of 45 mm thick lamellas of Norwegian spruce (picea abies). Each specimen thus consisted of three lamellas.

In total 48 timber specimens were prepared. Individual specimens were randomly paired for each test. The lamellas in each pair of specimens were positioned mutually parallel. Furthermore, in the test series of timber-timber contact, a parallel orientation of annual rings of laminations was assured.

2.2 MOISTURE CONTENT AND DENSITY

Both the glulam beams and the sawn specimens were conditioned at the standard environment of 20 ºC and 65 % relative humidity. Moisture content (MC) and density (ρ) of specimens were monitored at two stages. First, prior to testing, moisture content at 4 faces of each glulam specimen was measured and density at the actual moisture content was determined. Second, after each test, determination of MC and ρ by oven-drying method according to ISO 13061-1 [4] and 13061-2 [5] respectively was carried out on three timber pieces sawn from each test specimen so as each lamella was represented. Both density at moisture content ρ_W (conf. Table 2 MC corresponded to approx. 11 %) and density in the absolutely dry condition ρ_0 were determined. In total 144 timber pieces were thus examined by oven-drying method. Results of measurements are presented in Table 1 and Table 2.

Owing the conditioning of specimens, the measured MC exhibited low deviations from the standard value of 12 %. Measured density at MC (approx. 11 %) ρ_W could therefore be directly compared to requirements standardized for density at 12 % MC in EN 14080 [3]. Good agreement was found both for values of glulam and laminations. Observed normal distribution of density and amplitudes of COV agree also well with expected values provided by JCSS [6].

Table 1: *Results of density at MC (approx. 11%) ρ_W measurement on glulam specimens and sawn pieces*

	Glulam spec.[1]	Mean spec. [2]	All sawn pieces	ρ_{12} EN14081
	[kg/m^3]	[kg/m^3]	[kg/m^3]	[kg/m^3]
p_5	456	410	384	390
Mean	479	442	442	430
St.dev.	19	22	37	
COV	4.0 %	5.0 %	8.4 %	

[1] determined on glulam specimen prior to testing as a mean of measurements on 4 faces

[2] determined by oven-drying method as a mean from sawn pieces for respective lamellas in specimen

Table 2: *Results of moisture content measurement on glulam specimens and sawn pieces*

	Glulam spec.[1]	Mean spec. [2]	All sawn pieces
	[%] [1]	[%] [1]	[%] [1]
Mean	11.3	11.1	11.1
St.dev.	0.6	0.5	0.7
COV	5.6 %	4.7 %	6.2 %

[1], [2] see notes below Table 1

2.3 EXPERIMENTAL SET-UP

The experimental set-up is shown in Figure 2. Due to large cross-sectional area and high resistance of timber in compression parallel to the grain, a hydraulic actuator with force capacity of 1000 kN was used. The maximum applied force was typically in the range 500-600 kN. A deformation controlled loading with constant rate of 0,015 mm/s was used in order to reach maximum applied force within 300 s.

Two series of test configurations were tested under uniaxial compression parallel to grain. Each test series comprised of 12 individual tests. In total 24 tests were carried out. The first configuration consists of two timber specimens placed on top of each other with direct contact of end faces (denoted as "T-T" configuration). The upper specimen is denoted as "U", the lower as "L". In the second configuration, a 10 mm thick steel plate was placed in between the timber specimens (denoted as "T-S-T" configuration). Both configurations were tested using the same test procedure. The assembled pair of timber specimens was in the test set-up placed between two steel plates. A spherically seated loading-head was installed on the upper steel plate, which permitted centric application of the compressive load. Furthermore, special care was taken during the production of the specimens to ensure that upper and lower faces were sawn plane, parallel to one another and perpendicular to the axis of specimen.

Displacements were monitored by 8 LVDTs (displacement transducers). The locations of the transducers are shown in Figure 3. Two transducers were attached to each specimen (U, L) at two opposite faces denoted as 1 and 3 (transducers are consequently denoted as U1, U3 and L1, L3). Four other transducers were positioned at each face (1-4) spanning the interface between the specimens (transducers are denoted as M1-M4).

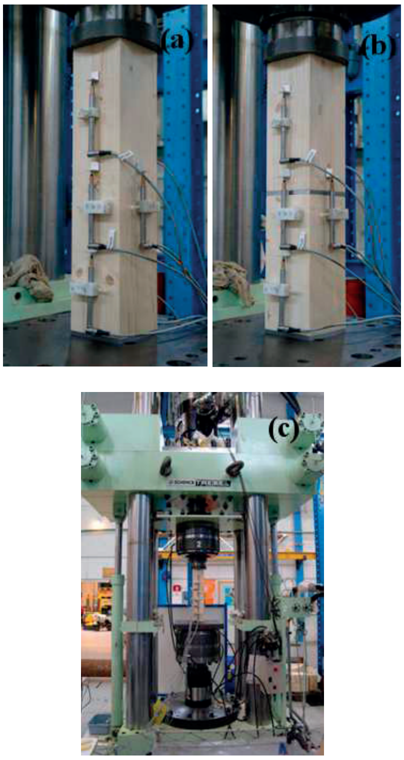

Figure 2: Test set-up: (a) detail of T-T configuration, (b) detail of T-S-T configuration, (c) overall view of loading device

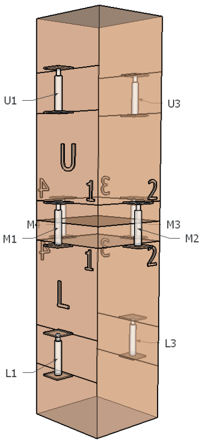

Figure 3: Location of displacement transducers

3 RESULTS AND DISCUSSION

3.1 MODES OF FRACTURE

All tests showed ductile behaviour, which is characteristic for compression parallel to the grain as recently declared among others by Dahl [7] and André et al. [8].

No distinctive difference in the modes of fracture between the two configurations could be observed. The specimens failed always by local compression failure of fibres throughout kinkband propagation. The fracture location along specimen was random and typically related to occurrence of knots. In some cases a secondary effect of splitting along the fibres occurred at high levels of loading and after the ultimate load had been reached.

For all T-T test specimens, fiber crushing at the end faces was observed. However, the magnitude of deformation varied significantly in the different tests. The development of local failure at end faces can be associated with the principle of least resistance. The compression failure occurs always at the weakest spot of the specimen. If the specimen fails at a distant location from the interface, a kinkband fracture begins to develop with low levels of deformation at the interface. The loading energy is consequently absorbed without further development of crushing at the interface zone.

As for T-S-T tests, failure occurred at various locations also for T-T configuration. Hence, the tests showed that the interface zones are not in general the weakest part. For T-T tests with intensively developed crushing, a ductile behaviour with a slow decrease of force was observed at the interface. Example of force-displacement curves of a test with characteristic ductile behaviour is presented in Figure 7. The deformation at the interface during the same test and the corresponding deformation pattern at end faces are shown in Figure 4.

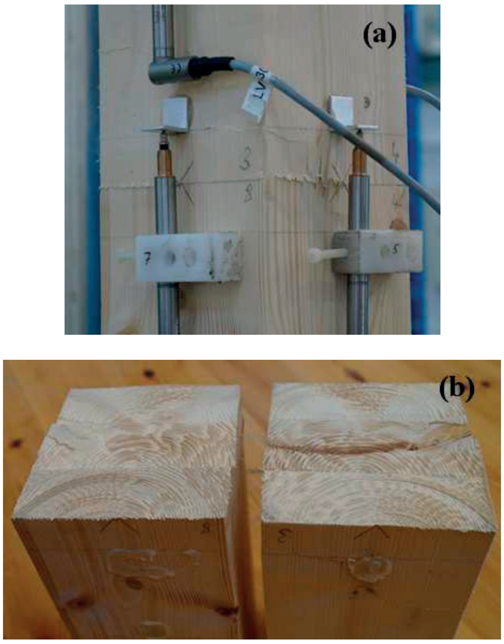

Figure 4: *Example of end fibers crushing: (a) deformation of face 3 and 4 during test, (b) deformation pattern at end faces after test (view from face 3)*

The observed crushing of end fibers was associated with a particular deformation pattern at the end faces. By closer inspection, it was evident that the deformation pattern was formed as a lattice created by mutual interference of over-passing annual rings of upper and lower specimens. Due to a generally higher density of latewood relative to earlywood, it was the latewood part of annual rings, which was being pressed into the earlywood zone of the companion specimen. Earlywood zones of both specimens were simultaneously crushed against each other so that a kind of sunken region was created. Extent of deformation was not uniform within the entire plane. In some areas, it was the fibres of upper specimen predominantly crushed into the lower specimen, whereas elsewhere the contrary applied. Based on observation of difference in deformation between latewood and earlywood, it is reasonable to suppose that development of the deformation pattern is governed by a ratio of respective local densities.

The deformation pattern is visually demonstrated in Figure 5, and bears a close resemblance to water patterns. The photo was taken on specimens from a preliminary test that had been carried out prior to the main test. Annual rings at the end faces of both specimens are heading from left to right side of the picture. Figure 5 (b) shows a schematic illustration of the deformed area. Here, clearly, both earlywood and latewood was crushed by the respective fibers of the mutual specimen.

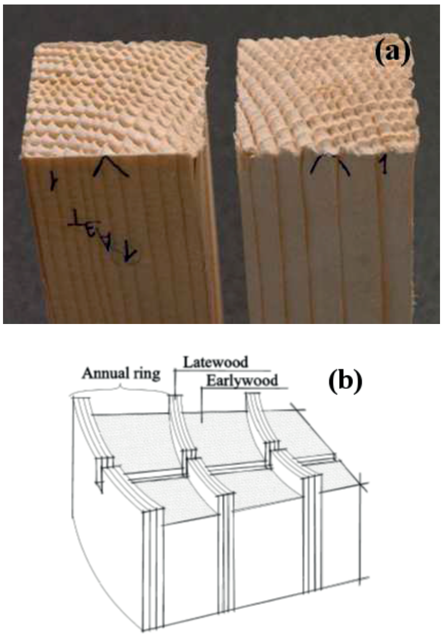

Figure 5: *Deformation pattern at timber end faces: (a) photo of pre-test specimens after test, (b) schematic illustration*

The pre-test specimens were produced from the same glulam beams. The dimension was 40/40 mm in cross section and 120 mm in length along grains. The pre-test procedure was similar to the main testing, except that only logging of the load actuator was used to monitor force-displacement characteristics. The results followed the same trend as that obtained from the main test.

3.2 STRENGTH AND DEFORMATION CHARACTERISTICS

Strength and deformation characteristics of the interface zone connecting the two specimens were of main interest.

The evaluation of capacity in compression parallel to the grain is summarized in Table 3. The capacity was simply determined as ultimate load acting at the nominal cross-sectional area of the specimens. Results for all tests sorted in increasing order are presented in Figure 6.

Table 3: *Summarized test results of capacity in compression parallel to the grain*

Conf.	Mean	p_5 (1)	St. dev.	COV
	[MPa]	[MPa]	[MPa]	[-]
T-T	33,6	30,5	1,7	0,051
T-S-T	33,3	29,0	2,3	0,069

(1) According to EN 14358:2006 [9]

It can be concluded that there is no apparent difference in capacity measured in the respective test configurations. Both the mean and the 5th percentile (p_5) were slightly higher for T-T results. Simultaneously, T-T results were in addition more clustered around the mean, leading to lower standard deviation. The results for both configurations fitted well to a lognormal distribution as proposed in [6].

The procedure in EN 14358 [9] was followed to determine the characteristic strength in compression parallel to the grain $f_{c,0,k}$. The determination was based on all tests in both T-T and T-S-T configuration. The obtained strength $f_{c,0,k}$ of 29,9 MPa was 22 % greater than the standardized value for GL30c in EN 14080 [3] of 24,5 MPa.

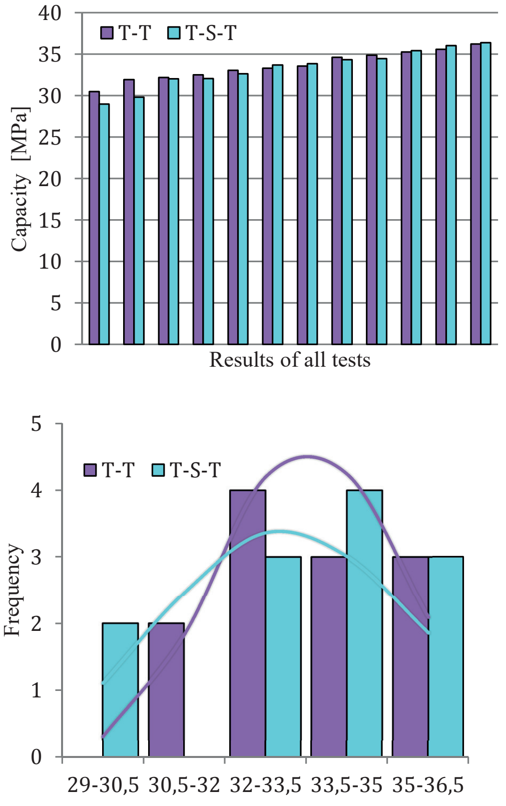

Figure 6: *Results of capacity in compression parallel to the grain for all tests*

For each test, 8 load-displacement curves were recorded corresponding to each displacement transducer in addition to the load cell. Since the monitored stiffness in compression parallel to grain is rather large, the corresponding displacements are in the range of fraction of millimetres. Hence, the accuracy of the displacements measured from the load actuator are affected by clearances in contact zones of all interacting elements and are somewhat higher than the true deformation of the specimens. The deformation parameters of the interface area were thus derived solely from measurements by LVDTs.

Force-displacement curves obtained by LVDTs could directly be used since deviations in dimensions of specimens were negligible and initial lengths, over which displacements were monitored, were kept constant. See Figure 7 and Figure 8 for representative examples of force-displacement curves of T-T and T-S-T configuration respectively. For notation of transducers see Figure 3.

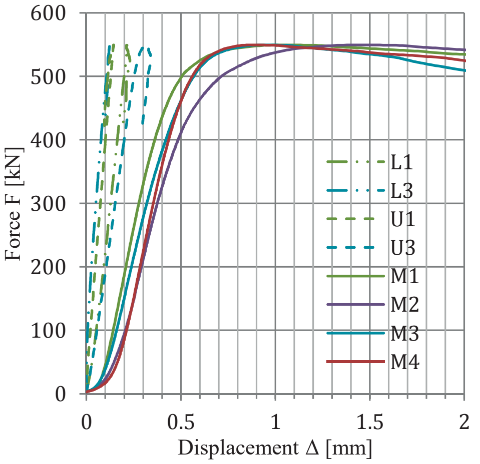

Figure 7: *Example of force-displacement curves monitored in one test of T-T configuration*

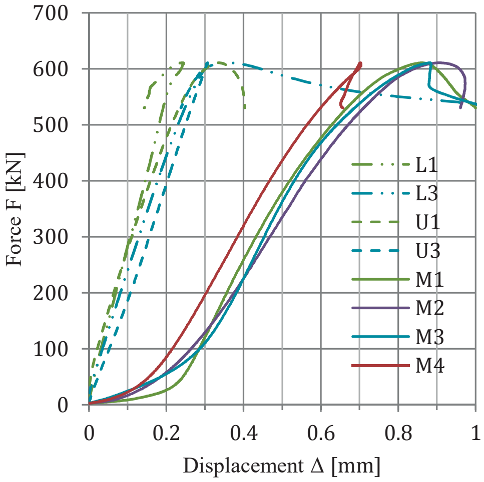

Figure 8: *Example of force-displacement curves monitored in one test of T-S-T configuration*

Considering Figure 7 and Figure 8, three clear trends can be observed. The interface values (M) are characterized by a distinct initial slip, elastic stiffness (slope of the curves) at the interface is lower than stiffness at the specimens (U, L) and the post-elastic behaviour can vary significantly for different tests. Following the mentioned trends, the evaluation of deformation characteristics at the interface was carried out in corresponding steps yielding three independent parameters: initial slip, elastic stiffness and ductility factor.

Figure 9 presents mean values of displacements measured at interface (M1-M4) for all tests. Clearly, the T-S-T configuration was characterized by a higher initial slip.

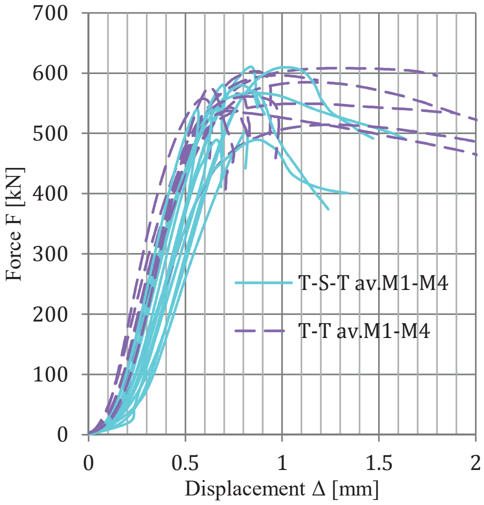

Figure 9: *Force-displacement curves for all tests as mean values of displacements at the interface (M)*

The initial slip was determined according to ISO 6891 [10] for displacements at 0,2 F_{max}. Mean of displacement measurements from all 4 faces were used (M1-M4). The evaluation of initial slip is summarized in Table 4. The T-S-T configuration showed in average 33 % higher initial slip.

Table 4: *Summarized results of evaluation of initial slip*

Conf.	Mean	St. dev.	COV
	[mm]	[mm]	[-]
T-T	0.20	0.02	0.12
T-S-T	0.26	0.05	0.19

In order to determine elastic surface contact stiffness at the interface of upper and lower specimen, a linear spring model was adopted. The simplification of the actual physical problem into spring model is presented in Figure 10.

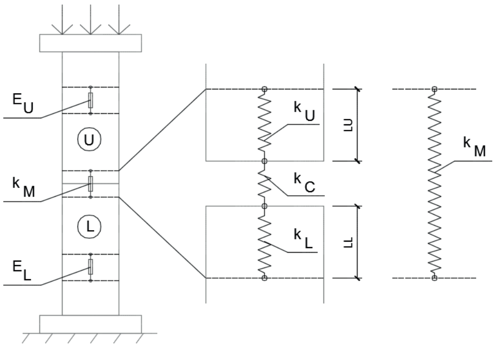

Figure 10: *Schematic visualization of problem simplification for evaluation of elastic contact stiffness at interface*

Displacements monitored by LVDTs at the interface Δ_M (considered as a mean of measurements on all 4 faces) involve 4 contributions: displacements due to deformation of the part of upper Δ_U and lower Δ_L specimen, displacements by initial slip Δ_i and displacements due to contact at end grains Δ_C. This equality is given by:

$$\Delta_M = \Delta_U + \Delta_L + \Delta_C + \Delta_i \qquad (1)$$

By assuming a material homogeneity along the entire specimen, eq. (1) takes following form:

$$\Delta_C = \Delta_M - \Delta_i - \frac{F \cdot L_U}{A_U \cdot E_U} - \frac{F \cdot L_L}{A_L \cdot E_L} \qquad (2)$$

Where F is the applied force corresponding to displacement Δ_M , A_U, A_L and E_U, E_L are cross sectional area and moduli of elasticity of the upper and the lower specimen respectively, and L_U, L_L are reference lengths (ranges) on the parts of upper and lower specimen respectively.

The moduli of elasticity for respective specimens were determined from measurements at unspliced part of upper and lower specimen (U,L) by:

$$E = \frac{k \cdot l}{A} \qquad (3)$$

where A and l are cross sectional area of specimen and length (range) on which the displacements were monitored respectively. The spring stiffness k is found as a mean of measurement at face 1 and 3 by:

$$k = \frac{F_{upper} - F_{lower}}{\Delta_{upper} - \Delta_{lower}} \qquad (4)$$

where F_{upper} - F_{lower} is the increment of load on the straight line portion within an elastic zone and Δ_{upper} - Δ_{lower} is the corresponding increment of deformation.

Upper and lower boundaries were optimized for each test in order to fit the actual range of linear elastic zone. Typically the linear range was between $F_{lower} = 0{,}3F_u$ and $F_{upper} = 0{,}6F_u$, where F_u is the ultimate loading force.

The surface contact stiffness of the interface is finally obtained by:

$$k_C = \frac{F}{\Delta_C} \tag{5}$$

Alternatively, k_C can be obtained directly by relating relative spring stiffnesses in series as:

$$k_C = \frac{k_U \cdot k_L \cdot k_M}{k_U \cdot k_L - k_U \cdot k_M - k_L \cdot k_M} \tag{6}$$

Where k_U and k_L represent spring stiffnesses of the part of the upper and lower specimen respectively and can be obtained by use of (3) and k_M represents stiffness corresponding to measured displacements Δ_M and can be obtained by use of (4).

The surface contact stiffness represents a useful parameter since it can be applied as input to numerical models. However, k_C depends in its magnitude on particular respective E-moduli of specimens. It is therefore unsuitable for relative comparison of stiffness characteristics at interface with focus on different test configurations. Hence, for relative comparison, an efficiency factor η is introduced. The efficiency factor relates the measured stiffness at interface k_M to a theoretical case of completely rigid contact (i.e. η=100 %).

The efficiency factor is defined as:

$$\eta = \frac{k_M}{\dfrac{k_U \cdot k_L}{k_U + k_L}} \tag{7}$$

Evaluation of elastic stiffness properties at interface is summarized in Table 5 and Table 6. As explained earlier, the relative comparison of results is more appropriate by the efficiency factor. The efficiency factor for all tests sorted in increasing order is presented in Figure 11.
Results for η showed insignificant difference between the respective configurations. While the mean was slightly higher for T-S-T configuration, the characteristic quantity (5th percentile) was on the contrary higher for T-T configuration. Standard deviation and COV were lower for T-T configuration. The results for both configurations fitted well to a lognormal distribution as proposed in [6] (conferring data for moduli of elasticities). Also values of k_C did not reveal any significant difference between the two configurations and again, T-T configuration yielded slightly better results.

Table 5: *Summarized results of evaluation of stiffness at interface by surface contact stiffness k_C*

Conf.	Mean	p_5 [1]	St. dev.	COV
	[kN/mm]	[kN/mm]	[kN/mm]	[-]
T-T	2796	1740	630	0,225
T-S-T	2780	1569	771	0,277

[1] According to EN 14358:2006 [9]

Table 6: *Summarized results of evaluation of stiffness at interface by efficiency factor η*

Conf.	Mean	p_5 [1]	St. dev.	COV
	[%]	[%]	[%]	[-]
T-T	53,1	39,6	7,3	0,138
T-S-T	53,4	39,0	7,7	0,145

[1] According to EN 14358:2006 [9]

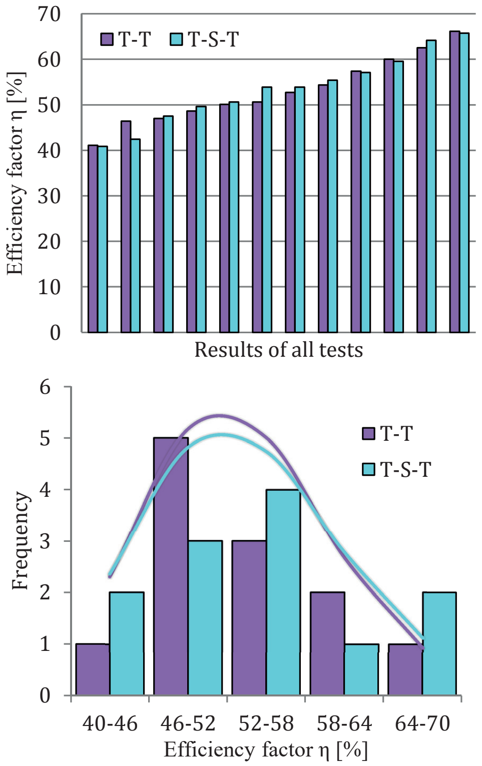

Figure 11: *Results of efficiency factor η for all tests*

While the low values of efficiency for T-T configuration can be explained by the clearly observed crushing of end fibers, interpretation of results of T-S-T configuration is more uncertain. No violation on planes of the end surfaces at contact with steel plate could be observed in any test. The possible explanation is that, in contrast to the direct contact of timber faces, the application of steel plate involves one more contact plane. Transfer of force is then carried out at two steps, each of them with a certain degree of imperfections and clearances. The preceding statement is supported by the observed higher initial slip for the T-S-T configuration (see Table 4).

The evaluation of post-elastic behaviour of the interface area is carried out on the basis of a level of ductility. It must be pointed out that the post-elastic displacements monitored by LVDTs at the interface (M) are related to the place of occurrence of fracture within the specimen. As was explained earlier, if fracture occurred outside the monitored range, the permanent displacements monitored by the LVDTs did not represent real post-elastic behaviour at the monitored location. It was however found useful to evaluate a possible trend towards particular behaviour provided by relatively high number of specimens.

The ductility evaluation was carried out according to data treatment suggested by Malo et al. [11].

The permanent displacements at the interface Δ_p are obtained by deduction of elastic part of displacements Δ_e and the initial slip Δ_i by:

$$\Delta_p = \Delta_M - \Delta_i - \Delta_e = \Delta_M - \Delta_i - \frac{F}{k_M} \tag{8}$$

Recall that F is the applied force corresponding to displacement Δ_M and k_M represents the elastic stiffness corresponding to measured displacements Δ_M.

The force-displacement curves for permanent displacements for all tests are presented in Figure 12. It is evident that for some of the T-T configuration specimens where the fracture occurred at the monitored interface area, the post-elastic behaviour was rather ductile.

The ductility factor was obtained by relating the permanent deformation at maximum load F_u to the elastic deformation at the same load:

$$D_{ue} = \frac{\Delta_{pu}}{\Delta_{eu}} = \frac{\Delta_{pu}}{\dfrac{F_u}{k_M}} \tag{9}$$

The evaluation of ductility factor is summarized in Table 7. The ductility factor for the T-T configuration was approx. 2,5 times higher compared to the T-S-T configuration.

Table 7: *Summarized results of evaluation of ductility factor*

Conf.	Mean	St. dev.	COV
	[-]	[-]	[-]
T-T	0.75	0.40	0.53
T-S-T	0.29	0.16	0.55

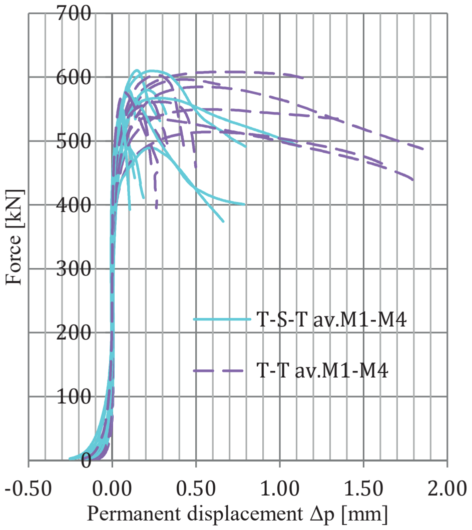

Figure 12: *Force-displacement curves for permanent displacements at the interface for all tests*

Capacity (σ_{max}) and elastic stiffness obtained from displacements of the load actuator (k_{tot}) were related to measured density (ρ) of specimens. The relations are plotted in scatter diagrams in Figure 13. The results showed a positive correlation both for T-T and T-S-T configuration. For density/capacity relation correlation coefficients were determined as $r_{\rho,\sigma max}$ = 0,69 and $r_{\rho,\sigma max}$ = 0,62 for T-T and T-S-T configuration respectively.

The elastic stiffness obtained from displacements of the load actuator represents a global response of the entire system of 2 timber specimens and the interface area. The corresponding correlation factors were found as $r_{\rho,ktot}$ = 0,70 and $r_{\rho,ktot}$ = 0,46 for T-T and T-S-T configuration respectively. The density was assumed as a minimum of upper and lower specimen for density measured prior to test on glulam specimens (see Table 1 for details). The obtained values of r were in good agreement with JCSS [6] and Dahl [7].

Due to dependence on local properties of earlywood and latewood at interface, correlation between measured density and deformation characteristics of interface area is somewhat more uncertain. Nevertheless, it is interesting to mention that there was observed a negative correlation with $\mathrm{r}_{\rho,\eta}$ = - 0,43 and $\mathrm{r}_{\rho,\mathrm{kC}}$ = - 0,29 for T-T specimens when pairing efficiency factor η and stiffness k_C with measured density. Corresponding $\mathrm{r}_{\rho,\eta/\mathrm{kC}}$ for T-S-T configuration did not show any trend.

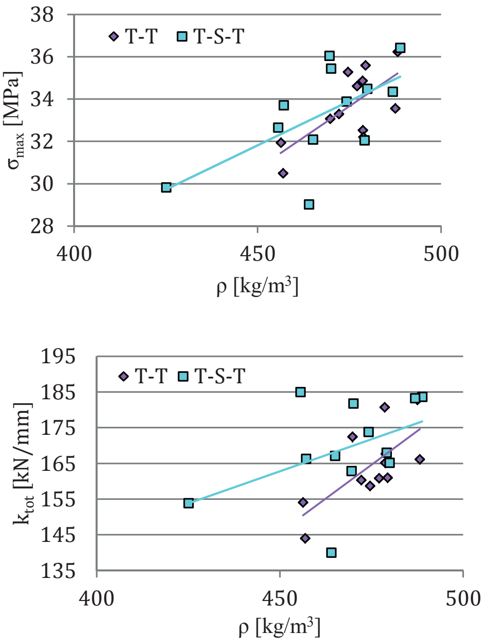

Figure 13: *Scatter diagrams for density (ρ), capacity (σ_{max}) and elastic stiffness obtained from displacements of the load actuator (k_{tot})*

4 CONCLUSIONS

End grain effects in timber joints under uniaxial compression load were studied. Two test configurations were tested. Half of the tests were set-up as a direct timber to timber contact (T-T configuration), whereas the remaining half of tests contained steel plate in between the mating wooden surfaces of the tested splice connection (T-S-T configuration).

For all T-T tests, fiber crushing at the end faces characterized by a particular deformation pattern was observed. However, based on the measured capacity and stiffness properties of the respective configurations, it is evident that neither strength nor contact stiffness at interface is enhanced by the application of a contact steel plate. Furthermore, tests with the intermediate contact steel plate were characterized by higher initial slip and less ductile post-elastic behaviour.

The following results can be highlighted:
Capacity: Very similar results were obtained for the two respective configurations.
Elastic stiffness of the interface area: Surface contact stiffness k_C and efficiency factor η have been introduced in order to describe the stiffness properties. Results showed insignificant difference between the respective configurations.
Initial slip: T-S-T configuration showed in average 33 % higher initial slip compared to T-T configuration.
Post-elastic behaviour: For T-T tests with intensively developed crushing of end fibers, a ductile behaviour with a slow decrease of force was observed at the interface.

ACKNOWLEDGEMENT

This work was funded by the WoodWisdom-Net+ project DuraTB ("Durable Timber Bridges") and the support from the funding bodies and partners is gratefully acknowledged.

REFERENCES

[1] H. Burkart, Learning Experiences from Timber Bridge Inspections, NPRA reports, Statens Vegvessen (Norwegian Public Roads Administration), 2016.
[2] CEN, EN 408:2010+A1:2012: Timber structures - Structural timber and glued laminated timber - Determination of some physical and mechanical properties, European Committee for Standardization, 2012.
[3] CEN, EN 14080:2013: Timber structures-Glued laminated timber and glued solid timber - Requirements, European Committee for Standardization, 2013.
[4] ISO, ISO 13061-1:2014(E): Physical and mechanical properties of wood - Test methods for small clear wood specimens - Part 1: Determination of moisture content for physical and mechanical tests, 2014.
[5] ISO, ISO 13061-2:2014(E): Physical and mechanical properties of wood - Test methods for small clear wood specimens - Part 1: Determination of density for physical and mechanical tests, 2014.
[6] JCSS, JCSS Probabilistic model code, Part 3: Resistance models, 3.05: Timber, Joint Committee on Structural Safety, 2006.
[7] K.B. Dahl, Mechanical properties of clear wood from Norway spruce, Department of Structural Engineering, vol Doctoral thesis, Norwegian University of Science and Technology, 2009.
[8] A. André, R. Kliger, L.E. Asp, Compression failure mechanism in small scale timber specimens, Construction and Building Materials 50 (2014) 130-139.
[9] CEN, EN 14358:2006: Timber Structures: Calculation of characteristic 5-percentile values and acceptance criteria for a sample, European Committee for Standardization, 2006.
[10] ISO, ISO 6891: Timber Structures: Joints made with mechanical fasteners: General principles for the determination of strength and deformation characteristics, 1991.
[11] K.A. Malo, J. Siem, P. Ellingsbø, Quantifying ductility in timber structures, Engineering Structures 33 (2011) 2998-3006.

Paper v

Effect of on-site splice joints for timber network arch bridges

Martin Cepelka, Kjell Arne Malo

In: Proceedings of the International Conference on Timber Bridges (ICTB 2017)
Skellefteå (2017)

Effect of on-site splice joints for timber network arch bridges

Martin CEPELKA
PhD. Candidate
Norwegian University of Science and Technology (NTNU)
Trondheim, Norway
martin.cepelka@ntnu.no

Martin Cepelka received his civil engineering degree from the Czech Technical University in Prague in 2011, worked as a bridge engineer from 2011 to 2014 and is currently pursuing a PhD at NTNU.

Kjell Arne MALO
Professor
Norwegian University of Science and Technology (NTNU)
Trondheim, Norway
kjell.malo@ntnu.no

Kjell Arne Malo is professor of timber structures at NTNU. His research topics are methods for increased strength and stiffness of connections for timber structures and vibrations in timber structures.

Summary

Feasibility studies of glulam arches with network hanger configurations have shown possibilities to achieve large spans of timber bridges. However, the length of timber elements is limited due to production and transportation issues. Long-span arches of full-timber cross sections must thus be spliced at building site. Considering stability and buckling problems of the timber arches, high requirements on flexural rigidity are imposed on the incorporated splice connections. In this paper, a novel timber splice solution using long threaded rods is presented and the effect of rotational stiffness of splice joints on stability of timber network arch bridges with spoked-wheel configuration of hangers is investigated by use of numerical models. The present investigation revealed that application of long threaded rods can provide practical splice joints with sufficient rotational stiffness in order to maintain stability of timber network arch bridges.

Keywords: timber bridge, splice joint, long threaded rod, network arch, rotational stiffness, buckling, finite element analysis

1. Introduction

The development of glued laminated timber (glulam) enables production of timber elements with nearly unlimited cross-sectional dimensions. The fact that glulam has excellent strength to weight ratio compared to steel and concrete, promotes glulam to be used in structures with large spans. However, production and transportation impose limitations on the length of timber elements. In order to obtain large spans, either truss structures or splicing of elements are necessary. Truss structures are characterised by a high number of connections, which are expensive and time consuming. When used in outdoor conditions such as timber bridges, connections have increased risk of decay due to moisture exposure.

Feasibility studies of glulam arches with network hanger configuration have shown that road timber bridges with spans reaching 100-120 m feature excellent stiffness properties and can be designed for full traffic loading [1, 2]. Massive glulam arches of such lengths must be spliced at the building site. In order to maintain stability and reduce buckling problems of the arches, it is crucial to incorporate flexural rigidity in the splice connections. The stability problems of network arch bridges containing splice joints were studied earlier in [3, 4]. These studies were carried out with a common layout of arch bridges where wind truss between arches is used to stabilize the arches laterally. A new conceptual design of timber network arch bridges presented in [2] introduces a so called spoked-wheel configuration of hangers, where hangers are inclined both in the in-plane and the out-of-plane direction. The wind truss can thus be avoided since the sideway support of the arches is provided through hangers. The out-of-plane stability of the arches can however be expected being a critical design issue and sufficient rotational stiffness of the splice joints is a key prerequisite in order to maintain the stability of the arches. In the present paper, a novel splicing solution by use of long threaded rods is presented and the effect of rotational stiffness of splice joints on stability of timber network arch bridges with spoked-wheel configuration of hangers is investigated by use of numerical models. The necessary rotational stiffness of the splice joints both in the in-plane and the out-of-plane direction is identified and the results are compared to the design possibilities of the presented splicing solution.

2. A novel splicing solution by use of long threaded rods

There are various examples of use of moment resisting splice joints in the building industry. These are mostly placed in planar structures (frames, arches) and indoor conditions. There are fewer examples of splice joints used in timber bridges. Several state-of-the-art connection techniques are presented in [5]. There are, however, no jointing techniques available, fulfilling requirements for a practical and rotationally stiff on-site splicing of large glulam sections of timber bridges.

The recent research at Norwegian University of Science and Technology, NTNU has dealt with application of long threaded rods as fasteners in timber splice connections subjected to a bending moment. The main objective of the research project has been to develop a splice that allows practical and reliable on-site splicing of large timber sections of glulam arch bridges. The dominating internal force in such structures is compression, which can be transferred by direct contact of timber end faces. Shear force can be transferred via shear keys. The design utilizes high withdrawal stiffness and has virtually no initial slip. The use of threaded rods can give rotationally stiff joints that can transfer moderate bending moments. By providing sufficient effective length, the failure mode is yielding of the steel rods. This enables a more reliable prediction of the structural properties and increased ductility of the joint.

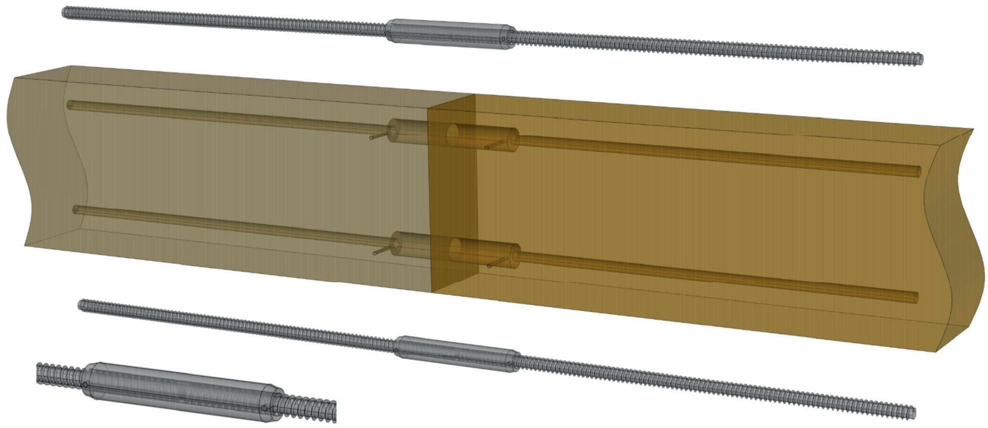

Fig. 1: Layout of splice connection with long threaded rods and grout-filled couplers.

A prototype splice joint using long threaded rods inserted parallel to the grain is shown in Fig. 1. Grout-fill steel couplers (similar to systems used for reinforced pre-cast concrete) were used for a mutual connection of the long threaded rods inserted in the opposed parts of timber beams. The steel couplers were purpose made, and manufactured from common structural steel. Two-component epoxy adhesive was used for grouting. Experimental and numerical investigations were carried out in order to determine the rotational stiffness and the moment capacity of the splice joint. Based on those, analytical relations for determining the rotational stiffness are proposed, and are here briefly summarized in the following. More details can be found in [6].
In the present analytical model, the relative rotation of the end faces of the splice connection is approximated by a relative rotation of the end sections of a beam portion of length $2l_c$. A deformed splice connection with a relative rotation θ of the end faces caused by the bending moment M is shown in Fig. 2. Here h and b are height and width of cross section respectively, a_0 is the height of wood in compression, a_i is a coordinate along z-axis of i-th row of the rods determined from the upper edge of wood in compression, l_c represents equivalent length of compression zone at each side of the connection, σ_x is normal stress in wood, K_{si} is axial stiffness of the i-th row of the rods and u_i is horizontal displacement at the the i-th row of the rods.

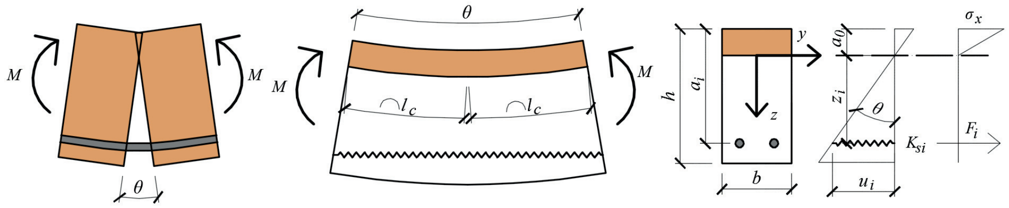

Fig. 2: Characteristics of the analytical model.

The height of wood in compression (position of neutral axis) is obtained by the following equation:

$$a_0 = \frac{-\sum_{i=1}^{n} K_{si} + \sqrt{\left(\sum_{i=1}^{n} K_{si}\right)^2 + \frac{E \cdot b}{l_c} \cdot \sum_{i=1}^{n} K_{si} \cdot a_i}}{\frac{E \cdot b}{2 \cdot l_c}} \tag{1}$$

where E is modulus of elasticity of timber parallel to the grain. The z-coordinate of the the i-th row of steel rods z_i is:

$$z_i = a_i - a_0 \tag{2}$$

The rotational stiffness of the connection k_θ is obtained as:

$$k_\theta = \frac{M}{\theta} = \sum_{i=1}^{n} K_{si} \cdot z_i^2 + \frac{E \cdot b \cdot a_0^3}{6 \cdot l_c} \tag{3}$$

The equivalent length of compression zone, l_c, is given by the following equation:

$$l_c = 0{,}85 \cdot h + l_{cr} \cdot \frac{E}{E_{cr}} \tag{4}$$

where E_{cr} is crushing modulus and l_{cr} is a crushing length.

The axial stiffness of the i-th row of steel rods, K_{si}, corresponding to the layout shown in Fig. 1 is given by Eq. (5). K_{si} is obtained as an effective stiffness of a system of three springs representing the axial withdrawal stiffnesses of the threaded rods at each side of the connection, denoted as K_w, and the axial stiffness of the joint of threaded rods in the rod coupler, denoted as K_{co}. The number of steel rods in one row is denoted as n_r.

$$K_{si} = n_r \cdot \frac{K_w \cdot K_{co}}{2 \cdot K_{co} + K_w} \tag{5}$$

With reference to the performed experimental work as presented in [6], the following input parameters were determined: K_w=264 kN/mm, K_{co}=299 kN/mm, E_{cr}=114 MPa and l_{cr}=3 mm.

The orientation of the threaded rods in the grain direction enables direct force transfer in the axial direction. It also utilizes the high withdrawal stiffness of rods parallel to the grain. On the other hand, for rods inserted parallel to the grain, the withdrawal failure is rather brittle, something that can lead to a progressive failure of a group of rods. Furthermore, the development of shrinkage cracks (in the grain direction) in close proximity to the threaded rods, can lead to loss of capacity. These shortcomings can be overcome by using long threaded rods with a small inclination to the grain.

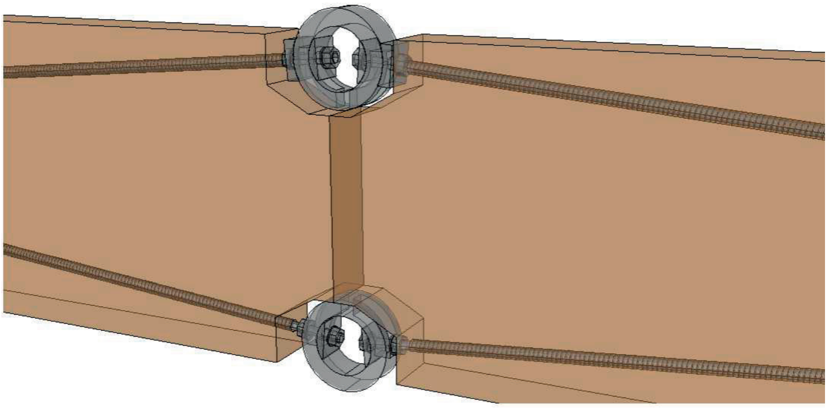

Fig. 3: Splice joint using long threaded rods inserted with an inclination to the grain.

A prototype splice joint using long threaded rods inserted with an inclination to the grain is shown in Fig. 3. Purpose made long threaded rods fabricated with a metric threaded part at the end of the rods furthermore allow easy and fast mounting of the rod coupler. The prototype joint was investigated by use of experiments and numerical models. The inclination of the rods was 5 degrees and effective length of the rods (the length of the rod screwed in the timber) was varied from 1000 mm to 1850 mm. A ductile tensile failure in rods (in the tension side) was achieved for rods of 1200 mm effective length and gross diameter of 22 mm. The experimentally tested splice joints featured large rotational stiffness and no initial slip. It should be noted that the application of the threaded rods with an inclination to the grain imposes a lateral force component at the end of the rods, which must be taken into account in the structural calculations. With reference to the analytical model presented here, Eq. (5) is adjusted for the combined axial and lateral deformations in dependence on the applied boundary conditions at the rod coupler. Detailed description of the performed work and analytical models will be published in the near future.

3. Effect of rotational stiffness of splice joints on stability of timber network arch bridges

3.1 Numerical models

A case-study arch bridge containing 2, 3 or 4 splice joints in each arch was modelled both in 2D and 3D and analysed by use of numerical models. The conceptual design of the bridge is based on the previous work of Bell [3] and Malo et al. [2]. The network configuration of hangers, where hangers cross each other at least twice, was shown to give a significantly lower bending moments and shear forces in the arches, as compared to the vertical arrangement of hangers, since the load is distributed approximately uniformly along the arch. The hangers are furthermore arranged in pairs with an out-of-plane inclination, providing a sideway support to the arches. By this so-called spoked-wheel configuration of hangers, a wind truss in between arches can be avoided, which in turn enhances durability of the arches due to lack of connections at the sides of arches. It is noted that network arch bridges present complex structural systems, for which various input parameters play important role in the distribution of stiffness characteristics and thus affect considerably the structural performance. The current investigation is limited to one particular arrangement, which is believed to be a representative example of a feasible network arch bridge with spoked-wheel configuration of hangers.

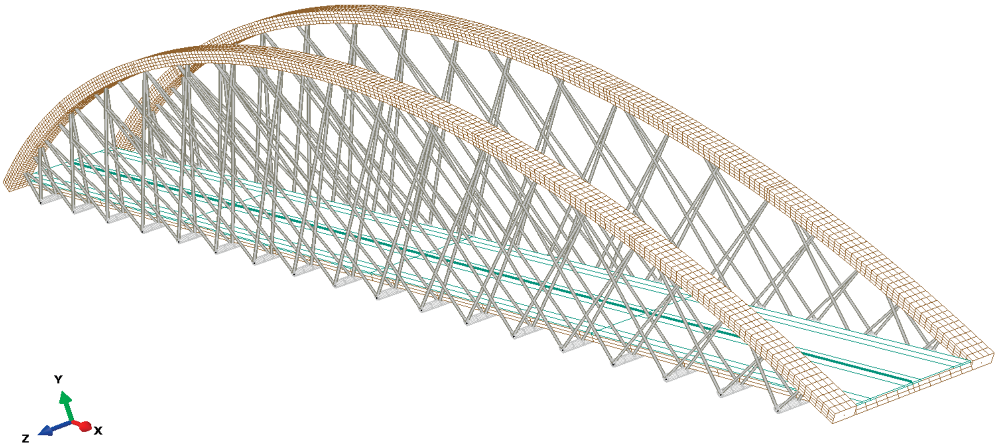

Fig. 4: 3D FEM model of the analysed bridge.

The bridge considered herein is a 2 lane road network arch bridge with a span of 100 m. The clear width of the bridge deck is 7 m, giving a distance between the centres of the arches of 8,3 m. The arch has a circular shape with the arch rise of 16 m, measured from the centre of the deck to the centre of the arch. There are 18 steel cross-beams uniformly distributed along the deck. The lateral distance between the anchor points of hangers at the cross-beams is 1200 mm (2*Z* with reference to Fig. 6). The arches have 1300 mm width and 900 mm height and are of glulam GL30c. The deck is made of a 500 m thick glulam stress-laminated slab of laminations GL24h. The steel hangers are 62 mm in diameter. The bridge parts were pre-designed according to European standards (Eurocodes) in order to assure suitable stiffness characteristics. The arches are supported through hinges in the in-plane direction, while a full rotational restraint is assumed in the out-of-plane direction at the abutments. In reality, the transverse rotational stiffness of the joint at the abutments will not be entirely rigid. However, as will be demonstrated later, the effect of a semi-rigid joint is negligible concerning stability assessments. The horizontal thrust is assumed to be taken by the abutments.

The deck displacements are restrained both in the vertical and the horizontal directions at the abutments.

The numerical analyses on a 3D model were performed by Abaqus [7], see Fig. 4. All structural parts were modelled by beam and bar elements except from the deck, which was modelled as a shell rigidly connected to the cross-beams. The hangers were defined such that they could take only tension. Dead load, traffic load (LM1) and wind load were applied according to Eurocode 1. The traffic load was applied in different configurations as shown in Fig. 5. Design values of loads were assumed in the load combinations (ULS). Static nonlinear analyses and linear (perturbation) buckling analyses were performed. The buckling analyses were in addition carried out on deformed shape of the structure (further referred to as "pre-load" since firstly the deformations by nonlinear analysis are found, and thereafter this deformed geometry is used as a base state in the buckling analysis).

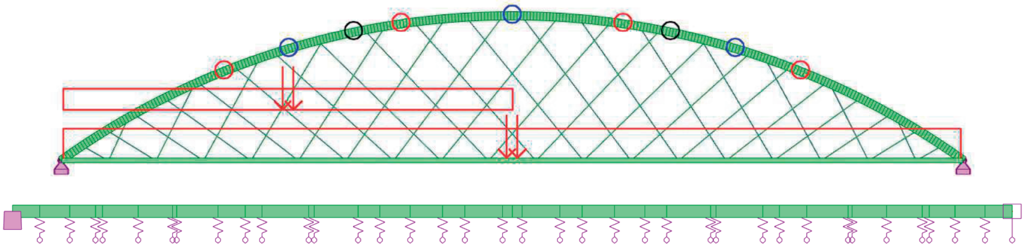

Fig. 5: 2D FEM models for analysis of in-plane (upper figure) and out-of-plane (lower figure) stability; the different configurations of the splice joints are differentiated with colours.

In order to validate the 3D model and to study the effect of the incorporated splice joints on in-plane and out-of-plane stability of the arches separately, complementary 2D analyses by use of RSAPRO [8] were performed, see Fig. 5. The in-plane model consisted of one arch carrying half the deck (modelled as a beam) by hangers which were forced to transfer only tension (with a cross section corresponding to one pair of the hangers). Nonlinear P-Δ analyses and linear buckling analyses were performed. Vertical load by dead load (including self-weight) and traffic load was assumed as shown in Fig. 5. The out-of-plane stability was studied on a simplified model consisting of the arch modelled as a straight beam (of arc length of the arch) supported by linear springs at the locations of the attachment points of the hangers. Linear buckling analyses were performed with the arch loaded by a uniform normal force along its axis. The spring stiffnesses were determined using Eq. (6), which assumes that for the lateral displacement of the arch to take place, one of the hangers in the pair buckles, while the second hanger supports the arch by its elongation component transversal to the arch.

$$K_t = \frac{E_s \cdot A_h}{L_h} \cdot \cos^2 \beta = \frac{E_s \cdot A_h}{L_h} \left(\frac{Z}{L_h} \right)^2 \tag{6}$$

Here E_s is elastic modulus of steel, A_h and L_h are cross-sectional area and length of a hanger, respectively, Z is lateral distance of a hanger anchor point at the deck level measured from the arch axis, and β is the angle between a hanger force and its component lateral to the arch. It is obvious from Eq. (6) that the lateral support of the arch, provided by hangers, decreases considerably with the increasing height of the arch above the deck. The effect is visualized in Fig. 6.

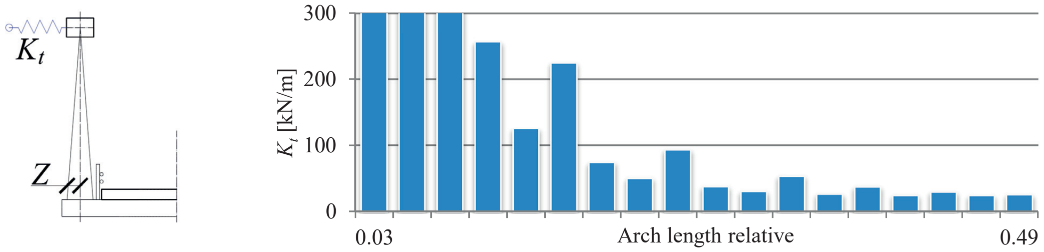

Fig. 6: Lateral elastic support of the arch provided by inclined hangers (K_t of first 3 hangers are 4480, 736 and 1166 kN/m).

3.2 Results and discussion

The results of the buckling analyses for the models without splice joints are summarized in Table 1. Here N is the maximum normal force in the arch, N_{cr} is the critical buckling normal force for which the arch becomes unstable, and $\chi = N_{cr} / N$ is a buckling load factor corresponding to the critical force (denoted as α_{cr} in Eurocode 3 [9]). The coefficient k_c is herein chosen as a measure related to stability verifications since it directly reduces the capacity of the cross section in ULS stability assessments according to Eurocode 5 [10] as shown in Eq. (7).

$$\frac{\sigma_{c,0,d}}{k_{c,y} f_{c,0,d}} + \frac{\sigma_{m,y,d}}{f_{m,y,d}} + k_m \frac{\sigma_{m,z,d}}{f_{m,z,d}} \leq 1 \quad \text{and} \quad \frac{\sigma_{c,0,d}}{k_{c,z} f_{c,0,d}} + k_m \frac{\sigma_{m,y,d}}{f_{m,y,d}} + \frac{\sigma_{m,z,d}}{f_{m,z,d}} \leq 1 \tag{7}$$

Table 1: Results of buckling analyses for models without splice joints

Model	2D		3D pre-load		3D without pre-load	
Notation	2D-in	2D-out	3D-pl V	3D-pl V+H	3D V	3D V+H
N	6831	6891	6163	6891	6163	6891
N_{cr}	91809	13162	16394	13782	16455	16745
χ	13,44	1,91	2,66	2,00	2,67	2,43
k_c	0,99	0,43	0,52	0,44	0,52	0,53

Note: V=only vertical load; V+H=vertical+horizontal load

The coefficient k_c was obtained by relations in Eurocode 5 [10] for the critical length obtained through the classical Euler's formula $N_{cr} = \pi^2 EI / L_{cr}^2$. By comparing the results from in-plane and out-of-plane 2D models with the results obtained by the 3D model, it becomes clear that buckling load of the arch is governed by the out-of-plane stability. The shape of the first buckling mode (see Fig. 8) obtained by the 3D model is also predominantly characterized by the out-ouf-plane buckling. It is therefore reasonable to calculate the coefficient k_c based on the arch stiffness EI in the out-of-plane direction. It is noted that the results presented herein correspond always to the load combination with the most unfavourable position of the traffic loading. The normal force for the out-of-plane 2D model is set equal to the maximum normal force from the 3D model for easier comparison of the relative values.

The stability of the arches containing splice joints (the locations of the splice joints are shown in Fig. 5) was studied by varying the rotational stiffness of the splice joints both in the in-plane and the out-of-plane directions. The results of the buckling analyses on models containing the splice joints are related to the unspliced models and are shown in Fig. 7. The shapes of the first buckling modes are shown in Fig. 8. The rotational stiffnesses in-plane and out-of-plane were assumed equal in the 3D models. It is, however, clear from the results that the in-plane stability is large compared to the out-of-plane stability and even for very low values of the in-plane rotational stiffness, the critical load of the arch is governed by the out-of-plane buckling.

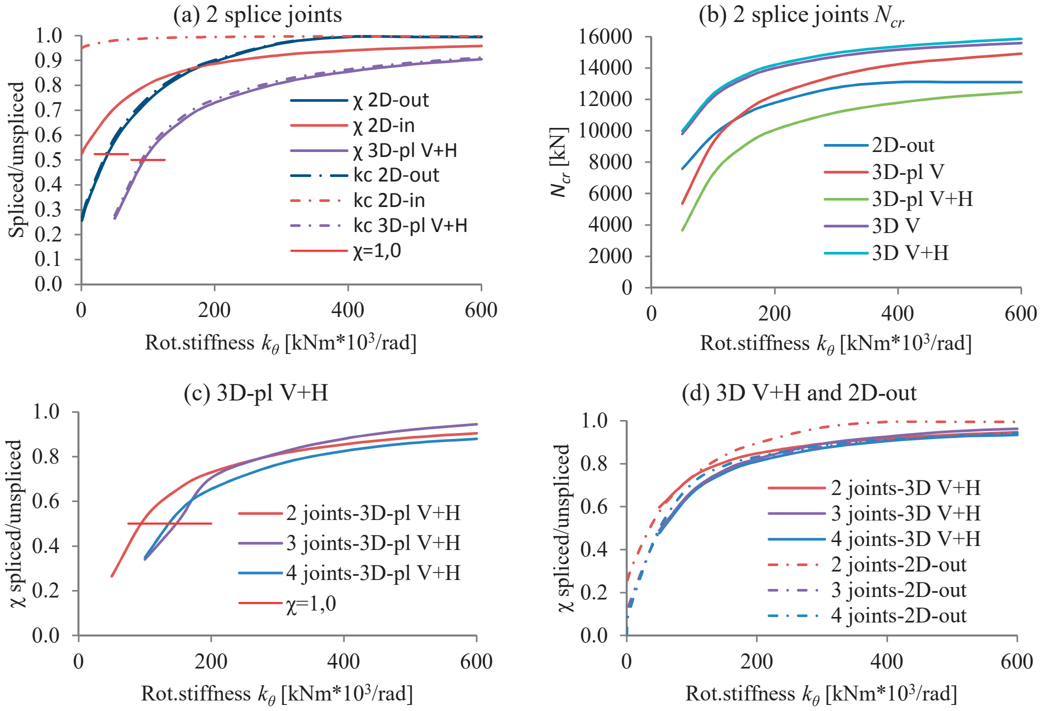

Fig. 7: Results from numerical models containing splice joints; for notation see Table 1.

Comparison of the results for the 2D in-plane, 2D out-of-plane and the 3D model is shown for the case of 2 splice joints in Fig. 7 (a). Same trends are also observed for the cases of 3 and 4 joints and the detailed results are therefore not shown herein. The comparison of cases with 2, 3 and 4 splice joints is shown in Fig. 7 (c). The results from the 3D model are shown for the case with pre-load and both vertical and horizontal loading, since this is the analysis yielding the lowest critical load, see Fig. 7 (b). The critical load obtained by the 3D model is nearly identical for the case of pure vertical loading and the case with vertical and horizontal loading in the analyses without pre-load. However, if the buckling analysis is performed on the deformed (pre-loaded) shape, the effect of the horizontal load becomes significant. From Fig. 7 (d), it is observed that the buckling behaviour of the arches with splice joints predicted by the simplified 2D out-of-plane model is similar to the results obtained by the 3D analyses without pre-load. Finally, no distinct difference is observed comparing the cases with 2, 3 and 4 splice joints. The buckling load is somewhat higher for the models with 2 joints especially for joint stiffnesses smaller than 200 000 kNm/rad. However, the buckling load factor χ is in this range close to a unity, which is the stability limit. The results indicate that for the out-of-plane rotational stiffness larger than approximately 400 000 kNm/rad, a further increase of the rotational stiffness is insignificant.

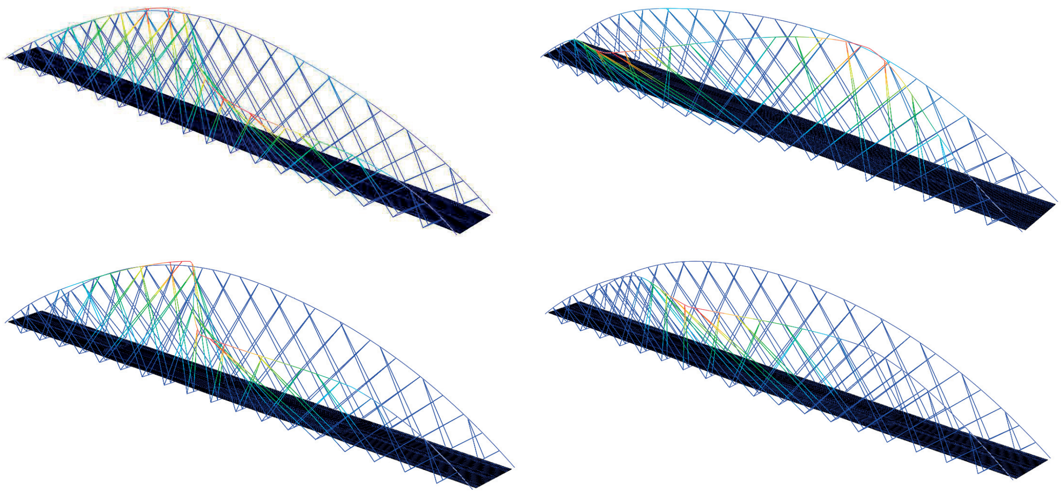

Fig. 8: Shapes of the first buckling mode: clockwise from the upper left corner: unspliced arches; 2 splices; 3 splices; 4 splices in each arch (plotted for models with k_θ=200 000 kNm/rad).

Considering the cross-sectional dimensions of the arch of 1300 mm width (out-of-plane) and 900 mm height (in-plane), the rotational stiffness of the splice joints that can be achieved by use of long threaded rods, as discussed in Section 2, will be approximately 600 000 kNm/rad in the out-of-plane direction and 500 000 kNm/rad in the in-plane direction. Based on the results presented in Fig. 7, this seems to be sufficient in order to prevent stability problems. In consideration of the most critical results, which were obtained by the 3D model with pre-load including horizontal loads (which in fact is a rather conservative approach), the effect of 2 splice joints in each arch is: $k_{c,spl.}/k_{c,unspl.}$=0,88, which means 12% reduction of the capacity. It should, however, be noted that the arch dimensions were not optimized. Consulting the extreme values of the internal forces presented in Fig. 9, a better utilization of the arches, and larger rotational stiffness of the joints, can be obtained by increasing the ratio of the width over the height of the cross section. The precedent statement is based on the assessment by Eqs. (7) which reveals that the capacity of the arch is governed by the out-of-plane buckling.

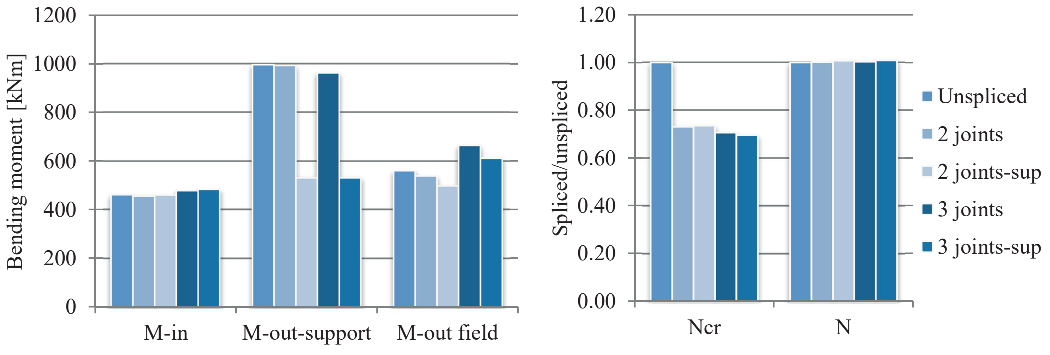

Fig. 9: Extreme values of the internal forces in the arches obtained by 3D models (3D-pl V+H; models with joints: k_θ=200 000 kNm/rad).

From the results in Fig. 9, it is evident that the splice joints have very little impact on the extreme values of the internal forces in the arches. In addition to the splice joints, a rotational stiffness of 100 000 kNm/rad was applied in the out-of-plane direction instead of the fixed rotational degree of freedom at the arch support (results denoted as "-sup"). It is seen that the effect on the critical buckling load is negligible, proving the assumption of the non-uniform distribution of the lateral arch support by hangers as shown in Fig. 6. With additional reference to Fig. 8, it is evident that the critical buckling load is reached due to instability of the central part of the arch. The semi-rigid lateral support furthermore implies that the out-of-plane bending moment at the support drops, but at the same time, the moment in the field remains approximately same, leading to a more uniform utilization of the arch.

4. Concluding remarks

It has earlier been shown that glulam arches with network hanger configuration are a feasible alternative for road bridges with spans reaching 100-120 m. An enhanced durability of the arches can moreover be achieved by avoiding the wind truss between arches and stabilizing the arch laterally through out-of-plane inclination of hangers. Since the timber arches cannot be produced and transported in one piece, rotationally stiff splice joints in arches are a key prerequisite for the viability of the design. The present investigation shows that the stability of timber network arch bridges can be maintained by use of splice joints with long threaded rods.

Acknowledgment

This work was funded by the WoodWisdom-Net+ project DuraTB ("Durable Timber Bridges") and the support from the funding bodies and partners is gratefully acknowledged. The authors would also like to acknowledge Anna Ostrycharczyk for her contribution in building up the 3D numerical model.

References

[1] Bell K., Structural Systems for Glulam Arch Bridges, *International Conference on Timber Bridges (ICTB 2010)*, Lillehammer, Norway, 2010

[2] Malo K.A., Ostrycharczyk A., Barli R., Hakvåg I., On Development of Network Arch Bridges in Timber, *International Conference on Timber Bridges (ICTB 2013)*, Las Vegas, USA, 2013

[3] Bell K., Wollebæk L., Large, Mechanically Joined Glulam Arches, *WCTE 2004*, Lahti, 2004

[4] Wollebæk L., Bell K., Stability of Glulam Arches, *WCTE 2004*, Lahti, 2014

[5] Cepelka M., Malo K.A., Review on on-site Splice Joints in Timber Engineering, *COST-Timber Bridges Conference 2014*, Biel/Bienne, 2014

[6] Cepelka M., Malo K.A., Moment Resisting Splice of Timber Beams Using Long Threaded Rods and Grout-Filled Couplers – Experimental Results and Predictive Models, *Submitted for publication in Construction and Building Materials* (Submitted 01/2017).

[7] Corp. D.S.S., Abaqus Analysis User's Guide, Version 6.14, 2014.

[8] Autodesk, Autodesk Robot Structural Analysis Proffesional (RSAPRO), 2017.

[9] CEN, Eurocode 3: Design of Steel Structures, Part 1-1: General rules and rules for buildings, European Committee for Standardization, Brussels, 2005.

[10] CEN, EN 1995-1-1:2004: Design of Timber Structures. Part 1-1: General-Common Rules and Rules for Buildings, European committee for standarization, Brussels, 2004.

Part III:
Appendices

A. Analytical description of splice efficiency

The analytical description of the splice efficiency adopted in *Paper i [95]* and *Paper iii [79]* is specified and discussed in the following.

The splice efficiency with respect to the moment capacity, η_M, is the ratio between the measured ultimate moment capacity M_u and the mean moment capacity of the un-spliced timber cross section, i.e.

$$\eta_M = \frac{M_u}{W \cdot f_{m,m}} \tag{A.1}$$

where W is the sectional modulus and $f_{m,m}$ is the mean bending strength.

The efficiency with respect to the rotational stiffness, η_k, cannot be defined directly since the relative rotation of two infinitesimally distant vertical sections in a continuous (un-spliced) beam is zero (Navier). Therefore, it was decided to describe the rotational stiffness efficiency of the joint by relating the mid-span deflection of an un-spliced beam to that of a beam containing a splice connection, see Eq. (A.2).

$$\begin{gathered} \eta_k = \frac{w_A + w_B}{w_A + w_B + w_C} \\ w_A = \frac{P \cdot l_s \cdot (3 \cdot L^2 - 4 \cdot l_s{}^2)}{48 \cdot E \cdot I}, w_B = \frac{P \cdot l_s \cdot \kappa}{2 \cdot G \cdot A}, w_C = \frac{P \cdot l_s \cdot L}{8 \cdot k_\theta} \end{gathered} \tag{A.2}$$

Here, E is the modulus of elasticity, G is the shear modulus, A is the beam cross-sectional area, I is the beam moment of inertia, κ is a shape coefficient for shear deformation and k_θ is the rotational stiffness of the splice joint. The deflection contributions w_A, w_B and w_C, corresponding to a four-point bending test arrangement (as shown in Figure A.1) are obtained from [41].

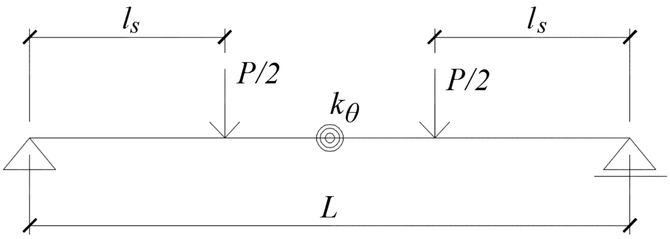

Figure A.1 Four point bending configuration of the test set-ups in [95] and [79]

It is worth noting that while the relation for the joint capacity efficiency in Eq.(A.1) is linear, the relation for the rotational stiffness in Eq.(A.2) is highly nonlinear, as illustrated in Figure A.2 for the experimental results from *Paper iii [79]*. The 100 % efficiency of the joint (i.e. fully rigid joint) can only be achieved for $k_\theta \rightarrow \infty$. This is of course practically impossible. Therefore, care must be taken when interpreting the efficiency results. Conferring Figure A.2, the nonlinearity, for example, implies that by doubling the maximum rotational stiffness obtained for the C4 configuration (from ca.35000 kNm/rad to ca. 70000 kNm/rad), the efficiency is improved only by 12 %.

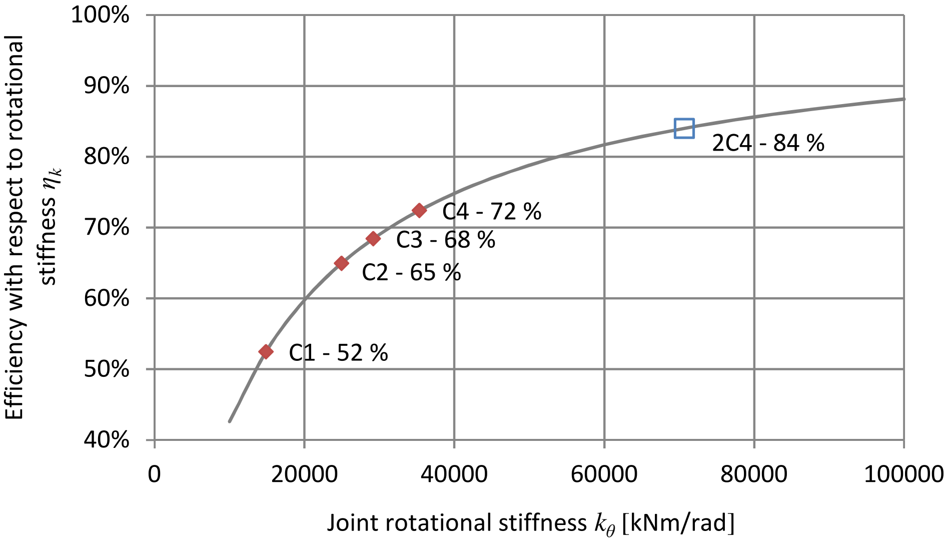

Figure A.2 Theoretical and experimental results of joint efficiency with respect to rotational stiffness corresponding to the results from Paper iii [79]

B. Derivation of the resultant stiffness of axially and laterally loaded LTRs

In the following, the derivation of the resultant stiffness of axially and laterally loaded LTRs related to the investigation in *Paper ii* [98] is presented. The respective stiffness in the axial K_{ax} and transversal direction K_v are associated with the local coordinate system of the rod $x-y$, see Figure B.1. The resultant stiffness in the load direction is found by a transformation of the local rod coordinate system into a "global" coordinate system $\bar{x}-\bar{y}$ by applying a rotation ψ. The force-displacement relation in the rod coordinate system $x-y$, $\mathbf{F}=\mathbf{K}\cdot\boldsymbol{\delta}$, transformed to the global coordinate system $\bar{x}-\bar{y}$, is denoted as $\bar{\mathbf{F}}=\bar{\mathbf{K}}\cdot\bar{\boldsymbol{\delta}}$. The transformation is carried out using the rotation tensor $\mathbf{Q}$ such that $\bar{\mathbf{K}}=\mathbf{Q}\cdot\mathbf{K}\cdot\mathbf{Q}^T$, $\bar{\mathbf{F}}=\mathbf{Q}\cdot\mathbf{F}$ and $\bar{\boldsymbol{\delta}}=\mathbf{Q}\cdot\boldsymbol{\delta}$. The rotation tensor in the matrix notation reads:

$$Q=\begin{pmatrix}\cos(\psi) & \sin(\psi)\\ -\sin(\psi) & \cos(\psi)\end{pmatrix} \tag{B.1}$$

Since the loading force F (acting along $\bar{x}$) is the resultant force, the matrix notation of the relation $\bar{\mathbf{F}}=\bar{\mathbf{K}}\cdot\bar{\boldsymbol{\delta}}$ is:

$$\begin{pmatrix}F\\ 0\end{pmatrix}=\begin{pmatrix}\bar{K}_{11} & \bar{K}_{12}\\ \bar{K}_{21} & \bar{K}_{22}\end{pmatrix}\cdot\begin{pmatrix}\delta_{\bar{x}}\\ \delta_{\bar{y}}\end{pmatrix} \tag{B.2}$$

The terms in the stiffness matrix $\bar{\mathbf{K}}$ are obtained by $\bar{\mathbf{K}}=\mathbf{Q}\cdot\mathbf{K}\cdot\mathbf{Q}^T$ as:

$$\begin{aligned}\bar{K}_{11}&=K_{ax}\cdot\cos^2(\psi)+K_v\cdot\sin^2(\psi)\\ \bar{K}_{22}&=K_{ax}\cdot\sin^2(\psi)+K_v\cdot\cos^2(\psi)\\ \bar{K}_{12}=\bar{K}_{21}&=-K_{ax}\cdot\cos(\psi)\cdot\sin(\psi)+K_v\cdot\cos(\psi)\cdot\sin(\psi)\end{aligned} \tag{B.3}$$

The set of Equations (B.2) is solved for the displacement along $\bar{x}$, $\delta_{\bar{x}}$, and the sought stiffness along $\bar{x}$ is found by $K=F/\delta_{\bar{x}}$ as:

$$K = \overline{K}_{11} - \overline{K}_{22} \cdot \left(\frac{\delta_{\overline{y}}}{\delta_{\overline{x}}} \right)^2 \tag{B.4}$$

The following equality is obtained from Eq. (B.2) :

$$\frac{\delta_{\overline{y}}}{\delta_{\overline{x}}} = -\frac{\overline{K}_{12}}{\overline{K}_{22}} \tag{B.5}$$

which inserted into Eq. (B.4), finally gives the relation for the stiffness along $\overline{x}$:

$$K = \overline{K}_{11} - \frac{\overline{K}_{12}^{\,2}}{\overline{K}_{22}} = \frac{K_{ax} \cdot K_v}{K_{ax} \cdot \sin^2(\psi) + K_v \cdot \cos^2(\psi)} \tag{B.6}$$

If displacements along $\overline{y}$ are prevented, Eq. (B.4) for $\delta_{\overline{y}} = 0$ reads:

$$K = \overline{K}_{11} = K_{ax} \cdot \cos^2(\psi) + K_v \cdot \sin^2(\psi) \tag{B.7}$$

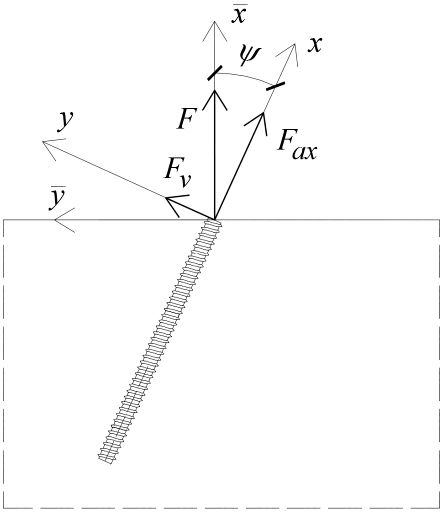

Figure B.1 LTR loaded by a force F in a direction different from the rod axis

DEPARTMENT OF STRUCTURAL ENGINEERING
NORWEGIAN UNIVERSITY OF SCIENCE AND TECHNOLOGY

N–7491 TRONDHEIM, NORWAY
Telephone: +47 73 59 47 00 Telefax: +47 73 59 47 01

"Reliability Analysis of Structural Systems using Nonlinear Finite Element Methods",
C. A. Holm, 1990:23, ISBN 82-7119-178-0.

"Uniform Stratified Flow Interaction with a Submerged Horizontal Cylinder",
Ø. Arntsen, 1990:32, ISBN 82-7119-188-8.

"Large Displacement Analysis of Flexible and Rigid Systems Considering Displacement-Dependent Loads and Nonlinear Constraints",
K. M. Mathisen, 1990:33, ISBN 82-7119-189-6.

"Solid Mechanics and Material Models including Large Deformations",
E. Levold, 1990:56, ISBN 82-7119-214-0, ISSN 0802-3271.

"Inelastic Deformation Capacity of Flexurally-Loaded Aluminium Alloy Structures",
T. Welo, 1990:62, ISBN 82-7119-220-5, ISSN 0802-3271.

"Visualization of Results from Mechanical Engineering Analysis",
K. Aamnes, 1990:63, ISBN 82-7119-221-3, ISSN 0802-3271.

"Object-Oriented Product Modeling for Structural Design",
S. I. Dale, 1991:6, ISBN 82-7119-258-2, ISSN 0802-3271.

"Parallel Techniques for Solving Finite Element Problems on Transputer Networks",
T. H. Hansen, 1991:19, ISBN 82-7119-273-6, ISSN 0802-3271.

"Statistical Description and Estimation of Ocean Drift Ice Environments",
R. Korsnes, 1991:24, ISBN 82-7119-278-7, ISSN 0802-3271.

“Properties of concrete related to fatigue damage: with emphasis on high strength concrete”,
G. Petkovic, 1991:35, ISBN 82-7119-290-6, ISSN 0802-3271.

"Turbidity Current Modelling",
B. Brørs, 1991:38, ISBN 82-7119-293-0, ISSN 0802-3271.

"Zero-Slump Concrete: Rheology, Degree of Compaction and Strength. Effects of Fillers as Part Cement-Replacement",
C. Sørensen, 1992:8, ISBN 82-7119-357-0, ISSN 0802-3271.

"Nonlinear Analysis of Reinforced Concrete Structures Exposed to Transient Loading",
K. V. Høiseth, 1992:15, ISBN 82-7119-364-3, ISSN 0802-3271.

"Finite Element Formulations and Solution Algorithms for Buckling and Collapse Analysis of Thin Shells",
R. O. Bjærum, 1992:30, ISBN 82-7119-380-5, ISSN 0802-3271.

"Response Statistics of Nonlinear Dynamic Systems",
J. M. Johnsen, 1992:42, ISBN 82-7119-393-7, ISSN 0802-3271.

"Digital Models in Engineering. A Study on why and how engineers build and operate digital models for decisison support",
J. Høyte, 1992:75, ISBN 82-7119-429-1, ISSN 0802-3271.

"Sparse Solution of Finite Element Equations",
A. C. Damhaug, 1992:76, ISBN 82-7119-430-5, ISSN 0802-3271.

"Some Aspects of Floating Ice Related to Sea Surface Operations in the Barents Sea",
S. Løset, 1992:95, ISBN 82-7119-452-6, ISSN 0802-3271.

"Modelling of Cyclic Plasticity with Application to Steel and Aluminium Structures",
O. S. Hopperstad, 1993:7, ISBN 82-7119-461-5, ISSN 0802-3271.

"The Free Formulation: Linear Theory and Extensions with Applications to Tetrahedral Elements
with Rotational Freedoms",
G. Skeie, 1993:17, ISBN 82-7119-472-0, ISSN 0802-3271.

"Høyfast betongs motstand mot piggdekkslitasje. Analyse av resultater fra prøving i Veisliter'n",
T. Tveter, 1993:62, ISBN 82-7119-522-0, ISSN 0802-3271.

"A Nonlinear Finite Element Based on Free Formulation Theory for Analysis of Sandwich Structures",
O. Aamlid, 1993:72, ISBN 82-7119-534-4, ISSN 0802-3271.

"The Effect of Curing Temperature and Silica Fume on Chloride Migration and Pore Structure of High Strength Concrete",
C. J. Hauck, 1993:90, ISBN 82-7119-553-0, ISSN 0802-3271.

"Failure of Concrete under Compressive Strain Gradients",
G. Markeset, 1993:110, ISBN 82-7119-575-1, ISSN 0802-3271.

"An experimental study of internal tidal amphidromes in Vestfjorden",
J. H. Nilsen, 1994:39, ISBN 82-7119-640-5, ISSN 0802-3271.

"Structural analysis of oil wells with emphasis on conductor design",
H. Larsen, 1994:46, ISBN 82-7119-648-0, ISSN 0802-3271.

"Adaptive methods for non-linear finite element analysis of shell structures",
K. M. Okstad, 1994:66, ISBN 82-7119-670-7, ISSN 0802-3271.

"On constitutive modelling in nonlinear analysis of concrete structures",
O. Fyrileiv, 1994:115, ISBN 82-7119-725-8, ISSN 0802-3271.

"Fluctuating wind load and response of a line-like engineering structure with emphasis on motion-induced wind forces",
J. Bogunovic Jakobsen, 1995:62, ISBN 82-7119-809-2, ISSN 0802-3271.

"An experimental study of beam-columns subjected to combined torsion, bending and axial actions",
A. Aalberg, 1995:66, ISBN 82-7119-813-0, ISSN 0802-3271.

"Scaling and cracking in unsealed freeze/thaw testing of Portland cement and silica fume concretes",
S. Jacobsen, 1995:101, ISBN 82-7119-851-3, ISSN 0802-3271.

"Damping of water waves by submerged vegetation. A case study of laminaria hyperborea",
A. M. Dubi, 1995:108, ISBN 82-7119-859-9, ISSN 0802-3271.

"The dynamics of a slope current in the Barents Sea",
Sheng Li, 1995:109, ISBN 82-7119-860-2, ISSN 0802-3271.

"Modellering av delmaterialenes betydning for betongens konsistens",
Ernst Mørtsell, 1996:12, ISBN 82-7119-894-7, ISSN 0802-3271.

"Bending of thin-walled aluminium extrusions",
Birgit Søvik Opheim, 1996:60, ISBN 82-7119-947-1, ISSN 0802-3271.

"Material modelling of aluminium for crashworthiness analysis",
Torodd Berstad, 1996:89, ISBN 82-7119-980-3, ISSN 0802-3271.

"Estimation of structural parameters from response measurements on submerged floating tunnels",
Rolf Magne Larssen, 1996:119, ISBN 82-471-0014-2, ISSN 0802-3271.

“Numerical modelling of plain and reinforced concrete by damage mechanics”,
Mario A. Polanco-Loria, 1997:20, ISBN 82-471-0049-5, ISSN 0802-3271.

“Nonlinear random vibrations - numerical analysis by path integration methods”,
Vibeke Moe, 1997:26, ISBN 82-471-0056-8, ISSN 0802-3271.

“Numerical prediction of vortex-induced vibration by the finite element method”,
Joar Martin Dalheim, 1997:63, ISBN 82-471-0096-7, ISSN 0802-3271.

“Time domain calculations of buffeting response for wind sensitive structures”,
Ketil Aas-Jakobsen, 1997:148, ISBN 82-471-0189-0, ISSN 0802-3271.

"A numerical study of flow about fixed and flexibly mounted circular cylinders",
Trond Stokka Meling, 1998:48, ISBN 82-471-0244-7, ISSN 0802-3271.

“Estimation of chloride penetration into concrete bridges in coastal areas”,
Per Egil Steen, 1998:89, ISBN 82-471-0290-0, ISSN 0802-3271.

“Stress-resultant material models for reinforced concrete plates and shells”,
Jan Arve Øverli, 1998:95, ISBN 82-471-0297-8, ISSN 0802-3271.

“Chloride binding in concrete. Effect of surrounding environment and concrete composition”,
Claus Kenneth Larsen, 1998:101, ISBN 82-471-0337-0, ISSN 0802-3271.

“Rotational capacity of aluminium alloy beams”,
Lars A. Moen, 1999:1, ISBN 82-471-0365-6, ISSN 0802-3271.

“Stretch Bending of Aluminium Extrusions”,
Arild H. Clausen, 1999:29, ISBN 82-471-0396-6, ISSN 0802-3271.

“Aluminium and Steel Beams under Concentrated Loading”,
Tore Tryland, 1999:30, ISBN 82-471-0397-4, ISSN 0802-3271.

"Engineering Models of Elastoplasticity and Fracture for Aluminium Alloys",
Odd-Geir Lademo, 1999:39, ISBN 82-471-0406-7, ISSN 0802-3271.

"Kapasitet og duktilitet av dybelforbindelser i trekonstruksjoner",
Jan Siem, 1999:46, ISBN 82-471-0414-8, ISSN 0802-3271.

“Etablering av distribuert ingeniørarbeid; Teknologiske og organisatoriske erfaringer fra en norsk ingeniørbedrift”,
Lars Line, 1999:52, ISBN 82-471-0420-2, ISSN 0802-3271.

“Estimation of Earthquake-Induced Response”,
Símon Ólafsson, 1999:73, ISBN 82-471-0443-1, ISSN 0802-3271.

“Coastal Concrete Bridges: Moisture State, Chloride Permeability and Aging Effects”
Ragnhild Holen Relling, 1999:74, ISBN 82-471-0445-8, ISSN 0802-3271.

”Capacity Assessment of Titanium Pipes Subjected to Bending and External Pressure”,
Arve Bjørset, 1999:100, ISBN 82-471-0473-3, ISSN 0802-3271.

“Validation of Numerical Collapse Behaviour of Thin-Walled Corrugated Panels”,
Håvar Ilstad, 1999:101, ISBN 82-471-0474-1, ISSN 0802-3271.

“Strength and Ductility of Welded Structures in Aluminium Alloys”,
Miroslaw Matusiak, 1999:113, ISBN 82-471-0487-3, ISSN 0802-3271.

“Thermal Dilation and Autogenous Deformation as Driving Forces to Self-Induced Stresses in High Performance Concrete”,
Øyvind Bjøntegaard, 1999:121, ISBN 82-7984-002-8, ISSN 0802-3271.

“Some Aspects of Ski Base Sliding Friction and Ski Base Structure”,
Dag Anders Moldestad, 1999:137, ISBN 82-7984-019-2, ISSN 0802-3271.

"Electrode reactions and corrosion resistance for steel in mortar and concrete",
Roy Antonsen, 2000:10, ISBN 82-7984-030-3, ISSN 0802-3271.

"Hydro-Physical Conditions in Kelp Forests and the Effect on Wave Damping and Dune Erosion. A case study on Laminaria Hyperborea",
Stig Magnar Løvås, 2000:28, ISBN 82-7984-050-8, ISSN 0802-3271.

"Random Vibration and the Path Integral Method",
Christian Skaug, 2000:39, ISBN 82-7984-061-3, ISSN 0802-3271.

"Buckling and geometrical nonlinear beam-type analyses of timber structures",
Trond Even Eggen, 2000:56, ISBN 82-7984-081-8, ISSN 0802-3271.

”Structural Crashworthiness of Aluminium Foam-Based Components”,
Arve Grønsund Hanssen, 2000:76, ISBN 82-7984-102-4, ISSN 0809-103X.

“Measurements and simulations of the consolidation in first-year sea ice ridges, and some aspects of mechanical behaviour”,
Knut V. Høyland, 2000:94, ISBN 82-7984-121-0, ISSN 0809-103X.

”Kinematics in Regular and Irregular Waves based on a Lagrangian Formulation”,
Svein Helge Gjøsund, 2000-86, ISBN 82-7984-112-1, ISSN 0809-103X.

”Self-Induced Cracking Problems in Hardening Concrete Structures”,
Daniela Bosnjak, 2000-121, ISBN 82-7984-151-2, ISSN 0809-103X.

"Ballistic Penetration and Perforation of Steel Plates",
Tore Børvik, 2000:124, ISBN 82-7984-154-7, ISSN 0809-103X.

"Freeze-Thaw resistance of Concrete. Effect of: Curing Conditions, Moisture Exchange and Materials",
Terje Finnerup Rønning, 2001:14, ISBN 82-7984-165-2, ISSN 0809-103X

"Structural behaviour of post tensioned concrete structures. Flat slab. Slabs on ground",
Steinar Trygstad, 2001:52, ISBN 82-471-5314-9, ISSN 0809-103X.

"Slipforming of Vertical Concrete Structures. Friction between concrete and slipform panel",
Kjell Tore Fosså, 2001:61, ISBN 82-471-5325-4, ISSN 0809-103X.

"Some numerical methods for the simulation of laminar and turbulent incompressible flows",
Jens Holmen, 2002:6, ISBN 82-471-5396-3, ISSN 0809-103X.

“Improved Fatigue Performance of Threaded Drillstring Connections by Cold Rolling”,
Steinar Kristoffersen, 2002:11, ISBN: 82-421-5402-1, ISSN 0809-103X.

"Deformations in Concrete Cantilever Bridges: Observations and Theoretical Modelling",
Peter F. Takâcs, 2002:23, ISBN 82-471-5415-3, ISSN 0809-103X.

"Stiffened aluminium plates subjected to impact loading",
Hilde Giæver Hildrum, 2002:69, ISBN 82-471-5467-6, ISSN 0809-103X.

"Full- and model scale study of wind effects on a medium-rise building in a built up area",
Jónas Thór Snæbjørnsson, 2002:95, ISBN82-471-5495-1, ISSN 0809-103X.

“Evaluation of Concepts for Loading of Hydrocarbons in Ice-infested water”,
Arnor Jensen, 2002:114, ISBN 82-417-5506-0, ISSN 0809-103X.

”Numerical and Physical Modelling of Oil Spreading in Broken Ice”,
Janne K. Økland Gjøsteen, 2002:130, ISBN 82-471-5523-0, ISSN 0809-103X.

”Diagnosis and protection of corroding steel in concrete”,
Franz Pruckner, 20002:140, ISBN 82-471-5555-4, ISSN 0809-103X.

“Tensile and Compressive Creep of Young Concrete: Testing and Modelling”,
Dawood Atrushi, 2003:17, ISBN 82-471-5565-6, ISSN 0809-103X.

“Rheology of Particle Suspensions. Fresh Concrete, Mortar and Cement Paste with Various Types of Lignosulfonates”,
Jon Elvar Wallevik, 2003:18, ISBN 82-471-5566-4, ISSN 0809-103X.

“Oblique Loading of Aluminium Crash Components”,
Aase Reyes, 2003:15, ISBN 82-471-5562-1, ISSN 0809-103X.

“Utilization of Ethiopian Natural Pozzolans”,
Surafel Ketema Desta, 2003:26, ISSN 82-471-5574-5, ISSN:0809-103X.

“Behaviour and strength prediction of reinforced concrete structures with discontinuity regions”, Helge Brå, 2004:11, ISBN 82-471-6222-9, ISSN 1503-8181.

“High-strength steel plates subjected to projectile impact. An experimental and numerical study”, Sumita Dey, 2004:38, ISBN 82-471-6282-2 (printed version), ISBN 82-471-6281-4 (electronic version), ISSN 1503-8181.

“Alkali-reactive and inert fillers in concrete. Rheology of fresh mixtures and expansive reactions.”
Bård M. Pedersen, 2004:92, ISBN 82-471-6401-9 (printed version), ISBN 82-471-6400-0 (electronic version), ISSN 1503-8181.

“On the Shear Capacity of Steel Girders with Large Web Openings”.
Nils Christian Hagen, 2005:9 ISBN 82-471-6878-2 (printed version), ISBN 82-471-6877-4 (electronic version), ISSN 1503-8181.

”Behaviour of aluminium extrusions subjected to axial loading”.
Østen Jensen, 2005:7, ISBN 82-471-6873-1 (printed version), ISBN 82-471-6872-3 (electronic version), ISSN 1503-8181.

”Thermal Aspects of corrosion of Steel in Concrete”.
Jan-Magnus Østvik, 2005:5, ISBN 82-471-6869-3 (printed version), ISBN 82-471-6868 (electronic version), ISSN 1503-8181.

”Mechanical and adaptive behaviour of bone in relation to hip replacement.” A study of bone remodelling and bone grafting.
Sébastien Muller, 2005:34, ISBN 82-471-6933-9 (printed version), ISBN 82-471-6932-0 (electronic version), ISSN 1503-8181.

“Analysis of geometrical nonlinearities with applications to timber structures”.
Lars Wollebæk, 2005:74, ISBN 82-471-7050-5 (printed version), ISBN 82-471-7019-1 (electronic version), ISSN 1503-8181.

“Pedestrian induced lateral vibrations of slender footbridges”,
Anders Rönnquist, 2005:102, ISBN 82-471-7082-5 (printed version), ISBN 82-471-7081-7 (electronic version), ISSN 1503-8181.

“Initial Strength Development of Fly Ash and Limestone Blended Cements at Various Temperatures Predicted by Ultrasonic Pulse Velocity”,
Tom Ivar Fredvik, 2005:112, ISBN 82-471-7105-8 (printed version), ISBN 82-471-7103-1 (electronic version), ISSN 1503-8181.

“Behaviour and modelling of thin-walled cast components”,
Cato Dørum, 2005:128, ISBN 82-471-7140-6 (printed version), ISBN 82-471-7139-2 (electronic version), ISSN 1503-8181.

“Behaviour and modelling of selfpiercing riveted connections”,
Raffaele Porcaro, 2005:165, ISBN 82-471-7219-4 (printed version), ISBN 82-471-7218-6 (electronic version), ISSN 1503-8181.

”Behaviour and Modelling og Aluminium Plates subjected to Compressive Load”,
Lars Rønning, 2005:154, ISBN 82-471-7169-1 (printed version), ISBN 82-471-7195-3 (electronic version), ISSN 1503-8181.

”Bumper beam-longitudinal system subjected to offset impact loading”,
Satyanarayana Kokkula, 2005:193, ISBN 82-471-7280-1 (printed version), ISBN 82-471-7279-8 (electronic version), ISSN 1503-8181.

“Control of Chloride Penetration into Concrete Structures at Early Age”,
Guofei Liu, 2006:46, ISBN 82-471-7838-9 (printed version), ISBN 82-471-7837-0 (electronic version), ISSN 1503-8181.

“Modelling of Welded Thin-Walled Aluminium Structures”,
Ting Wang, 2006:78, ISBN 82-471-7907-5 (printed version), ISBN 82-471-7906-7 (electronic version), ISSN 1503-8181.

”Time-variant reliability of dynamic systems by importance sampling and probabilistic analysis of ice loads”,
Anna Ivanova Olsen, 2006:139, ISBN 82-471-8041-3 (printed version), ISBN 82-471-8040-5 (electronic version), ISSN 1503-8181.

“Fatigue life prediction of an aluminium alloy automotive component using finite element analysis of surface topography”.
Sigmund Kyrre Ås, 2006:25, ISBN 82-471-7791-9 (printed version), ISBN 82-471-7791-9 (electronic version), ISSN 1503-8181.

”Constitutive models of elastoplasticity and fracture for aluminium alloys under strain path change”,
Dasharatha Achani, 2006:76, ISBN 82-471-7903-2 (printed version), ISBN 82-471-7902-4 (electronic version), ISSN 1503-8181.

“Simulations of 2D dynamic brittle fracture by the Element-free Galerkin method and linear fracture mechanics”,
Tommy Karlsson, 2006:125, ISBN 82-471-8011-1 (printed version), ISBN 82-471-8010-3 (electronic version), ISSN 1503-8181.

“Penetration and Perforation of Granite Targets by Hard Projectiles”,
Chong Chiang Seah, 2006:188, ISBN 82-471-8150-9 (printed version), ISBN 82-471-8149-5 (electronic version), ISSN 1503-8181.

“Deformations, strain capacity and cracking of concrete in plastic and early hardening phases”, Tor Arne Hammer, 2007:234, ISBN 978-82-471-5191-4 (printed version), ISBN 978-82-471-5207-2 (electronic version), ISSN 1503-8181.

“Crashworthiness of dual-phase high-strength steel: Material and Component behaviour”, Venkatapathi Tarigopula, 2007:230, ISBN 82-471-5076-4 (printed version), ISBN 82-471-5093-1 (electronic version), ISSN 1503-8181.

“Fibre reinforcement in load carrying concrete structures”, Åse Lyslo Døssland, 2008:50, ISBN 978-82-471-6910-0 (printed version), ISBN 978-82-471-6924-7 (electronic version), ISSN 1503-8181.

“Low-velocity penetration of aluminium plates”, Frode Grytten, 2008:46, ISBN 978-82-471-6826-4 (printed version), ISBN 978-82-471-6843-1 (electronic version), ISSN 1503-8181.

“Robustness studies of structures subjected to large deformations”, Ørjan Fyllingen, 2008:24, ISBN 978-82-471-6339-9 (printed version), ISBN 978-82-471-6342-9 (electronic version), ISSN 1503-8181.

“Constitutive modelling of morsellised bone”, Knut Birger Lunde, 2008:92, ISBN 978-82-471-7829-4 (printed version), ISBN 978-82-471-7832-4 (electronic version), ISSN 1503-8181.

“Experimental Investigations of Wind Loading on a Suspension Bridge Girder”, Bjørn Isaksen, 2008:131, ISBN 978-82-471-8656-5 (printed version), ISBN 978-82-471-8673-2 (electronic version), ISSN 1503-8181.

“Cracking Risk of Concrete Structures in The Hardening Phase”, Guomin Ji, 2008:198, ISBN 978-82-471-1079-9 (printed version), ISBN 978-82-471-1080-5 (electronic version), ISSN 1503-8181.

“Modelling and numerical analysis of the porcine and human mitral apparatus”, Victorien Emile Prot, 2008:249, ISBN 978-82-471-1192-5 (printed version), ISBN 978-82-471-1193-2 (electronic version), ISSN 1503-8181.

“Strength analysis of net structures”, Heidi Moe, 2009:48, ISBN 978-82-471-1468-1 (printed version), ISBN 978-82-471-1469-8 (electronic version), ISSN1503-8181.

“Numerical analysis of ductile fracture in surface cracked shells”, Espen Berg, 2009:80, ISBN 978-82-471-1537-4 (printed version), ISBN 978-82-471-1538-1 (electronic version), ISSN 1503-8181.

"Subject specific finite element analysis of bone – for evaluation of the healing of a leg lengthening and evaluation of femoral stem design",
Sune Hansborg Pettersen, 2009:99, ISBN 978-82-471-1579-4 (printed version), ISBN 978-82-471-1580-0 (electronic version), ISSN 1503-8181.

"Evaluation of fracture parameters for notched multi-layered structures",
Lingyun Shang, 2009:137, ISBN 978-82-471-1662-3 (printed version), ISBN 978-82-471-1663-0 (electronic version), ISSN 1503-8181.

"Modelling of Dynamic Material Behaviour and Fracture of Aluminium Alloys for Structural Applications"
Yan Chen, 2009:69, ISBN 978-82-471-1515-2 (printed version), ISBN 978-82 471-1516-9 (electronic version), ISSN 1503-8181.

"Nanomechanics of polymer and composite particles"
Jianying He 2009:213, ISBN 978-82-471-1828-3 (printed version), ISBN 978-82-471-1829-0 (electronic version), ISSN 1503-8181.

"Mechanical properties of clear wood from Norway spruce"
Kristian Berbom Dahl 2009:250, ISBN 978-82-471-1911-2 (printed version) ISBN 978-82-471-1912-9 (electronic version), ISSN 1503-8181.

"Modeling of the degradation of TiB_2 mechanical properties by residual stresses and liquid Al penetration along grain boundaries"
Micol Pezzotta 2009:254, ISBN 978-82-471-1923-5 (printed version) ISBN 978-82-471-1924-2 (electronic version) ISSN 1503-8181.

"Effect of welding residual stress on fracture"
Xiabo Ren 2010:77, ISBN 978-82-471-2115-3 (printed version) ISBN 978-82-471-2116-0 (electronic version), ISSN 1503-8181.

"Pan-based carbon fiber as anode material in cathodic protection system for concrete structures"
Mahdi Chini 2010:122, ISBN 978-82-471-2210-5 (printed version) ISBN 978-82-471-2213-6 (electronic version), ISSN 1503-8181.

"Structural Behaviour of deteriorated and retrofitted concrete structures"
Irina Vasililjeva Sæther 2010:171, ISBN 978-82-471-2315-7 (printed version) ISBN 978-82-471-2316-4 (electronic version) ISSN 1503-8181.

"Prediction of local snow loads on roofs"
Vivian Meløysund 2010:247, ISBN 978-82-471-2490-1 (printed version) ISBN 978-82-471-2491-8 (electronic version) ISSN 1503-8181.

"Behaviour and modelling of polymers for crash applications"
Virgile Delhaye 2010:251, ISBN 978-82-471-2501-4 (printed version) ISBN 978-82-471-2502-1 (electronic version) ISSN 1503-8181.

“Blended cement with reducted CO_2 emission – Utilizing the Fly Ash-Limestone Synergy”,
Klaartje De Weerdt 2011:32, ISBN 978-82-471-2584-7 (printed version) ISBN 978-82-471-2584-4 (electronic version) ISSN 1503-8181.

“Chloride induced reinforcement corrosion in concrete” Concept of critical chloride content – methods and mechanisms.
Ueli Angst 2011:113, ISBN 978-82-471-2769-9 (printed version) ISBN 978-82-471-2763-6 (electronic version) ISSN 1503-8181.

“A thermo-electric-Mechanical study of the carbon anode and contact interface for Energy savings in the production of aluminium”.
Dag Herman Andersen 2011:157, ISBN 978-82-471-2859-6 (printed version) ISBN 978-82-471-2860-2 (electronic version) ISSN 1503-8181.

“Structural Capacity of Anchorage Ties in Masonry Veneer Walls Subjected to Earthquake”. The implications of Eurocode 8 and Eurocode 6 on a typical Norwegain veneer wall.
Ahmed Mohamed Yousry Hamed 2011:181, ISBN 978-82-471-2911-1 (printed version) ISBN 978-82-471-2912-8 (electronic ver.) ISSN 1503-8181.

“Work-hardening behaviour in age-hardenable Al-Zn-Mg(-Cu) alloys”.
Ida Westermann , 2011:247, ISBN 978-82-471-3056-8 (printed ver.) ISBN 978-82-471-3057-5 (electronic ver.) ISSN 1503-8181.

“Behaviour and modelling of selfpiercing riveted connections using aluminium rivets”.
Nguyen-Hieu Hoang, 2011:266, ISBN 978-82-471-3097-1 (printed ver.) ISBN 978-82-471-3099-5 (electronic ver.) ISSN 1503-8181.

“Fibre reinforced concrete”.
Sindre Sandbakk, 2011:297, ISBN 978-82-471-3167-1 (printed ver.) ISBN 978-82-471-3168-8 (electronic ver) ISSN 1503:8181.

“Dynamic behaviour of cablesupported bridges subjected to strong natural wind”.
Ole Andre Øiseth, 2011:315, ISBN 978-82-471-3209-8 (printed ver.) ISBN 978-82-471-3210-4 (electronic ver.) ISSN 1503-8181.

“Constitutive modeling of solargrade silicon materials”
Julien Cochard, 2011:307, ISBN 978-82-471-3189-3 (printed ver). ISBN 978-82-471-3190-9 (electronic ver.) ISSN 1503-8181.

“Constitutive behavior and fracture of shape memory alloys”
Jim Stian Olsen, 2012:57, ISBN 978-82-471-3382-8 (printed ver.) ISBN 978-82-471-3383-5 (electronic ver.) ISSN 1503-8181.

"Field measurements in mechanical testing using close-range photogrammetry and digital image analysis"
Egil Fagerholt, 2012:95, ISBN 978-82-471-3466-5 (printed ver.) ISBN 978-82-471-3467-2 (electronic ver.) ISSN 1503-8181.

"Towards a better under standing of the ultimate behaviour of lightweight aggregate concrete in compression and bending",
Håvard Nedrelid, 2012:123, ISBN 978-82-471-3527-3 (printed ver.) ISBN 978-82-471-3528-0 (electronic ver.) ISSN 1503-8181.

"Numerical simulations of blood flow in the left side of the heart"
Sigrid Kaarstad Dahl, 2012:135, ISBN 978-82-471-3553-2 (printed ver.) ISBN 978-82-471-3555-6 (electronic ver.) ISSN 1503-8181.

"Moisture induced stresses in glulam"
Vanessa Angst-Nicollier, 2012:139, ISBN 978-82-471-3562-4 (printed ver.) ISBN 978-82-471-3563-1 (electronic ver.) ISSN 1503-8181.

"Biomechanical aspects of distraction osteogensis"
Valentina La Russa, 2012:250, ISBN 978-82-471-3807-6 (printed ver.) ISBN 978-82-471-3808-3 (electronic ver.) ISSN 1503-8181.

"Ductile fracture in dual-phase steel. Theoretical, experimental and numerical study"
Gaute Gruben, 2012:257, ISBN 978-82-471-3822-9 (printed ver.) ISBN 978-82-471-3823-6 (electronic ver.) ISSN 1503-8181.

"Damping in Timber Structures"
Nathalie Labonnote, 2012:263, ISBN 978-82-471-3836-6 (printed ver.) ISBN 978-82-471-3837-3 (electronic ver.) ISSN 1503-8181.

"Biomechanical modeling of fetal veins: The umbilical vein and ductus venosus bifurcation"
Paul Roger Leinan, 2012:299, ISBN 978-82-471-3915-8 (printed ver.) ISBN 978-82-471-3916-5 (electronic ver.) ISSN 1503-8181.

"Large-Deformation behaviour of thermoplastics at various stress states"
Anne Serine Ognedal, 2012:298, ISBN 978-82-471-3913-4 (printed ver.) ISBN 978-82-471-3914-1 (electronic ver.) ISSN 1503-8181.

"Hardening accelerator for fly ash blended cement"
Kien Dinh Hoang, 2012:366, ISBN 978-82-471-4063-5 (printed ver.) ISBN 978-82-471-4064-2 (electronic ver.) ISSN 1503-8181.

"From molecular structure to mechanical properties"
Jianyang Wu, 2013:186, ISBN 978-82-471-4485-5 (printed ver.) ISBN 978-82-471-4486-2 (electronic ver.) ISSN 1503-8181.

“Experimental and numerical study of hybrid concrete structures”
Linn Grepstad Nes, 2013:259, ISBN 978-82-471-4644-6 (printed ver.) ISBN 978-82-471-4645-3 (electronic ver.) ISSN 1503-8181.

“Mechanics of ultra-thin multi crystalline silicon wafers”
Saber Saffar, 2013:199, ISBN 978-82-471-4511-1 (printed ver.) ISBN 978-82-471-4513-5 (electronic ver). ISSN 1503-8181.

“Through process modelling of welded aluminium structures”
Anizahyati Alisibramulisi, 2013:325, ISBN 978-82-471-4788-7 (printed ver.) ISBN 978-82-471-4789-4 (electronic ver.) ISSN 1503-8181.

“Combined blast and fragment loading on steel plates”
Knut Gaarder Rakvåg, 2013:361, ISBN978-82-471-4872-3 (printed ver.) ISBN 978-82-4873-0 (electronic ver.). ISSN 1503-8181.

“Characterization and modelling of the anisotropic behaviour of high-strength aluminium alloy”
Marion Fourmeau, 2014:37, ISBN 978-82-326-0008-3 (printed ver.) ISBN 978-82-326-0009-0 (electronic ver.) ISSN 1503-8181.

“Behaviour of threated steel fasteners at elevated deformation rates”
Henning Fransplass, 2014:65, ISBN 978-82-326-0054-0 (printed ver.) ISBN 978-82-326-0055-7 (electronic ver.) ISSN 1503-8181.

“Sedimentation and Bleeding”
Ya Peng, 2014:89, ISBN 978-82-326-0102-8 (printed ver.) ISBN 978-82-326-0103-5 (electric ver.) ISSN 1503-8181.

“Impact against X65 offshore pipelines”
Martin Kristoffersen, 2014:362, ISBN 978-82-326-0636-8 (printed ver.) ISBN 978-82-326-0637-5 (electronic ver.) ISSN 1503-8181.

“Formability of aluminium alloy subjected to prestrain by rolling”
Dmitry Vysochinskiy, 2014:363,, ISBN 978-82-326-0638-2 (printed ver.) ISBN 978-82-326-0639-9 (electronic ver.) ISSN 1503-8181.

“Experimental and numerical study of Yielding, Work-Hardening and anisotropy in textured AA6xxx alloys using crystal plasticity models”
Mikhail Khadyko, 2015:28, ISBN 978-82-326-0724-2 (printed ver.) ISBN 978-82-326-0725-9 (electronic ver.) ISSN 1503-8181.

“Behaviour and Modelling of AA6xxx Aluminium Alloys Under a Wide Range of Temperatures and Strain Rates”
Vincent Vilamosa, 2015:63, ISBN 978-82-326-0786-0 (printed ver.) ISBN 978-82-326-0787-7 (electronic ver.) ISSN 1503-8181.

"A Probabilistic Approach in Failure Modelling of Aluminium High Pressure Die-Castings"
Octavian Knoll, 2015:137, ISBN 978-82-326-0930-7 (printed ver.) ISBN 978-82-326-0931-4 (electronic ver.) ISSN 1503-8181.

"Ice Abrasion on Marine Concrete Structures"
Egil Møen, 2015:189, ISBN 978-82-326-1034-1 (printed ver.) ISBN 978-82-326-1035-8 (electronic ver.) ISSN 1503-8181.

"Fibre Orientation in Steel-Fibre-Reinforced Concrete"
Giedrius Zirgulis, 2015:229, ISBN 978-82-326-1114-0 (printed ver.) ISBN 978-82-326-1115-7 (electronic ver.) ISSN 1503-8181.

"Effect of spatial variation and possible interference of localised corrosion on the residual capacity of a reinforced concrete beam"
Mohammad Mahdi Kioumarsi, 2015:282, ISBN 978-82-326-1220-8 (printed ver.) ISBN 978-82-1221-5 (electronic ver.) ISSN 1503-8181.

"The role of concrete resistivity in chloride-induced macro-cell corrosion"
Karla Horbostel, 2015:324, ISBN 978-82-326-1304-5 (printed ver.) ISBN 978-82-326-1305-2 (electonic ver.) ISSN 1503-8181.

"Flowable fibre-reinforced concrete for structural applications"
Elena Vidal Sarmiento, 2015-335, ISBN 978-82-326-1324-3 (printed ver.) ISBN 978-82-326-1325-0 (electronic ver.) ISSN 1503-8181.

"Development of chushed sand for concrete production with microproportioning"
Rolands Cepuritis, 2016:19, ISBN 978-82-326-1382-3 (printed ver.) ISBN 978-82-326-1383-0 (electronic ver.) ISSN 1503-8181.

"Withdrawal properties of threaded rods embedded in glued-laminated timer elements"
Haris Stamatopoulos, 2016:48, ISBN 978-82-326-1436-3 (printed ver.) ISBN 978-82-326-1437-0 (electronic ver.) ISSN 1503-8181.

"An Experimental and numerical study of thermoplastics at large deformation"
Marius Andersen, 2016:191, ISBN 978-82-326-1720-3 (printed ver.) ISBN 978-82-326-1721-0 (electronic ver.) ISSN 1503-8181.

"Modeling and Simulation of Ballistic Impact"
Jens Kristian Holmen, 2016:240, ISBN 978-82-326-1818-7 (printed ver). ISBN 978-82-326-1819-4 (electronic ver.) ISSN 1503-8181.

"Early age crack assessment of concrete structures"
Anja B. Estensen Klausen, 2016:256, ISBN 978-82-326-1850-7 (printed ver). ISBN 978-82-326-1851-4 (electronic ver.) ISSN 1503-8181.

“Uncertainty quantification and sensitivity analysis for cardiovascular models”
Vinzenz Gregor Eck, 2016:234, ISBN 978-82-326-1806-4 (printed ver.) ISBN 978-82-326-1807-1 (electronic ver.) ISSN 1503-8181.

“Dynamic behaviour of existing and new railway catenary systems under Norwegain conditions”
Petter Røe Nåvik, 2016:298, ISBN 978-82-326-1935-1 (printed ver.) ISBN 978-82-326-1934-4 (electronic ver.) ISSN 1503-8181.

“Mechanical behaviour of particle-filled elastomers at various temperatures”
Arne Ilseng, 2016-295, ISBN978-82-326-1928-3 (printed ver.) ISBN 978-82-326-1929-0 (electronic ver.) ISSN 1503-8181.

“Nanotechnology for Anti-Icing Application”
Zhiwei He, 2016:348, ISBN 978-82-326-2038-8 (printed ver.) ISBN 978-82-326-2019-5 (electronic ver.) ISSN 1503-8181.

“Conduction Mechanisms in Conductive Adhesives with Metal-Coated Polyer Spheres”
Sigurd Rolland Pettersen, 2016:349, ISBN 978-326-2040-1 (printed ver,) ISBN 978-82-326-2041-8 (electronic ver.) ISSN 1503-8181.

“The interaction between calcium lignosulfonate and cement”
Alessia Colombo, 2017:20, ISBN 978-82-326-2122-4 (printed ver.) ISBN 978-82-326-2123-1 (electronic ver.) ISSN 1503-8181.

“Behaviour and Modelling of Flexible Structures Subjected to Blast Loading”
Vegard Aune, 2017:101, ISBN 978-82-326-2274-0 (printed ver.) ISBN 978-82-326-2275-7 (electronic ver.) ISSN 1503-8181.

“Behaviour of steel connections under quasi-static and impact loading”
Erik Løhre Grimsmo, 2017:159, ISBN 978-82-326-2390-7 (printed ver.) ISBN 978-82-326-2391-4 (electronic ver.) ISSN 1503-8181.

“An experimental and numerical study of cortical bone at he macro and Nano-scale”
Masoud Ramenzanzadehkoldeh,, 2017:208, ISBN 978-82-326-2488-1 (printed ver.) ISBN 978-82-326-2489-8 (electronic ver.) ISSN 1503-8181.

“Optoelectrical Properties of a Novel Organic Semiconductor: 6,13-Dichloropentacene”
Mao Wang, 2017:130, ISBN 978-82-326-2332-7 (printed ver.) ISBN 978-82-326-2333-4) (electronic ver.) ISSN 1503-8181.

“Core-shell structured microgels and their behavior at oil and water interface”
Yi Gong, 2017:182, ISBN 978-82-326-2436-2 (printed. ver.) ISBN 978-82-326-2437-9 (electronic ver.) ISSN 1503-8181.

“Aspects of design of reinforced concrete structures using nonliear finite element analyses”
Morten Engen, 2017:149, ISBN 978-82-326-2370-9 (printed ver.) ISBN 978-82-326-2371-6 (electronic ver.) ISSN 1503-8181.

“Numerical studies on ductile failure of aluminium alloys”
Lars Edvard Dæhli, 2017:284, ISBN 978-82-326-2636-6 (printed ver.) ISBN 978-82-326-2637-3 (electronic ver.) ISSN 1503-8181.

“Modelling and Assessment of Hydrogen Embrittlement in Steels and Nickel Alloys”
Haiyang Yu, 2017:278, ISBN 978-82-326-2624-3 (printed. ver.) ISBN 978-82-326-2625-0 (electronic ver.) ISSN 1503-8181.